Department of Mechanical Engineering

Thermal Enhancement Strategies for Fluid Jets Impinging on a Heated Surface

Andrew James Campbell King

This thesis is presented for the degree of
Doctor of Philosophy
of
Curtin University of Technology

December 2007

Declaration

To the best of my knowledge and belief this thesis contains no material previously published by any other person except where due acknowledgement has been made.

This thesis contains no material which has been accepted for the award of any other degree or diploma in any university.

All investigations presented in this thesis are my own except where specific reference has been made to the work of others. A list of papers in which some of this work has been published is provided in Appendix A.

Signature: _____

Date: _____

Abstract

This research investigation examines the thermal behaviour of single and arrays of fluid jets impinging at heated surfaces, and formulates enhancement schemes for the jet impingement heat transfer processes for high-intensity cooling applications. The proposed techniques are numerically modelled and analysed over a wide parametric range to identify flow characteristics leading to thermal enhancement and optimum performance.

The first scheme applies to a single fluid jet and incorporates a protruding object at the impingement surface to improve heat transfer. In this, a conical protrusion of high thermal conductivity is attached to the heated surface directly beneath the jet. Three different aspect ratios of 0.5, 1 and 2 are investigated for the protrusion while the inclusion of a fillet at the base of the cone is also studied. Jet Reynolds numbers between 100 and 30,000 are modelled. The observed thermal performance is compared with a reference case having no surface attachment. With this arrangement, the heat transfer rate typically varies between 10 and 40 percent above the reference case although depending on certain parametric combinations, the heat transfer may increase above or decrease below the reference performance. The highest indicated increase in heat transfer is about 90 percent while 15 percent below is the lowest. Careful selection of cone surface profile creates potential for further thermal enhancement.

The second scheme applies to a single fluid jet and incorporates a recess in the impingement surface to improve heat transfer. In this, a cylindrical cavity is introduced to the surface beneath the jet into which the fluid jet impinges. The effects of the cavity on heat transfer are examined for a number of different cavity diameters, cavity depths and jet discharge heights wherein a surface without a cavity is taken as the reference surface. Cavity diameters of 2, 3 and 4 times the jet diameter are investigated at cavity depths between zero and 4 times the jet diameter. Jet discharge heights range between 2 jet diameters above the reference surface to 2 jet diameters below the reference surface. The jet Reynolds number is varied between 100 and 30,000. With

this enhancement technique, increases in heat transfer rates of up to 45 percent are observed when compared to the reference performance.

The thermal performance of fluid jet arrays is examined by altering square or hexagonal array configurations to identify flow characteristics leading to optimal heat transfer rates. For this, the jet to jet spacing is varied between 1.5 and 7 times the jet diameter while the jet to surface height is varied between 2 and 6 times the jet diameter. Jet Reynolds numbers between 100 and 30,000 are investigated. For each configuration, a critical jet-to-jet spacing is identified below which the heat transfer is observed to reduce significantly. Correlations for the expected heat transfer for a square or hexagonal array are presented in terms of the jet to jet spacing, jet height and jet Reynolds number.

Acknowledgments

I would like to acknowledge the following people, without whom this task would have been all the much more difficult.

Firstly, my supervisor, Associate Professor Tilak Chandratilleke, who provided support, guidance and valuable insight throughout the period of my studies at Curtin, both undergraduate and postgraduate.

Dr Mark Pitman, who helped me maintain my sanity throughout my time as a post graduate student.

Finally, my family, who have always been supportive of my endeavours, and who instilled me with the curiosity to start down this path in the first place.

Table of Contents

List of Figures

Nomenclature

d	Diameter of the jet nozzle	m
d_c	Cone diameter	m
	Cavity diameter	m
k	Turbulent kinetic energy	m^2/s^2
k_f	Thermal Conductivity of the fluid	$W/m\,K$
l	Distance between jet centerlines	m
	Cavity depth	m
L	Net cup depth	m
$\dot{q}$	Heat transfer rate from the surface	W
ΔT	Difference between jet exit temperature (ambient) and surface temperature	m/s
V	Bulk velocity of the jet	m/s
z	Distance between the reference surface and the jet nozzle exit	m
α	Cone aspect ratio	–
μ	Dynamic viscosity of fluid	$kg/m\,s$
ρ	Fluid density	kg/m^3

Non-dimensional Groups

Re	Reynolds Number	$\rho V d/\mu$
Nu	Nusselt Number	$h_c d/k_f$

Chapter 1

Introduction

This thesis presents three schemes aimed at improving the heat transfer performance of impinging jet systems. Impinging jets offer amongst the highest heat transfer rates possible from single phase convection and for this reason have been applied to solve heat transfer problems in a diverse range of industries, from micro-electronics to steel production to power generation. With such broad application, identifying and evaluating avenues for further heat transfer enhancement is of enormous benefit and has been the focus of much research. The work presented in this thesis provides a significant contribution to this area in identifying and evaluating three distinct schemes capable of achieving heat transfer rates greater than those obtainable using conventional impinging jets.

Before these schemes are presented it is first necessary to describe an impinging jet. An impinging jet is formed when a free flow, such as one discharging from a pipe or orifice, is interrupted by the presence of a plate or surface. The fluid now impinges on the surface and undergoes a sharp change in direction. When the fluid and surface temperature differ, heat transfer occurs between the jet and the surface. A example of an impinging jet is shown in Figure 1.1.

An impinging jet exhibits three distinct flow regions: the development region,

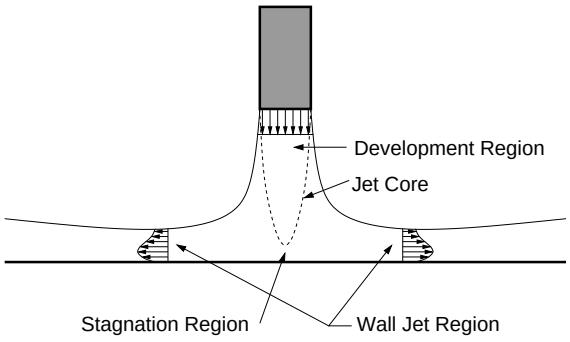

Figure 1.1: An impinging jet, identifying three distinct flow regions

where the fluid exits the nozzle and flows towards the surface; the stagnation region, where the jet strikes the surface; and the wall jet region, where the fluid flows parallel to the surface [1].

In the development region, fluid from the surroundings is entrained into the jet and the velocity is reduced. Within this zone, however, a region where the fluid velocity is close to that of the bulk jet velocity can still be identified. This region is known as the jet core. Identifying this region is useful as the highest values for heat transfer are generally observed when the surface is located to coincide with the end of the jet core, at a distance of about five to six times the jet diameter from the jet nozzle exit.

In the stagnation region, the axial momentum of the jet decreases as the fluid nears the surface and is deflected to flow along it. This give a corresponding rise in the static pressure in this region, and a stagnation point is formed where the jet centreline intersects the surface. The stagnation region provides the highest local heat transfer rates in an impinging jet.

In the wall jet region, high levels of turbulence are generated in the flow due to shear forces acting between the surface and the adjacent fluid. This promotes heat transfer and a localised increase is observed in this region. Where the jet-to-surface distance is small, typically less than five times the jet diameter, a secondary local maximum is observed in the local heat transfer rate, at a distance of approximately two times the jet diameter from the jet centreline.

The presence of these three distinct regions in an impinging jet results in a heat transfer distribution over the target surface that is highly localised. The useful region for heat transfer is typically located within five diameters from the jet centreline as indicated in the heat transfer distribution plots in Figure 1.2.

1.1 Enhancement Techniques

The highly localised nature of impinging jet heat transfer presents two readily apparent paths to enhance heat transfer from the impingement surface. The first is to focus on

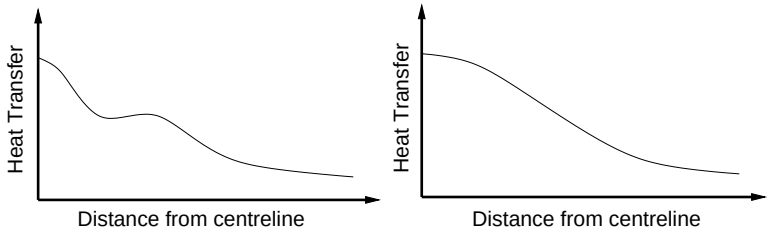

(a) $z/D < 5$ (b) $z/D > 5$

Figure 1.2: Typical Heat Transfer Distributions for a single impinging jet

increasing the maximum local heat transfer rate from a single impinging jet, while the second is to focus on reducing the spatial variation in the heat transfer distribution. These are introduced further in the following two sections.

1.1.1 Local Heat Transfer

Two separate schemes directed at improving the local heat transfer from an impinging jet are identified and investigated in this thesis. Both seek to improve the heat transfer by modifying the surface geometry and, as a result, the surrounding flow.

The first scheme aims to increase the heat transfer from a circular impinging jet by modifying the flow in the stagnation region. This is achieved by attaching a solid, highly conductive cone-shaped protrusion to the surface directly beneath the jet, centred on the jet axis. The second scheme modifies the flow in the wall jet region by introducing an additional change in direction to the fluid. This is achieved by the addition of a cylindrical cavity again located directly beneath the jet and centred on the jet axis. The two schemes are presented in Figures 1.3(a) and 1.3(b).

No previous investigations or reports on either of these enhancement techniques are found in the literature, and the investigation and evaluation of these schemes provides a significant contribution to the field.

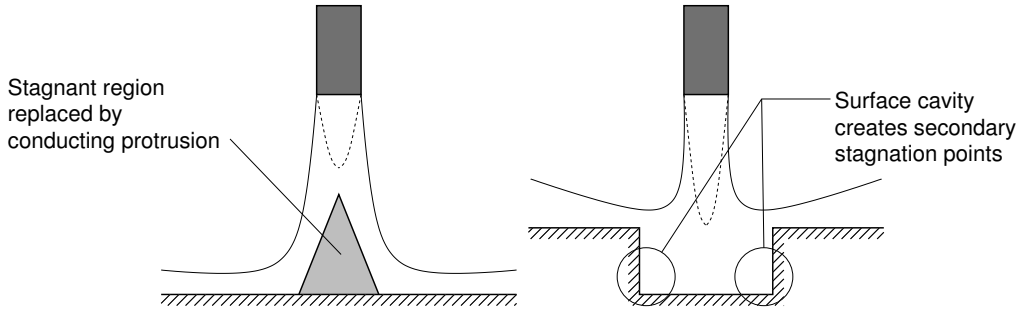

(a) Surface Protrusion proposal (b) Surface Cavity proposal

Figure 1.3: Proposed schemes for enhancing heat transfer rates from a single impinging jet.

1.1.2 Uniform Heat Transfer

The two schemes mentioned in the previous section are concerned with isolated impinging jets. In many cases, however, the area over which heat transfer is to take place is large, and the spatial variation of heat transfer observed in a single jet is not ideal. In these situations, arrays of impinging jets are typically employed. The applications where this type of heat transfer is desirable are numerous, and as such arrays of impinging jets have been subject to much previous investigation. Even so, only a few detailed parametric studies on the heat transfer from impinging jet arrays have been published. This work addresses this shortfall by investigating and correlating the available heat transfer from a large number of impinging jet arrays.

In this work consideration is given to large arrays, where the diameters of the individual jets are considerably smaller than the total size of the array. This means a significant number of jets are required to provide the necessary heat transfer, and it is advantageous to know the most effective geometry. For these arrays the number of jets on the edge of the array is small in comparison to the number of internal jets, and a 'representative jet' analysis technique can be used to determine the heat transfer from the array. A 'representative jet' analysis considers only a single jet in the array. This jet represents any internal jet within the array, and allows the heat transfer and flow characteristics of the entire array to be determined with a less computationally

intensive numerical model. The efficiencies that result from applying this technique to impinging jet arrays allows a much more detailed parametric study to be undertaken, compared with 'non-large' arrays or when using other modelling techniques.

1.2 Research Objectives

The objectives of the work presented in this thesis are presented below for both local heat transfer enhancement and uniform heat transfer enhancement.

1.2.1 Local Heat Transfer Enhancement

Objective

To determine the potential for heat transfer enhancement in a single impinging jet through the modification of the target surface geometry by introducing either

a. Highly conducting cone-shaped protrusions; or

b. Cylindrical Cavities

to the surface, centred on the jet axis.

1.2.2 Uniform Heat Transfer Enhancement

> **Objective**
>
> **To examine the effects of the geometric arrangement of a large array of impinging jets on the average heat transfer rate from a surface.**

1.3 Thesis Structure

The first part of this thesis, consisting of Chapters 2 and 3, reviews the relevant literature on jet impingement and discusses some numerical modelling considerations. Following on, Chapter 4 addresses in more detail a particular shortfall in turbulence modelling for impinging jet heat transfer. Chapters 5 and 6, present parametric studies on the two investigated local heat transfer enhancement schemes, addressing Objective 1.2.1, while Chapter 7, presents work conducted on arrays of impinging jets, addressing Objective 1.2.2. Finally, Chapter 8 summarises the conclusions on each of the three heat transfer enhancement schemes.

Chapter 2

Literature Survey of Jet Impingement

An extensive body of literature reports on the flow and heat transfer characteristics of impinging jets. This chapter identifies from the literature the prior research which is relevant to this thesis, while also reviewing other key publications in the area.

The review is divided into three sections. The first section covers numerical modelling considerations when simulating impinging jet heat transfer, in particular turbulence modelling. The second section reviews literature discussing enhancements to impinging jet heat transfer through modification of the target surface. The final section discusses literature detailing research on heat transfer from impinging jet arrays.

2.1 Numerical modelling

The numerical modelling techniques used in this work generally not unique to impinging jet heat transfer and are typically quite mature and well published. These techniques are discussed in Chapter 3. However, one topic still provides some difficulties when modelling impinging jet heat transfer. This is turbulence. Turbulence is an important element affecting impinging jet heat transfer and is consequently a topic of much interest to those researching impinging jets. From a numerical simulation perspective, the modelling of impinging jet turbulence has proved to be a particularly difficult problem. The difficulties stem from the fact that impinging jet flows are significantly different to the predominantly shear driven flows for which the most commonly used turbulence models have typically been developed. Impinging jet flows also exhibit complex transitions between near-laminar regions and regions of high turbulence. Initially the fluid exits the jet nozzle between laminar and fully-developed turbulent flow as determined by the upstream flow conditions and primarily the jet Reynolds number. As the fluid flows towards the impingement surface the turbulence dissipates, and a

minimal amount of turbulence occurs in the stagnation region. In the wall-jet region high shear stresses again promote turbulence generation, followed by further dissipation as the distance from the jet axis increases. It is these transitions which provide an additional difficulty in the accurate simulation of impinging jet heat transfer.

Research on impinging jet turbulence has therefore chiefly been carried out by two groups – those investigating impinging jets for their desirable heat transfer characteristics, and those developing general purpose turbulence models. For this reason there is a large amount of literature on impinging jet turbulence and heat transfer available, detailing both experimental and numerical work. These two topics are covered separately in sections 2.1.1 and 2.1.2.

2.1.1 Experimental Work

Martin [2] provides a thorough review and collation of early work into the heat and mass transfer characteristics of fluid jets impinging onto a flat target surface. A combination of analytical and experimental results were presented for these simple impinging jet systems as well as additional considerations for less straightforward (but more practical) configurations of impinging jets for heat and mass transfer processes. Correlations for both local and average heat transfer are presented for individual circular impinging jets, and a final section provides a discussion of behaviour of impinging jet arrays.

Baughn and Shimizu [3] conducted detailed experiments to determine the heat transfer from an impinging jet. Their aim was to overcome previous difficulties with correlating earlier experimental data by concentrating on an impinging jet with a fully developed flow profile prior to discharge. A single Reynolds number of 23,750 was studied at a range of jet-to-surface distances. The data from these experiments is a commonly used comparison dataset for numerical heat transfer results, including the work in this thesis and many of the papers discussed in Section 2.1.2.

Baughn, Hechanova, and Yan [4] used the same apparatus to conduct further measurements of heat transfer. In contrast to the above paper, this paper reported on the

heat transfer from an impinging jet in which the jet was heated rather than the surface. Measurements of heat transfer compared favourably with results for cases where the surface was heated, as long as suitable allowances were made for entrainment of surrounding air.

Jambunathan, Lai, Moss, and Button [1] performed a review of the available experimental data for single jet impingement over a large range of Reynolds numbers and jet-to-surface distances. Reynolds numbers between 5000 and 124,000 were investigated at jet-to-surface distances between 1.2 and 16 times the jet diameter. Their conclusions state that when correlating the local heat transfer rates for a single impinging jet the form of the correlation should be

$$\mathrm{Nu} = f(\mathrm{Re}, \frac{z}{d}, \frac{x}{d}, \mathrm{Pr})$$

though still further adjustment is needed if changes in nozzle geometry, confinement and upstream turbulence levels are also to be included. They present a detailed correlation for single impinging jet heat transfer covering a large range of experimental data published between 1962 and 1990.

Cooper, Jackson, Launder, and Liao [5] conducted flow experiments to determine the velocity fields for a fully developed impinging jet. These experiments were designed to acquire suitable data for evaluating the performance of various turbulence models. The numerical work is described in a companion paper by Craft, Graham, and Launder [6], which is discussed below.

Lee, Greif, Lee, and Lee [7] extended the available impinging jet data by measuring the heat transfer from an impinging jet over a lower range of Reynolds numbers, from 4000 to 14,400, at jet-to-surface distances between 2 and 10 times the jet diameter. The experimental heat transfer data from this work has been used in a number of other papers as a comparison dataset for evaluating heat transfer predictions from numerical simulations.

Nishino, Samada, Kasuya, and Torii [8] investigated the flow profiles of a turbulent

impinging jet using a combination of particle image velocimetry and particle tracking velocimetry. Their results indicated that in the near-wall region of an impinging jet the axial turbulence intensity was reduced, whereas the radial intensity was augmented. Using measurements of the turbulent stress anisotropy they found that the turbulence in the stagnation region is axisymmetric.

Ashforth-Frost, Jambunathan, Whitney, and Ball [9] studied a single impinging jet in both confined and semi-confined configurations at a Reynolds number of 20,000. Jet-to-surface distances between 1 and 8 jet diameters were considered and local heat transfer rates for the semi-confined case were presented. The change in the stagnation point heat transfer due to confinement was determined, with the semi-confined cases found to have consistently lower heat transfer compared with the unconfined cases. The highest heat transfer was found to occur at a jet-to-surface distance of 1 jet-diameter beyond the measured length of the potential core.

Sakakibara, Hishida, and Maeda [10] conducted experiments to determine both heat transfer and flow characteristics of an impinging slot jet using both digital particle image velocimetry and laser-induced fluorescence simultaneously. By correlating the vorticity to the turbulent heat flux, they concluded that amplification of vorticity was the most probable mechanism through which heat transfer was enhanced in the stagnation region of a single impinging jet.

Li and Garimella [11] collated earlier experimental work on heat transfer from impinging jets and developed a number of correlations to determine the stagnation point and average heat transfer. Their correlations are valid over a wide range of Reynolds numbers, jet heights and fluid properties, as indicated by the Prandtl number.

2.1.2 Numerical Work

Craft, Graham, and Launder [6] used an orthogonally impinging jet as test case for turbulence model assessment. Four models were examined, a low-Reynolds number k-ε model [12], a Reynolds Stress model, based on a second moment closure approach, and two alternative models also based second moment closure approaches.

The last three models differ from standard two-equation k-ε models by solving an additional transport equation for the turbulent shear stresses, $\rho\overline{u_i'u_j'}$. Results from these models were compared with experimental data from a companion paper by Cooper et al. [5] (discussed in Section 2.1.1). They highlighted poor prediction of heat transfer when using the low-Reynolds number k-ε model and the basic Reynolds Stress model, while the two alternative second moment closure models showed much better agreement.

Durbin [13] produced a paper describing the k-ε-$\bar{v}^2$ model, a model formulated based on a second moment closure approach (presented in full in an earlier paper [14]). The impetus for the development of the model was the poor prediction of turbulence models that were based on the two-equation k-ε formulation. The model, also known as the $\bar{v}^2$-f model, used two extra transport equations to account for the turbulent shear stresses in the flow in addition to the transport equations for turbulent kinetic energy, k, and turbulent dissipation, ε, from the standard k-ε model. A backwards facing step and a diffuser flow were simulated to validate the model. The results from these cases showed good agreement with experiments, though no comparison was made with results from the standard k-ε model. A further unsteady simulation of vortex shedding in the wake of a triangular prism was conducted and also showed good agreement with experimental results. The $\bar{v}^2$-$f$model is described in more detail in Chapter 3.

Durbin [15] followed this paper with a short technical note providing an explanation for the poor flow predictions of the k-ε model in stagnation point flows, including impinging jets, and proposed possible methods to overcome this anomaly.

Dianat, Fairweather, and Jones [16] presented another turbulence model based on a second moment closure approach. Comparisons were made for impinging jet and a two-dimensional channel flows. For impinging jet flows the k-ε model was again found to predict the mean and fluctuating velocities poorly, whereas the second moment closure model performed well.

Behnia, Parneix, and Durbin [17] studied numerically the heat transfer from an impinging jet using the $\bar{v}^2$-f model or the standard k-ε model. Comparisons with experi-

mental data were made for both models, and the $\overline{v}^2$-f model was found to predict both the heat transfer and velocity distributions with better agreement than the k-ε model.

Morris, Garimella, and Fitzgerald [18] numerically investigated a confined axisymmetric impinging jet where turbulence was modelled using a Reynolds stress turbulence model. Impinging jets at Reynolds numbers between 4000 and 23,000 were simulated, and the velocity fields compared with experimental data obtained using laser-Doppler velocimetry. Near-wall (closer than 1 jet-diameter) velocity measurements were not possible with their apparatus, however for the regions that were investigated they claimed good qualitative and quantitative agreement.

Behnia, Parneix, Shabany, and Durbin [19] published an additional paper, which investigated the heat transfer from an impinging jet at a range of jet-to-surface distances, including extremely low values (less than 1 jet diameter). A further two situations were also modelled: the effects of confinement on the heat transfer from an impinging jet; and also the heat transfer from a jet impinging on a pedestal of similar dimensions to the jet. Comparisons were made between the k-ε model and $\overline{v}^2$-f model, and again the k-ε model was found to drastically overpredict the heat transfer in the stagnation region, while the $\overline{v}^2$-f model provided good agreement with experimental results for both the flat surface and pedestal cases. From the flat surface results, they concluded that for jet-to-surface distances above 1 jet diameter, confinement has little effect on the heat transfer from an impinging jet, while at closer distances confinement causes the heat transfer from the surface to decrease.

Park and Sung [20] investigated heat transfer from an impinging jet using the standard k-ε turbulence model, the k-ε-$\overline{v}^2$ (or $\overline{v}^2$-f) turbulence model and an additional turbulence model which they labelled the k-ε-f_μ model. Again the poor performance of the k-ε model was highlighted, while good agreement with experimental heat transfer results was reported for both the k-ε-$\overline{v}^2$ and k-ε-f_μ models.

Merci and Dick [21] claimed that while the $\overline{v}^2$-f model showed good agreement with experimental results, the overhead of the additional transport equations in the model make it more time consuming and less straightforward than a two-equation

k-ε model. To address these concerns they formulated a modified k-ε model using a blended transport equation for ε and a cubic function for the turbulent stresses. Single impinging jets with jet-to-surface distances of between 1 and 14 jet diameters were modelled and showed good agreement with experimental data, similar to that of the $\overline{v}^2$-f model.

2.1.3 Summary

The previous sections highlight the significant effort directed towards understanding turbulence in impinging jets, both through experiment and numerical modelling. For numerical modelling, the k-ε model is commonly the first choice when the flow is expected to be turbulent and, for most flows, the predicted results show good agreement with experimental results. The literature reviewed in the previous section presents a significant case that the k-ε model is unsuitable for simulating impinging jet flows. This is further exacerbated when the heat transfer is also of interest.

The previous section also shows that there have been many attempts to develop an alternative turbulence model which can handle straightforward flows, while also accurately modelling impinging jet flows (and other edge cases). While a clear consensus is not reached over the best alternative turbulence model, the $\overline{v}^2$-f model stands out from the literature as a possible candidate for this role. In terms of the work presented in this thesis, the $\overline{v}^2$-f model also has the advantage of having been included in a number of commercial CFD codes. These points are investigated in more depth in Chapter 4 of this thesis.

2.2 Surface Modification

Impinging jets are employed to solve heat transfer problems across a wide range of industries. As such, many studies have been conducted in order to determine mechanisms and methods that enhance heat transfer even further. Modifying the target surface to enhance heat transfer is often desirable as implementation is possible with

minimal alteration to the remainder of the system. This section reviews the research pertinent to heat transfer enhancement achieved through surface modifications.

In 1996, Mesbah, Baughn, and Yap [22] experimentally investigated the change in heat transfer for an impinging jet when the target surface was changed from flat to concave. For their work a circular jet at a Reynolds number of 23,000 impinged on a concave hemispherical surface. The jet-to-surface distance was adjusted between 2 and 6 jet diameters. Comparison with earlier results for a flat surface showed heat transfer was higher for a concave surface than for a flat surface, which they attribute to slower development of the thermal boundary layer. However, when allowances were made for the effective area over which heat transfer took place, they concluded that a concave surface would not necessarily lead to a higher total Nusselt number when compared with a flat plate, as the curved surface has a larger area than the flat surface.

Lee, Chung, and Kim [23] investigated impinging jet heat transfer to a convex hemispherical curved surface. They studied a number of surface curvature ratios at Reynolds numbers from 11,000 to 50,000 and for jet-to-surface distances between 2 and 10 jet diameters. Local heat transfer was observed to increase with increasing curvature, however no adjustments were made for changes in heat transfer area. The authors attributed the increase in heat transfer to increased acceleration in the wall jet region.

In a later technical note, Lee, Chung, and Kim [24] extended their study to include higher Reynolds numbers, up to 87,000. In this paper they also included comparisons with a flat surface, and found that heat transfer is higher for a convex surface. As with Lee et al. [23] changes in the heat transfer area were not considered.

Beitelmal, Saad, and Patel [25] studied the effects surface roughness on impinging jet heat transfer. The ‘rough’ surface was constructed by adding a single ring of small protruding bumps at a radial distance of 3 jet-diameters from the jet axis. Reynolds numbers between 9600 and 38,500 were investigated and the jet-to-surface distance was varied between 1 and 10 jet-diameters. Heat transfer was found to be higher than for a flat plate at all Reynolds numbers and jet-to-surface distances, with a maximum

increase of 6 % recorded.

Ekkad and Kontrovitz [26] investigated the changes in heat transfer using a dimpled target surface. In their configuration, an array of jets in cross-flow impinged onto surfaces with dimples both aligned and staggered with respect to the jet axes. Reynolds numbers between 4800 and 14,800 were examined and the inclusion of dimples on the target surface was found to reduce heat transfer for both the staggered and aligned cases.

Yilbas, Shuja, and Budair [27] investigated a circular jet impinging onto a surface with a cylindrical cavity. They studied cavities of the same diameter of the jet, at various depths for a jet velocity of 100 m/s. Heat transfer from the base of the cavity was found to decrease as the depth of the cavity increased, whereas the heat transfer from the sides of the cavity increased with cavity depth. Overall heat transfer was lower when only the cavity base was considered, while it was higher if both the side and bottom of the cavity were included.

In a similar manner to the above paper, Yilbas, Shuja, and Budair [28] examined through numerical simulation the heat transfer and flow for a circular jet impinging into a conical cavity. The cavity diameter at the surface was maintained at the jet diameter, while the cavity depth was varied. Jet velocities of 50 and 100 m/s were simulated. The authors found that the local Nusselt number generally decreased as the cavity depth increased.

2.2.1 Summary

The preceding section presents relevant previous work investigating jet impingement heat transfer from modified surfaces. The effects of the modifications were mixed, with both increases and reductions in heat transfer reported. Reviewing the literature also highlighted the novel nature of the enhancement techniques presented in this thesis, with investigations or proposals of similar methods non-existent. Due to this absence, evaluation of the heat transfer enhancement potential of surface modifications such as protrusions and cavities, provides a significant contribution to this area.

2.3 Impinging Jet Arrays

Impinging jet arrays have often been adopted for heat transfer problems where the highly localised nature of heat transfer from a single jet is undesirable. Application examples include turbine blades, electronic microchips and metal quenching, amongst others. The industrial benefits of impinging jet arrays has naturally led to a huge number of publications into the associated heat transfer characteristics. This section reviews the key research relevant to the impinging jet array investigations described in Chapter 7.

Goldstein and Timmers [29] determined the heat transfer from an array of 7 jets using liquid crystal thermography for jet heights of 2 and 6 jet diameters. A single Reynolds number of 40,000 was considered.

Florschuetz, Metzger, and Su [30] experimentally investigated an array of confined impinging jets with initial cross-flow and constrained to exit in one direction. Heat transfer in terms of Nusselt number was presented for a range of configurations.

Florschuetz and Su [31] extended this work to include the effects of crossflow temperature. They found that 'flow history', for both temperature and crossflow conditions, could significantly alter the heat transfer from an array of impinging jets.

Obot and Trabold [32] also studied jet arrays in crossflow of varying strength and developed correlations to determine heat transfer. They found the highest heat transfer occurred with minimum crossflow and that as jet-to-jet spacing was decreased heat transfer increased. Reynolds numbers between 1000 and 21,000 were considered at jet-to-jet spacings between 2 and 16 jet diameters.

Huber and Viskanta [33] investigated the convective heat transfer from a confined array on impinging circular jets. Jet heights of 0.25, 1.0 and 6.0 jet diameters were studied for a range of Reynolds numbers between 3500 and 20,400. They investigated a 3 x 3 array of jets with and without exits for spent air. They found the maximum heat transfer occurred when a jet-to-jet spacing of 4 jet diameters was used. This spacing was the lowest spacing considered in their paper. They further concluded that including

exits for the spent-air significantly increased the uniformity of heat transfer from the array.

San and Lai [34] studied a staggered array of impinging jets in order to determine the optimum jet-to-jet spacing to give maximum heat transfer. Reynolds numbers of 10,000, 20,000 and 30,000 were considered. Their experimental array consisted of five jets with spent fluid exiting from the sides of the apparatus. The stagnation point Nusselt number was used as the performance measure and the optimum spacing was found to be between 8 and 12 jet diameters with nozzle-to-surface spacings between 2 and 6 jet diameters considered.

Brevet, Dejeu, Dorignac, Jolly, and Vullierme [35] studied the heat transfer from both a single row of jets and three rows of jets in order to optimise the spacing. They found that average Nusselt number generally increased as jet-to-jet spacing decreased, with the maximum occurring with a spacing between 2 and 3 diameters. When the total flow rate was constrained, the jet-to-jet spacing for maximum heat transfer was found to occur between 4 and 5 jet diameters.

Rhee, Yoon, and Cho [36] investigated the heat transfer characteristics of an impinging jet array with and without crossflow using naphthalene sublimation. The jet array was confined to exit in one direction and the effect of adding effusion holes for spent-air investigated. They found that for small nozzle-to-surface spacings the effusion holes resulted in enhanced heat transfer from the array.

Aldabbagh and Sezai [37] conducted numerical simulations of a 3 x 3 array of square laminar jets with spent fluid removal. Reynolds numbers up to 500 were studied and the maximum heat transfer was found to occur at the lowest jet-to-jet spacing investigated.

Yan, Mei, Liu, Soong, and Yang [38] experimented with an array of elliptic jets with spent fluid exiting through both ends of the domain. Heat transfer was measured using liquid crystal thermography. A constant spacing between the jets was investigated, however the shape of the individual jets was altered. While crossflow was an important consideration in their study, a number of their results are valid for compari-

son to an array in the absence of crossflow. Reynolds numbers of 1500, 3000 and 4500 were studied.

Thielen, Jonker, and Hanjalić [39] conducted numerical simulations on a three by three square array of jets and a nine jet circular array. Simulations were conducted using both $\overline{v}^2$-f and k-ε turbulence models. A limited number of heat transfer results were presented, with similar findings to other jet array investigations. In preparing their domains for simulation, the authors utilised only two of the three symmetries existing in their arrays. A consequence of this treatment was that for the square array the flow was not symmetric about the unused symmetry. They found that in most cases heat transfer was not significantly affected by the symmetry breaking.

2.3.1 Summary

The previous section presented investigations into heat transfer from arrays of impinging jets. Investigations typically considered only a limited range of parameters. As such, there is still a need for more extensive research into the heat transfer from impinging jet arrays. With the development of more extensive correlations the application of impinging jets to a wide range of industrial problems would be aided significantly. The research discussed in Chapter 7 of this thesis presents correlations for the heat transfer from impinging jet arrays over a large parameter space and contributes to the existing work in this field.

Chapter 3

Numerical Flow Modelling

In Chapter 1 two main approaches for improving impinging jet heat transfer were introduced, based on either increasing the local heat transfer rates or increasing the uniformity of the heat transfer distribution. To investigate if these techniques are beneficial, parametric studies were conducted to determine the characteristic heat transfer rates for each of the three schemes, for a number of different configurations. These studies were made by conducting a series of numerical simulations for each proposal. This chapter discusses the necessary considerations when conducting these simulations.

The fundamental equations describing fluid flow are the Navier-Stokes equations. These equations are highly coupled and non-linear and as a result only a limited number of flows lend themselves to an analytical solution. Even for this small number of flows, well defined boundary conditions are required, in addition to other simplifying assumptions. This means that many of the flows of interest to engineers do not readily lend themselves to a purely analytical approach, as these typically involve complex geometries in conjunction with complex flow interactions. For these types of flow, which include impinging jets, a numerical approach is often the chosen option as numerical studies are generally cheaper and faster than an equivalent experimental investigation.

The underlying mathematical techniques for performing numerical simulations of fluid problems are quite mature, though until recently the computer codes implementing these techniques were typically developed for a particular flow problem or class of flow problem. Within the last two decades or so, general purpose numerical solvers became feasible due mostly to increasing availability of raw computing power. These solvers are now seeing widespread use in industry and academia for both research and design. The chief advantage of general purpose solvers is through removing duplication of programming effort (and associated testing and bug fixing), allowing the same code to be reused for a number of different problems. From a fluid dynamicist's per-

spective this is advantageous as the fluid dynamicist is now free to concentrate on the problem at hand rather than the programming. For this reason the work presented in this thesis makes use of the commercial computational fluid dynamics (CFD) code FLUENT [40].

While the separation of the researcher from the code is advantageous, it can also mean that the large number of assumptions that (necessarily) underly a general purpose solver can be left by the wayside. This is a disadvantage that must be avoided by ensuring the researcher has an in-depth understanding of the methods and techniques used in a general purpose CFD code. Without this knowledge accurate and precise results cannot be guaranteed. The following sections provide a brief overview of some of the major considerations in using a general purpose numerical code.

3.1 Discretization

The Navier-Stokes equations apply to a fluid continuum. Before these equations can be solved numerically they must be transformed into a system of discrete equations. This process, called discretization, is typically achieved using finite difference or finite volume techniques.

Both techniques are similar, and in both cases discretization requires subdividing the solution domain into a number of discrete regions and applying the governing equations to each. A control volume approach has a number of advantages for discretization, notably that complex geometries or irregular grids are handled easily while at the same time conservation of mass and momentum is guaranteed. In contrast, a finite difference approach better lends itself to higher order interpolation schemes if required. In both cases a number of different solution algorithms are available to solve the resulting system of equations. Discretization is important as correct discretization of the domain plays an extremely important part in obtaining accurate results from a numerical solution and can mean the difference between accurate results and nonsense.

For control volume based codes triangular or quadrilateral cells are typically used

for two-dimensional problems, while three-dimensional problems make use of tetrahedral, hexahedral or prismatic cells. The choice of cell shape depends chiefly on the geometry, where triangular or tetrahedral meshes are better suited to meshing complex geometries and simple geometries lend themselves to regular (structured) quadrilateral or hexahedral meshes. Structured meshes are favoured where possible as higher accuracies are possible for the same number of cells (as a consequence of interpolating between cell centre values and face values for each cell) [41]. Depending on the desired mesh type, many grid generating algorithms are available, though the actual algorithm used has minimal effect on accuracy of the final grid. In any case, a suitable grid can be ensured by performing two operations – a grid independence study and boundary layer refinement. These are discussed in the following sections.

3.1.1 Grid independence

The discretization process unavoidably introduces errors in a numerical solution by approximating a continuous field by a discrete one. These errors are greatest in regions where the gradients are highest and this is generally taken this into account by making the grid finer in regions where high gradients are expected, for example regions where abrupt changes in geometry take place or near to solid surfaces.

While initial consideration of the expected flow is useful, a refinement process is still necessary to ensure that the errors in the solution due to discretization are below a certain threshold. This process consists of refining the grid, usually by doubling the mesh density, and obtaining a further solution on the finer grid. If the difference between the results from the original grid and the refined grid are within a prescribed limit then the original grid can be considered as giving results to the desired accuracy. If the difference between the two sets of results is greater than this limit, then the refined grid takes the place of the original grid and new refined grid is created. This procedure is repeated until the error between two successive solutions is within the originally prescribed error limit. A solution obtained from a mesh that has been refined in this way is said to be ‘grid independent’.

The above refinement process is generally sufficient to ensure that errors in the results are below the required threshold. In cases where turbulence modelling techniques are applied further checking of the mesh in boundary regions is also warranted.

3.1.2 Boundary Layer Refinement

For laminar flows a grid can generally be considered suitable following the refinement process described in the previous section. However when modelling turbulent flows, especially those where heat transfer is included, additional factors must be considered in conjunction with the refinement process to account for the treatment of the flow near surfaces. When modelling turbulence there is generally two approaches that can be taken to treat these near-wall flows. One requires the turbulence model to be developed in such a way as to be valid right up to the wall, while the other uses a separate model to account for the near-wall region. These two methods generally place different requirements on the fineness of the grid near a surface.

The fineness of a grid near a wall can be measured by calculating the non-dimensional distance from the wall, y^+, defined as

$$y^+ = \frac{\rho u^* y}{\mu} \tag{3.1}$$

where u^* is the friction velocity, $u^* = \sqrt{\tau_0/\rho}$ [42].

In a simulation where a turbulence model is used the value of y^+ at the walls must be checked to determine if the near wall mesh is adequate, where the suitable range of y^+ values depends on the method used to account for turbulence in the near-wall flow.

For the first method, those where the turbulence model is valid right up to surfaces, the required y^+ value of the cells adjacent to the wall should be approximately 1. This ensures that the first cell centre is within the laminar sub-layer. It is also desirable to have at least ten grid cells within the laminar region, or $\mathrm{Re}_y < 200$, where Re_y is the Reynolds number based on the distance of the cell from the wall.

The second method for accounting for the near wall flow requires a separate model

for the regions near a surface to be used. This model is usually either a single function to directly determine the flow characteristics in the near wall cell, or a separate low Reynolds number model that accounts for the boundary layer flow in the laminar sub-layer in a similar manner to the first method.

The single function or 'wall function' approach typically uses the standard logarithmic approximation of the boundary layer [42]. In this case the cell centre y^+ values in the cells adjacent to a surface must be between 30 and 300 to ensure the cell centre is in the logarithmic region of the turbulent boundary layer. This implies a lower bound on the value for y^+ and as such the cell size near the wall will also have a minimum value. When this limit is reached in a cell further refinement is not possible without breaking the validity of the wall function model. This can cause problems when refining a grid since the refinement process can cause the cell size near the wall to decrease below the minimum size.

Where a laminar sub layer model is used the requirements mimic those for the first method. In this case the cell centre y^+ value in the cells adjacent to surfaces should be approximately 1 and a minimum of ten cells should be within the laminar region, $\mathrm{Re}_y < 200$.

3.2 Solution Algorithms and Interpolation Functions

A number of solution algorithms have been created to allow the Navier-Stokes equations to be solved numerically. These algorithms are generally quite complex and are often designed around certain types of flow. The two most common are the 'Semi Implicit Method for Pressure Linked Equations' or SIMPLE algorithm of Patankar [43], and the 'Pressure-Implicit with Splitting of Operators' (PISO) scheme of Issa [44] though many others exist. In most cases the choice of algorithm does not affect the results, rather the simulation run time or memory usage, and as such no further discussion is warranted.

On the other hand the choice of interpolation function can affect the results. Nu-

merical codes generally store the values of the flow variables at the cell centres, while solution algorithms typically require values at the cell faces also. To determine the face values requires a function to interpolate the variable between cell centres. As with solution algorithms many different interpolation schemes are possible, and the most common are the first and second order upwind schemes. These two schemes calculate the diffusion component of the value of the flow variable on the face using standard first (or second) order approaches, while the convection component is weighted towards the value of the upstream cell. Upwinding generally gives better results than a standard interpolation scheme for flows dominated by convection.

Second order upwind schemes provide much better accuracy than their first order equivalents and should be used where possible. From practical standpoint, higher order schemes are more likely to suffer stability problems and it is usual for steady-state simulations to perform a number of iterations of a lower-order scheme to initialise the flow field. Other interpolation schemes are not used in this work and readers are directed to Versteeg and Malalasekera [41] for more in-depth discussion.

3.3 Turbulence Modelling

Impinging jets are an example of a physical system that is particularly difficult to model correctly. This is due principally to the high streamline curvature present in impinging jets combined with complex transitions between laminar and turbulent flow.

Turbulent flows can be categorised as flows where inertial forces in the fluid dominate the viscous forces in a flow, indicated by the Reynolds number. Turbulent flows exhibit irregular, rapid fluctuations in velocity and pressure as small-scale eddies and larger flow features interact. These interactions promote mixing in the fluid and as a result turbulence in the flow is generally desirable for heat transfer applications.

This section introduces accepted finite volume methods for accounting for turbulence when conducting numerical simulations. Particular emphasis is paid towards applicability to modelling impinging jet heat transfer. Chapter 4 continues the discus-

sion with a detailed investigation into the suitability of general purpose RANS models for modelling turbulence in impinging jet heat transfer.

3.3.1 The Need for Turbulence Modelling

The complete Navier-Stokes equations apply equally to both laminar and turbulent flows, and theoretically there is no need to account for turbulence separately. Direct numerical simulation (DNS), for example, solves the complete Navier Stokes equations without the need for turbulence modelling. While DNS has been used successfully to simulate turbulent flows in simple geometries, it is currently not feasible when simulating medium to high Reynolds number flows in arbitrary geometries.

Turbulent flows are inherently three dimensional and time dependent. As a consequence many assumptions which simplify a flow problem are prohibited when using direct numerical simulation. For example assumptions concerning the dimensionality or steady state nature of a flow cannot be made, even where these assumptions are valid. This means that every DNS problem will be three-dimensional and time-dependent, an expensive exercise in both time and computational resources.

Additionally, in medium to high Reynolds number flows turbulent features occur over a large range of scales, with the smallest scale typically many orders of magnitude less than the characteristic dimensions of the flow. Direct numerical simulation of these flows therefore requires extremely fine grid sizes to be used as the mesh must be fine enough to adequately capture the turbulent features occurring over the complete range of scales.

The above comments are related to the practicality of DNS, and with the continuing increases in computing power DNS be feasible in the future for a much larger range of flow problems. There are other reasons for avoiding DNS however.

Researchers are often only concerned with the bulk flow behaviour in a problem, especially when a problem is an engineering problem. While more complex analyses are often conducted, these are usually only considered if the predicted flow differs greatly from the observed flow. As the bulk behaviour of the flow is the major concern,

the vast amount of data generated by a full three dimensional unsteady simulation is essentially wasted and is post-processed to extract this behaviour before analyses or comparisons are made. For these problems a DNS approach is not needed. In addition, CFD for design purposes is applied iteratively - by comparing the performance of proposed designs as design variables are varied over a range of values. For parametric analyses like these any shortfalls in a particular modelling technique will generally affect all designs similarly, and results still provide valuable information for design development, even though the actual performance may vary from the predicted performance.

For these reasons including turbulence through modelling is usually the pragmatic choice.

3.3.2 Numerical Methods for Modelling Turbulence

The most widely employed turbulence models are based on the Reynolds-Averaged Navier-Stokes (RANS) equations. These are derived by considering all the velocity components as a combination of a bulk velocity component and a fluctuating velocity component, as

$$u = \bar{U} + u' \tag{3.2}$$

After making the substitution into the Navier-Stokes equations and simplifying the resulting set of equations is averaged and the following system of equations is obtained.

$$\frac{\partial}{\partial t}\left(\rho \bar{U}_i\right) + \frac{\partial}{\partial x_j}\left(\rho \bar{U}_i \bar{U}_j\right) = \\ -\frac{\partial p}{\partial x_i} + \frac{\partial}{\partial x_j}\left[\mu\left(\frac{\partial \bar{U}_i}{\partial x_j} + \frac{\partial \bar{U}_j}{\partial x_i} - \frac{2}{3}\delta_{ij}\frac{\partial \bar{U}_i}{\partial x_i}\right)\right] + \frac{\partial}{\partial x_j}\left(-\rho\overline{u_i' u_j'}\right) \tag{3.3}$$

As can be seen, the RANS equations are similar to the original Navier-Stokes equations, except that the absolute velocity components are replaced by the bulk velocity components. There is one additional term though, the Reynolds stress term, $-\rho\overline{u_i' u_j'}$.

When modelling turbulence it is this term that is referred to, and these stresses that must be modelled in order to close the system of equations.

Boussinesq Models

The Boussinesq turbulence models provide the simplest method for closing the system of equations. These models assume the Reynolds stresses to be homogeneous and the $-\rho\overline{u_i'u_j'}$ term is replaced by an additional viscosity term, μ_t, such that

$$-\rho\overline{u_i'u_j'} = \mu_t\left(\frac{\partial u_i}{\partial x_j}+\frac{\partial u_j}{\partial x_i}\right)-\frac{2}{3}\left(\rho k+\mu_t\frac{\partial u_i}{\partial x_i}\right)\delta_{ij} \tag{3.4}$$

This is in line with an intuitive understanding of turbulence as additional diffusion in the flow. Various Boussinesq models have been developed, with the differences between each based on the method for calculating this additional viscosity term and the transported turbulence properties.

k-ε model

The k-ε turbulence model is probably the most widely used RANS turbulence model and as a result has been validated against a wide range of different flows. Essentially the k-ε model introduces two additional flow variables to account for turbulence, the turbulent kinetic energy, k, and the turbulent dissipation rate, ε. These are flow variables and as such two additional transport equations are needed, one each for k and ε . These transport equations are included in Appendix B. The turbulent viscosity is calculated from

$$\mu_t = \rho C_\mu \frac{k^2}{\varepsilon} \tag{3.5}$$

The transport equations are generally not valid for the near-wall region and a separate near wall model is required, as described in Section 3.3.3

Low Reynolds Number k-ε models

Low Reynolds number k-ε turbulence models are a class of turbulence models based on the standard k-ε model that use a variety of damping functions to account

for low-Reynolds number (or near-wall) regions of flow. In these models the kinetic energy and dissipation equations remain the same as in the standard k-ε model for the far field flow. An example of one such model is the low-Reynolds number model of Yang and Shih [45]. A vast number of these models exist in the literature, mostly developed for specific applications.

k-ω model

The k-ω model is also a two equation model, however the turbulence dissipation rate, ε, is replaced by the specific dissipation rate, ω, such that

$$\omega = \frac{\varepsilon}{k} \tag{3.6}$$

The turbulent viscosity is then calculated as

$$\mu_t = \alpha^* \frac{\rho k}{\omega} \tag{3.7}$$

where α^* is an additional coefficient to account for low Reynolds number flows. The full set of transport equations for the k-ω model are included in Appendix B.

$\overline{v}^2$-f model

The $\overline{v}^2$-f model is again based on a similar approach to the k-ε model. However in the $\overline{v}^2$-f model two additional quantities are introduced, a velocity scale, $\overline{v}^2$, and a redistribution variable, f, which accounts for the redistribution of turbulence from the streamline direction to the wall normal direction. For the $\overline{v}^2$-f model the turbulent viscosity, μ_t, is dependent on the velocity scale, $\overline{v}^2$, and a time scale, T, whose derivation is included in Appendix B. The turbulent viscosity is calculated from

$$\mu_t = \rho C_\mu \overline{v^2} T \tag{3.8}$$

$\overline{v}^2$ can also be considered as the velocity fluctuation normal to the streamline direction [17]. Again the full set of transport equations for the $\overline{v}^2$-f model are included in Appendix B.

Reynolds Stress Models

The Reynolds stress turbulence model, while still based on the RANS equations, removes the assumption about the homogeneity (and isotropy) of the turbulence in the flow. This requires solving transport equations for each of the Reynolds stress components in addition to the dissipation rate. As a result five additional transport equations need to be solved for a two dimensional problem while seven additional equations are required for a three dimensional problem. To account for near wall flows the boundary conditions are derived using a separate wall model, using a similar approach to the k-ε turbulence model. The complete set of transport equations are included in Appendix B.

3.3.3 Near Wall Models for Turbulent Flows

Many turbulence models, especially those based on the standard k-ε model, are derived for the bulk flow region, and are known to be invalid for the near wall regions. In order to account for the flow near walls, a separate model is used for wall boundaries. This model is either a single function providing the turbulence parameters in the wall-adjacent cell, commonly called the 'wall-function' approach, or a separate near wall model that completely resolves the near wall flow.

The single function or 'wall function' approach uses a standard logarithmic approximation of the boundary layer with the boundary layer described by

$$U^* = \frac{1}{\kappa} \ln(Ey^*) \tag{3.9}$$

where U^* and y^* are the mean velocity and distance from the wall respectively. Substituting these into Equation 3.9 gives

$$\frac{UC_\mu^{1/4}k^{1/2}}{\tau_w/\rho} = \frac{1}{\kappa} \ln\left(E\frac{\rho C_m u^{1/4}k^{1/2}y}{\mu}\right) \tag{3.10}$$

which relates the turbulent kinetic energy, k, to the distance from the wall, y, and the

mean velocity, U. The remaining terms are constants which are derived empirically (C_μ, κ, E) or fluid properties (ρ, μ). Equation 3.10 allows the correct turbulence properties to be set in the near-wall region.

3.3.4 Turbulence Modelling in Impinging Jets

Due to their unique flow characteristics impinging jets provide a particularly difficult problem for turbulence models, predominantly due to the transitional nature of the flow. In an impinging jet, the flow at the exit of the jet nozzle starts somewhere between partially and fully-developed turbulent flow depending on the upstream conditions. The turbulence in the flow dissipates somewhat, transitioning back to near laminar conditions in the stagnation region. In the wall-jet region turbulence production increases again followed by further dissipation as the distance from the jet axis grows. In addition to these transitions, the high curvature of the streamlines introduces some anisotropy in the flow and creates additional modelling difficulties.

Inaccuracies in predicting near wall flow, and subsequently the heat transfer, have been reported often in the literature with Cooper et al. [5], Behnia et al. [19, 46] and Craft et al. [6] amongst many reporting this. However consideration of these papers together fails to identify a clearly better turbulence model for predicting impinging jet heat transfer. The next chapter addresses this by investigating the predicted heat transfer from an impinging jet for a number of RANS turbulence models. Comparison of these results with a number of published data allowed a suitable model to be identified for the later work presented in this thesis.

Chapter 4

Impinging Jet Turbulence Modelling

Impinging jets are an inherently turbulent phenomena, and as such it is necessary to include turbulence in any numerical modelling attempts. As discussed in the previous chapter, Reynolds-Averaged Navier-Stokes (RANS) turbulence models correlate well with experimental results, in addition to providing a suitable balance between accuracy and computational expense. For impinging jet flows however, these same models often poorly predict the flow characteristics, and in particular the heat transfer.

While it is generally acknowledged that the standard RANS turbulence models, such as the k-ε model, give inaccurate heat transfer predictions for impinging jets, there is no clear consensus on the most suitable alternative model (or models). The aim of the work presented in this chapter was to identify and evaluate the candidate RANS turbulence models, in order to select the best model for predicting the heat transfer from an impinging jet. The identification of the $\overline{v}^2$-f model as the most accurate model provided a solid foundation for the results presented the remainder of this thesis.

4.1 Turbulence Models

The candidate turbulence models for comparison were drawn firstly from those which have seen widespread use in flow modelling, while these were supplemented with two additional low-Reynolds number models. The first group of models consisted of the standard k-ε model [12], the k-ω model [47] and the Reynolds Stress Model (RSM) [48–50]. The two low-Reynolds number models were the low-Reynolds number k-ε model of Yang and Shih [45] and the $\overline{v}^2$-f model [13]. The standard k-ε model, k-ω model and RSM model are available in the standard FLUENT CFD package, the low-Reynolds number k-ε model is included in the standard package but must be selected through an expert interface, while the $\overline{v}^2$-f model is available with an additional

license. The standard k-ε model and the Reynolds Stress model required separate near wall treatment, and a wall function model was used for both.

4.2 Methodology

The test geometry for the turbulence model evaluation consisted of a single circular jet impinging orthogonally onto an isothermally heated flat plate. This test case was chosen to suit the available experimental data. A two-dimensional axisymmetric jet was modelled to take advantage of the rotational symmetry present in the problem. To compare the performance of each of the models, the local Nusselt number for the heated wall was calculated for each simulation and compared with available experimental data. Simulations were also conducted at intermediate Reynolds numbers to allow any additional trends in the models to be identified. The successful models were those that showed good agreement with the experimental results when comparing the predicted local heat transfer at the wall. Four experimental datasets were available to compare with the numerical results, those of Baughn and Shimizu [3], Baughn et al. [4], Cooper et al. [5] and Lee et al. [7].

4.3 Simulation Parameters

The simulation parameters were selected to match closely available experimental results where possible to allow more valid comparisons to be made between the models. The variables considered for investigation were the jet-to-surface distance, z, and the jet velocity, V. These variables were non-dimensionalised with respect to the jet diameter and the values used for simulations are given in Table 4.1. Experimental data was available for Reynolds numbers of 6500 and 23,000, at jet-to-surface distances, z^*, of 2, 4 and 6.

Parameter	Variable	Non-dimensionalised	Values
Jet-to-surface height	z/d	z^*	2, 4, 6
Jet Velocity	$\rho V d/\mu$	Re	6500, 10,000, 23,000, 30,000

Table 4.1: Parameter ranges for turbulence model investigation

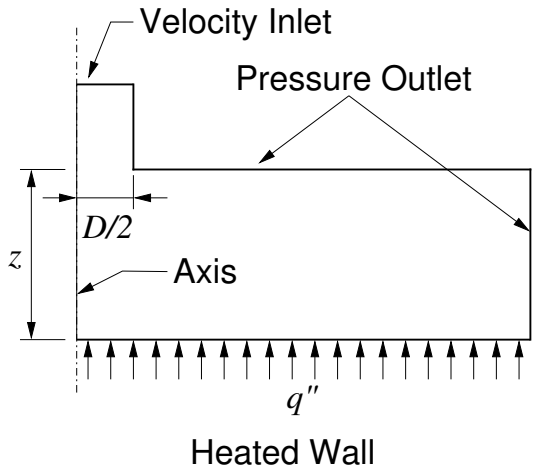

Figure 4.1: Solution Domain

4.3.1 Computational Domain

A diagram of the problem domain is shown in Figure 4.1. The computational domain extended to 8 jet-diameters from the jet axis with an additional portion of the jet nozzle included in the domain to capture any flow variations that may have occurred within the nozzle exit region.

4.3.2 Boundary Conditions

The boundary conditions for the simulation were selected to best match the conditions for which the experimental data was obtained. The heated wall was considered to be isothermal with a temperature difference of 25^{o}C above the jet inlet temperature. The outlet boundaries were treated as pressure outlet conditions, with a reference pressure of zero at the boundary. For the jet inlet boundary a fully developed flow profile was used, wherein the profiles for the turbulent quantities, velocity and pressure were obtained from an independent numerical model of a long tube. These inlet flow profiles

were obtained for Reynolds numbers of 6500, 17,000, 23,000 and 34,000 to allow comparison with the experimental data [3–5, 7]. All wall surfaces were considered to be no-slip.

4.3.3 Mesh Generation

A regular quadrilateral mesh was constructed over the domain with finer grid spacing used adjacent to the heated surface to allow accurate representation of the boundary layer flow. Grid independence of the mesh was established in accordance with the process outlined in Chapter 3, while the boundary layer mesh was refined so that the boundary cell centre y^+ values along the heated wall were within the required limits for each of the models. The results presented for each of the investigated turbulence models were calculated on the refined meshes.

4.4 Results

Figures 4.2 to 4.5 show the local surface Nusselt number distributions for a jet-to-surface distance of 2 jet-diameters at Reynolds numbers of 6500, 10000, 23000 and 30000. Figures 4.6 to 4.9 show the local Nusselt number for a jet to surface distance of 4 jet diameters while figures 4.10 to 4.13 show the Nusselt number when the jet discharges 6 jet diameters above the surface. Superimposed on these figures are the experimental data of Baughn and Shimizu [3], Baughn et al. [4], Cooper et al. [5] and Lee et al. [7].

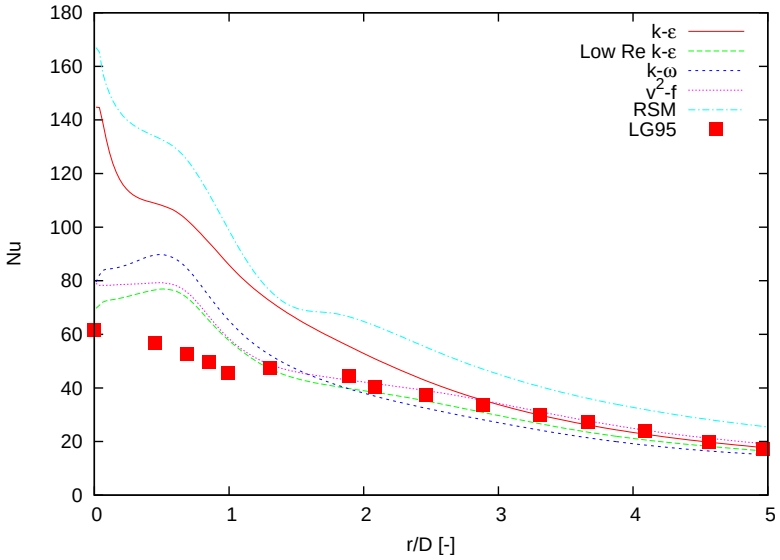

Figure 4.2: Surface Nusselt Number, $z = 2$, Re = 6500 (LG95 - Lee et al. [7])

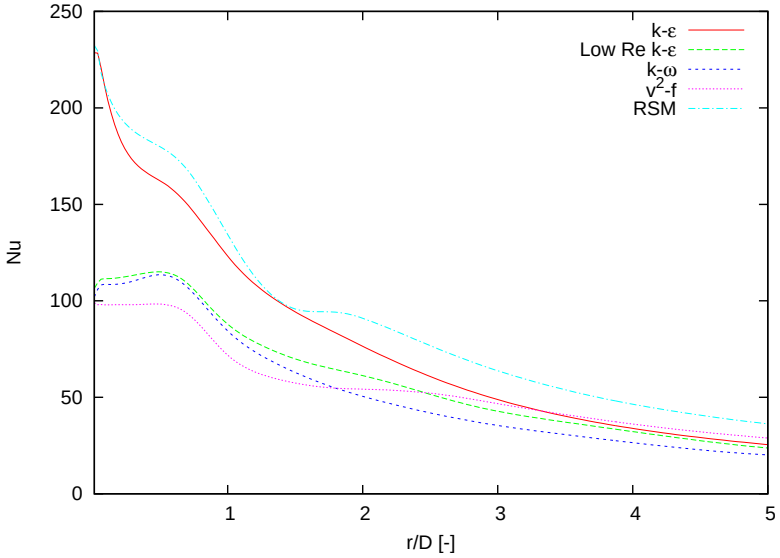

Figure 4.3: Surface Nusselt Number, $z = 2$, Re = 10000

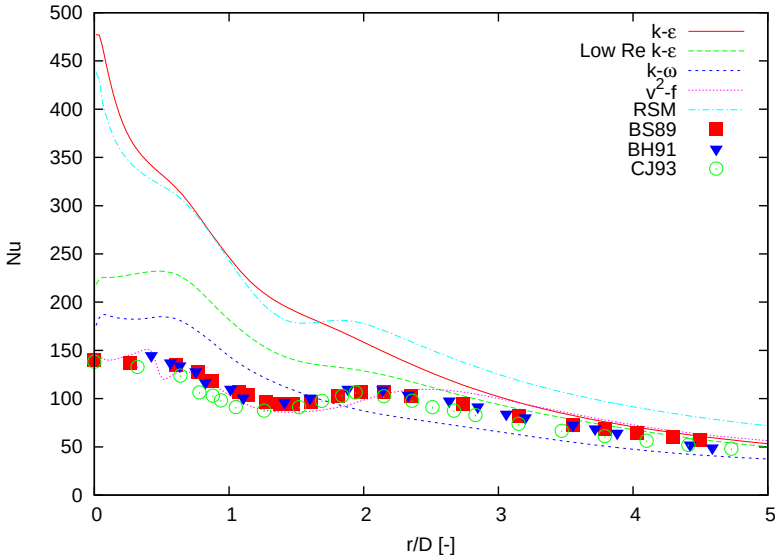

Figure 4.4: Surface Nusselt Number, z = 2, Re = 23000 (BS89 - Baughn and Shimizu [3], BH91 - Baughn et al. [4], CJ93 - Cooper et al. [5])

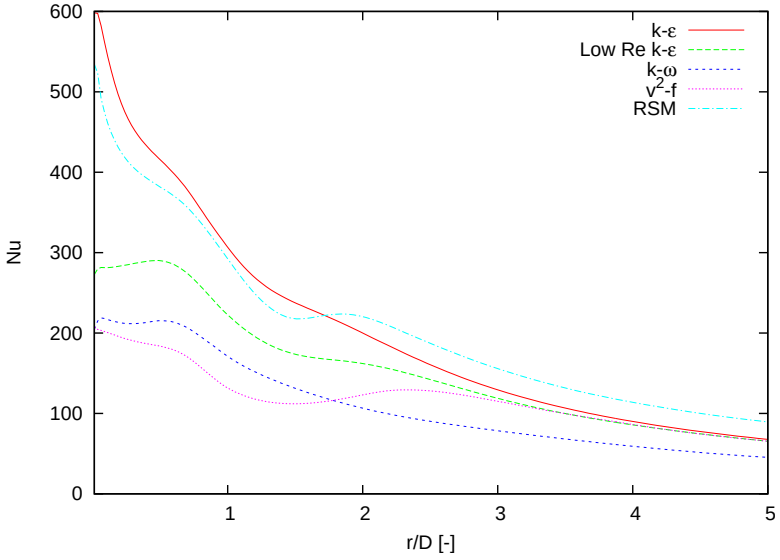

Figure 4.5: Surface Nusselt Number, z = 2, Re = 30000

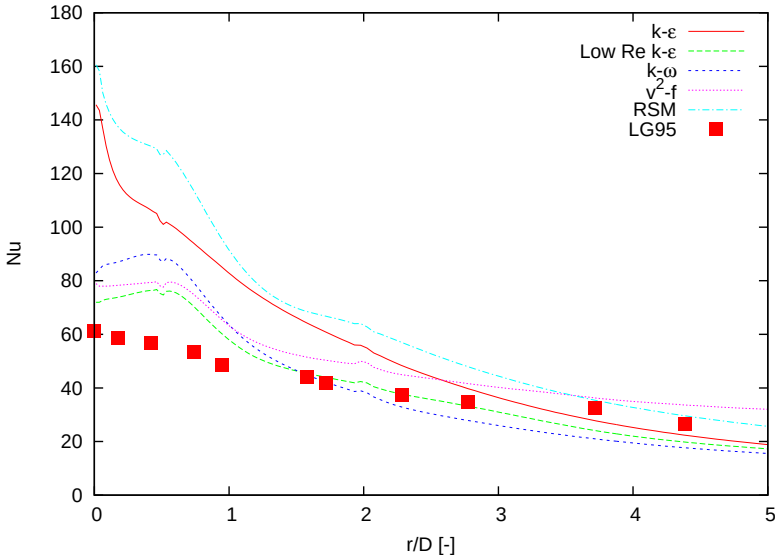

Figure 4.6: Surface Nusselt Number, $z = 4$, Re = 6500 (LG95 - Lee et al. [7])

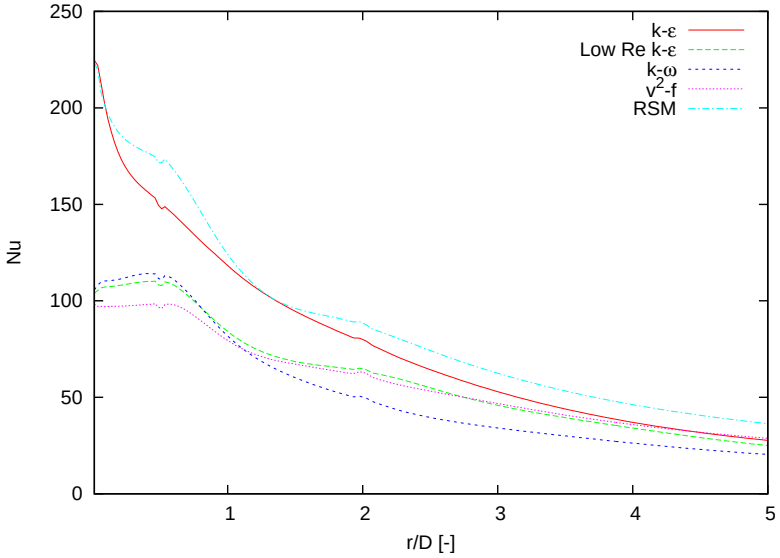

Figure 4.7: Surface Nusselt Number, $z = 4$, Re = 10000

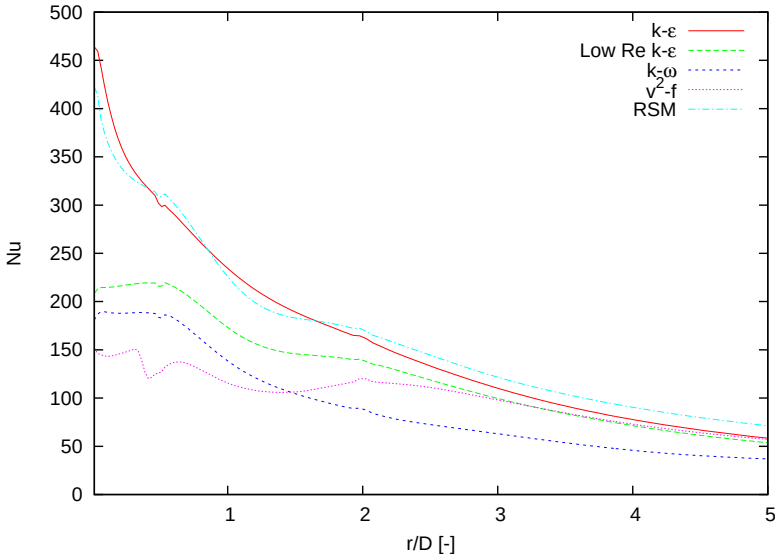

Figure 4.8: Surface Nusselt Number, $z = 4$, Re = 23000

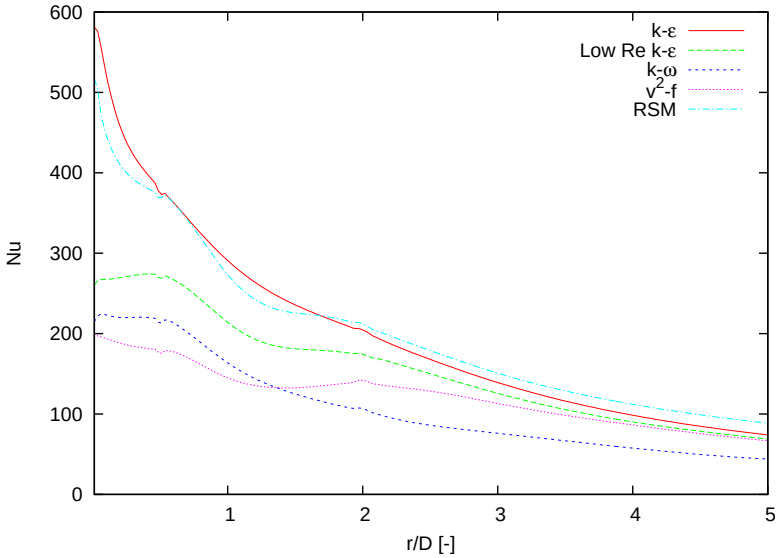

Figure 4.9: Surface Nusselt Number, $z = 4$, Re = 30000

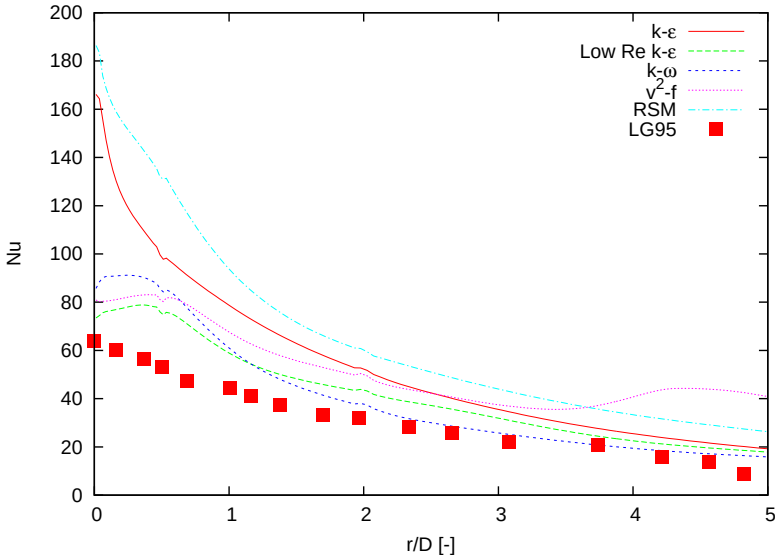

Figure 4.10: Surface Nusselt Number, $z = 6$, Re = 6500 (LG95 - Lee et al. [7])

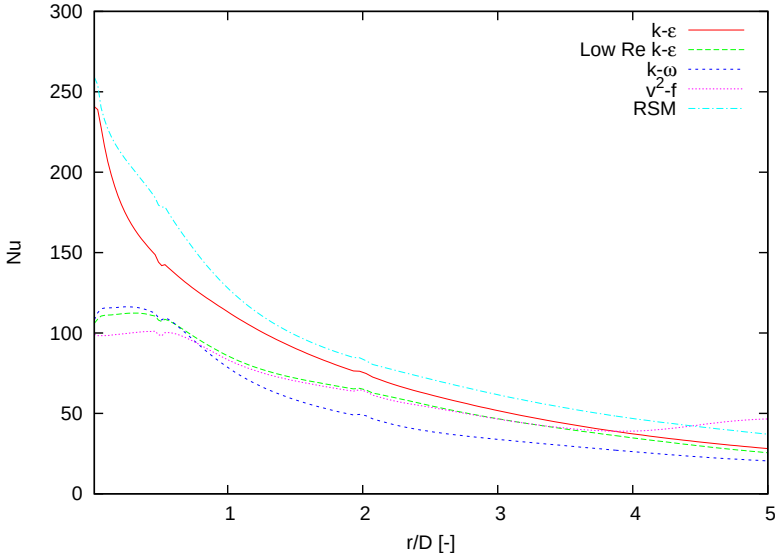

Figure 4.11: Surface Nusselt Number, $z = 6$, Re = 10000

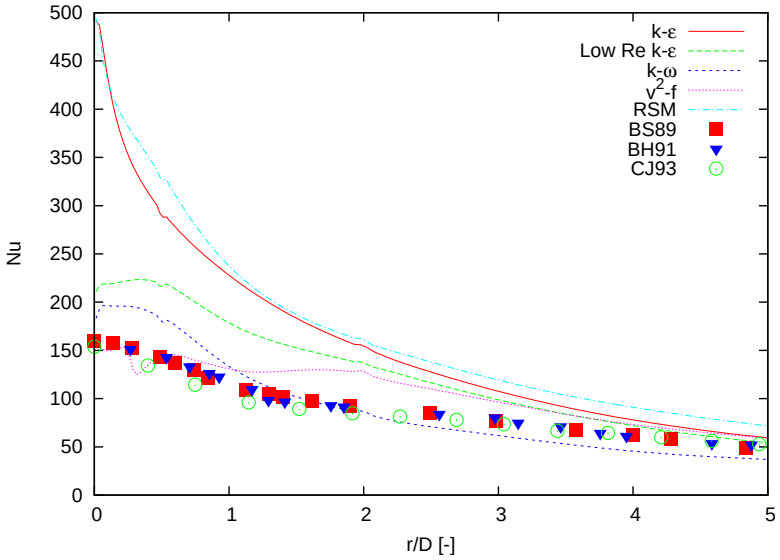

Figure 4.12: Surface Nusselt Number, z = 6, Re = 23000 (BS89 - Baughn and Shimizu [3], BH91 - Baughn et al. [4], CJ93 - Cooper et al. [5])

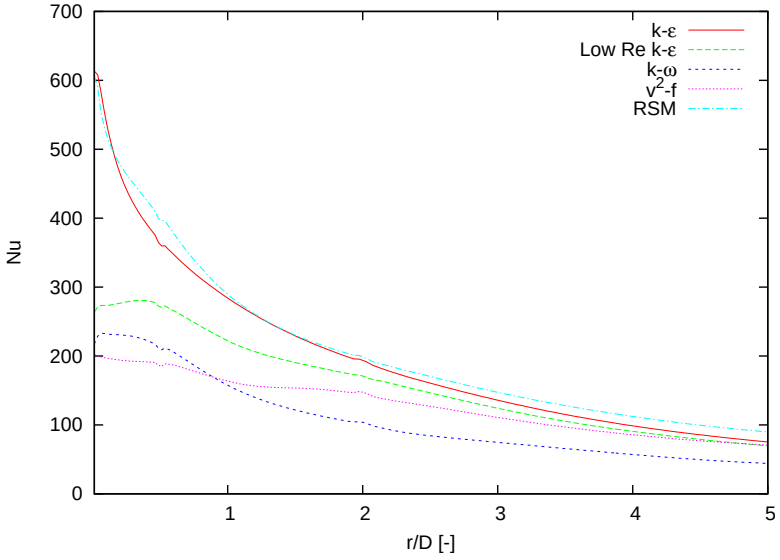

Figure 4.13: Surface Nusselt Number, z = 6, Re = 30000

Differences in the predicted surface Nusselt number are clearly apparent when comparing the results from each of the turbulence models. Generally, all models predicted a higher local Nusselt number for the heated surface than the experimental results, with the overprediction the greatest within a radial distance of two jet diameters from the jet axis. Beyond this distance from the axis the predicted Nusselt numbers begin to converge with the experimental results. Far from the jet axis, the k-ε, k-ω, RSM and $\overline{v}^2$-f models all predict higher a local Nusselt number, while the k-ω model underpredicts the Nusselt number in this region. Among the models investigated, the Reynolds Stress model and k-ε model exhibit the highest deviation from the experimental results. The remaining three models, the $\overline{v}^2$-f model, Low Re k-ε model and the k-ω model show reasonable agreement in all cases examined. This behaviour is explored in the next section.

4.5 Discussion

The worst performing model of those investigated was the standard k-ε turbulence model. Considering this model first, the standard k-ε model was developed fundamentally for simple flows, where shear is the predominant mechanism in the flow. Additionally, in the formulation tested this model requires a separate blending model or wall function approach to solve for the boundary layer flow. In jet impingement flows however, high streamline curvature occurs in the stagnation region, followed by steep velocity gradients and vigorous flow transitions within the wall-jet region and consequently the standard k-ε model does not adequately represent the entire flow domain, in part due to its dependence on a near-wall model.

This failure to accurately capture the stagnation region of impinging jet flow is best demonstrated by examining the contours of turbulent kinetic energy in this region. Figure 4.14(a) shows contours of kinetic energy for the k-ε model, with Figure 4.14(e) showing contours of turbulent kinetic energy from the $\overline{v}^2$-f model for comparison.

It is apparent from this figure that the turbulent kinetic energy in the stagnation re-

gion was predicted to be much greater for the standard k-ε model when compared with the results from the $\overline{v}^2$-f model. The higher kinetic energy predicted by the standard k-ε model accounts for the significantly higher predicted local Nusselt number. This mechanism has previously been identified by Craft et al. [6].

The Reynolds stress model, while developed to account for a larger range of flows, unfortunately also predicted the local Nusselt number poorly. As with the standard k-ε model the Reynolds stress model as included in FLUENT also relies on a separate near wall model to account for the boundary layer flow. As a consequence the RSM also predicts a higher local Nusselt number due to the near wall model overpredicting the generation of turbulent kinetic energy in the stagnation region. Figure 4.14(b) illustrates this with a much higher levels of turbulent kinetic energy visible compared to the $\overline{v}^2$-f model predictions shown in Figure 4.14(e).

The low-Reynolds number k-ε model, k-ω and $\overline{v}^2$-f turbulence models perform much better in predicting impinging jet flow and heat transfer for the flat heated surface test case. This is mostly as a result of better prediction of the turbulent kinetic energy production at the heated wall, with none of these models requiring a separate model to account for the boundary layer flow. Again plotting contours of the kinetic energy near the stagnation region is useful. Figures 4.14(c), 4.14(d) and 4.14(e) show contours of turbulent kinetic energy for the low-Reynolds number k-ε model, the k-ω model and the $\overline{v}^2$-f model respectively. In each of these cases low levels of turbulent kinetic energy are predicted for the region directly beneath the jet nozzle.

The low-Reynolds number k-ε model exhibited better agreement with the experimental results than the standard k-ε and RSM models, though significant kinetic energy production was still observed in the stagnation region. This was evident in the the heat transfer as well, with the local heat transfer predicted to be up to 75% greater than the corresponding experimental values. The low-Reynolds number k-ε model used in the investigation was based on the standard k-ε model and incorporated a 'damping function' to modify the turbulent parameters in the near wall region. While an alternative choice of the damping function may have improved model performance, this task was

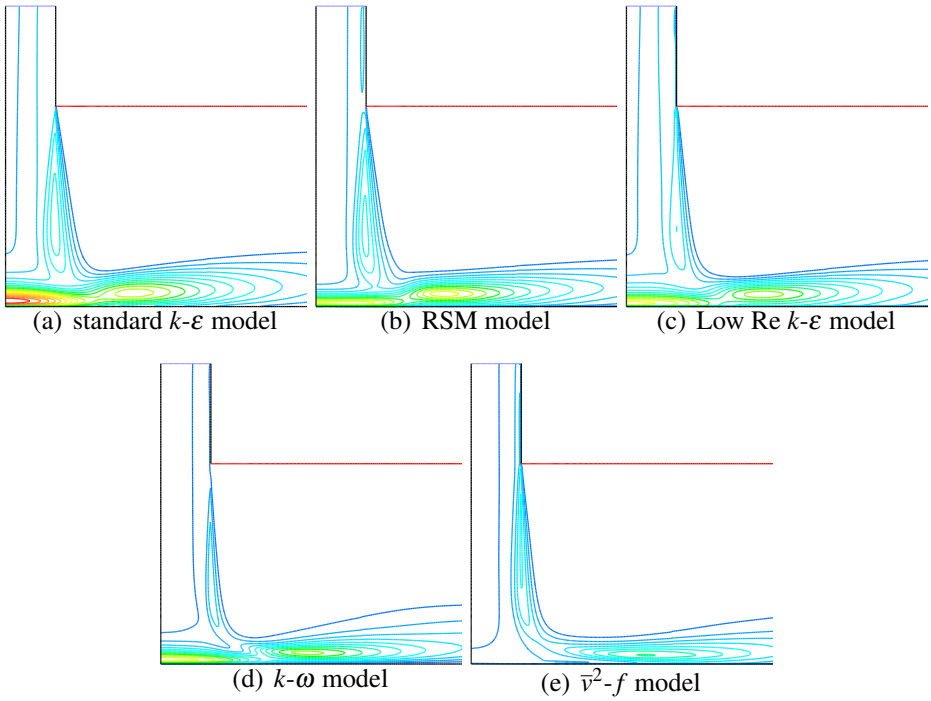

(a) standard k-ε model (b) RSM model (c) Low Re k-ε model

(d) k-ω model (e) $\overline{v}^2$-f model

Figure 4.14: Contours of turbulent kinetic energy normalised with respect to the maximum level for the k-ε model, Re $= 23,000$, $z^* = 2$

beyond the scope of this work.

The second of the contenders, the k-ω model, was like the k-ε model a two-equation model, though the formulation in terms of specific dissipation (ω) allowed easier modelling of near wall flows without the need for additional damping functions. In the results obtained the k-ω model also over-predicted the stagnation-point heat transfer by up to 40%. Away from the stagnation point, however, the heat transfer rate predicted was lower than the experimental values. The last of the candidate models, the $\overline{v}^2$-f model also used a damping function approach though the extent of the damping was determined by solving a separate relaxation equation over the whole flow domain in addition to solving a transport equation for the normal velocity fluctuations. As evident from Figures 4.2, 4.4, 4.6, 4.10 and 4.12, the $\overline{v}^2$-f model gives the least over-predicted heat transfer rates among all tested turbulent models. The results are in good agreement with experimental data for Reynolds numbers of 6500 and 23,000.

As observed in Figure 4.4 the $\overline{v}^2$-f model alone captures the secondary heat trans-

fer peak that occurs in jet impingement heat transfer at low jet-to-surface spacings ($z^* < 5$). The other turbulence models investigated failed to predict this feature, although a slight increase in local Nusselt number is observed in the results obtained with the Reynolds Stress and low-Reynolds number k-ε models, at locations corresponding to the secondary peak points. This secondary peak, evident in the experimental results, is an important characteristic of jet impingement heat transfer. While the local Nusselt number is lower in magnitude than the maximum value (which occurs in the stagnation region), when computing average heat transfer values for a circular jet the secondary peak makes a significant contribution to the total heat transfer due to the circumferential area increasing as the distance from the jet increases.

4.6 Conclusions

The work presented in this chapter was conducted to determine the most appropriate turbulence model for modelling jet impingement heat transfer. Due to the poor performance of the standard k-ε model and Reynolds Stress model, both were easily eliminated from the suitable turbulence models, while for the remaining models it was necessary to consider other factors as well. The low-Reynolds number-k-ε model and the k-ω model and $\overline{v}^2$-f models all gave reasonable predictions of the heat transfer, however the $\overline{v}^2$-f model was the only model which captured the secondary peak in heat transfer. This secondary peak is a characteristic feature of impinging jet heat transfer, and for this reason the $\overline{v}^2$-f model was selected for the remainder of the work presented in this thesis.

Chapter 5

Surface Protrusions

Much research has been done on new methods to enhance the heat transfer potential of impinging jet flows. Where the proposed techniques have concentrated on modifications to the target surface, the methods investigated have included ideas such as the effects of curvature or the effects of altering the surface roughness. The schemes proposed in this chapter and the following chapter are novel and show significant potential for enhancing heat transfer from an impinging jet. The first scheme, presented in this chapter, investigates the heat transfer characteristics of an impinging jet system incorporating a highly conducting protrusion, or 'cone', extending from the heat transfer surface.

5.1 Surface Modification Scheme

The surface modification scheme investigated in this chapter seeks to increase the heat transfer of an impinging jet by modifying the flow in the stagnation region of an impinging jet. This region contributes significantly to the heat transfer from the jet, and is a somewhat unique characteristic of impinging jet flows. As described in Chapter 1, the stagnation region of an impinging jet consists of a pocket of relatively stagnant fluid situated beneath the jet where the jet centreline intersects the target surface. This region has the highest local heat transfer rates observed in the system, even though the principal mode of heat transfer for a stagnant fluid is via conduction. The scheme described in this chapter replaces the stagnant fluid at the impingement point with solid material that has a higher thermal conductivity than the surrounding fluid. Figure 5.1 shows a general arrangement of the scheme. The protrusion aims to reduce disruption of the flow field near the stagnation region, and consequently, increase the net heat transfer rate from the surface.

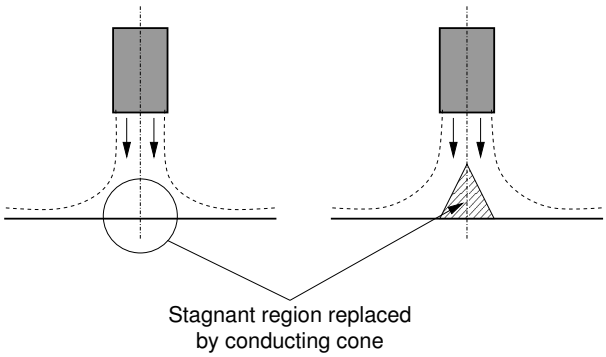

Figure 5.1: Proposed Surface Modification. Left: side view of an unmodified jet, Right: side view with an added conical protrusion

5.2 Methodology

To evaluate the proposed modification an appropriate measure of performance was required. The average surface Nusselt number, $\overline{\mathrm{Nu}}$, provides a good indication of the heat transfer performance, and for this investigation $\overline{\mathrm{Nu}}$ was defined as

$$\overline{\mathrm{Nu}} = \frac{4\dot{q}d}{\pi d_{\mathrm{ref}}^2 k_f \Delta T} \tag{5.1}$$

where $\dot{q}$ was the total heat transfer through a circular area of a diameter d_{ref} centred around the jet axis. The Nusselt number in Equation 5.1 is not a true Nusselt number, in the sense that the additional heat transfer area due to the cone was not accounted for and the material properties of the cone have been ignored. Even so, this parameter proved suitable as a means to compare the performance of each of the cone geometries.

5.3 Simulation Parameters

A parametric study was conducted to evaluate the performance of the proposed modification, after identifying the relevant variables. These variables were the cone aspect ratio, α, and the Reynolds number, Re. Additional parameters were also identified for investigation, though initial evaluation of the performance indicated that heat transfer enhancement was not as high as expected and that the 'cavity' proposal, described in

Chapter 6, provided better heat transfer enhancement potential. As a consequence only a single jet-to-surface distance, z, and cone diameter, d_c, were considered. The parameters for the study were non-dimensionalized with respect to the jet diameter and the range of values investigated are given in Table 5.1, while Figure 5.2 relates them to the geometry of the jet.

Parameter	Variable	Non-dimensionalized	Values
Jet-to-surface height	z/d	z^*	2
Cone Diameter	d_c/d	d_c^*	1
Cone Aspect Ratio	$2h/d_c$	α	0, 0.5, 1.0, 2.0
Jet Velocity	$\rho V d/\mu$	Re	200, 500, 1000, 2000, 5000, 10000, 20000, 30000

Table 5.1: Parameter Ranges for Cone Geometries. $\alpha = 0$ corresponds to the reference flat plate case.

Preliminary analysis of results showed separation of the flow where the base of the cone met the heated surface. To reduce this separation it was decided to investigate whether the addition of a fillet at the cone base provided any further change in the heat transfer compared with the original cases. The resulting set of surface cone geometries investigated is displayed in Table 5.2.

The problem was simplified for analysis by considering the problem to be two-dimensional and axisymmetric. A simple rectangular section of the geometry was modelled, with a portion of the jet nozzle added to the domain to capture any flow variations near the exit of the jet. All fluid regions in the domain were considered to be air, while copper was selected as the material for the cone due to its high thermal

aspect ratio	without fillet	with fillet
$\alpha = 0.5$	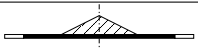	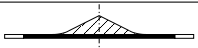
$\alpha = 1.0$		
$\alpha = 2.0$	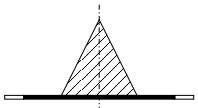	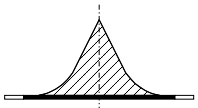

Table 5.2: Cone geometries investigated

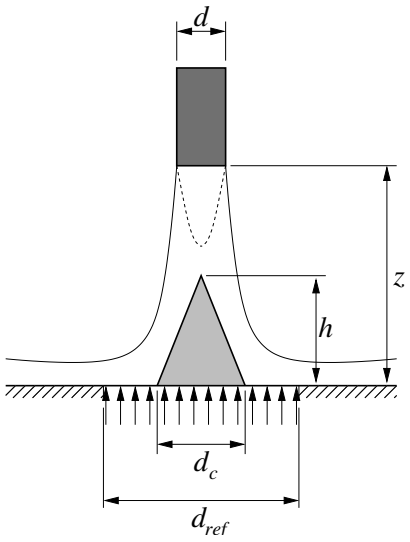

Figure 5.2: Solution Domain

conductivity of k = 387.6 W/mK. Turbulence was modelled using the $\overline{v}^2$-f model in accordance with the results from the turbulence modelling investigation presented in Chapter 4.

5.3.1 Boundary Conditions

The boundary conditions for the problem were as follows. The bottom surface was treated as an isothermal boundary at a temperature 25^{o}C higher than the jet temperature. The jet inlet velocity profile was taken to be uniform, with the bulk jet velocity, V, calculated to give the desired Reynolds numbers. A constant pressure boundary condition was used at the fluid outlets at the top and side of the domain, with the reference pressure set to zero.

5.3.2 Mesh

The domain was discretized using a quadrilateral mesh except for the solid region of the cone. This region was discretized using a triangular mesh to accurately capture the geometry. A finer grid spacing was used adjacent to all surfaces in the fluid region to allow accurate representation of the boundary layers. Grid independence checks

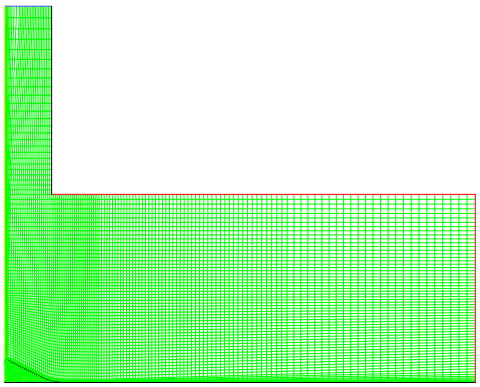

Figure 5.3: Typical mesh for a cone protruding from the surface

were conducted as outlined in Chapter 3. Figure 5.3 shows a typical mesh used for the simulations.

5.4 Results and Discussion

The equation to define the average surface Nusselt number, Equation 5.1, required a diameter, d_{ref}, to be determined in order to calculate the average heat transfer rate from the jet. This reference diameter was chosen to be two times the jet diameter, a distance that represents the most effective region for heat transfer in a typical impinging jet system. Figures 5.4 and 5.5 show the heat transfer, as indicated by the average surface Nusselt number, from each of the cone geometries studied. The figures refer to cones without and with fillets respectively. It can be seen from the figures that the introduction of the cone aids the heat transfer from the surface, especially for a cone aspect ratio, α, of 2.0. Better heat transfer is indicated where data points occur above the line marked reference, which indicates the heat transfer available from a flat plate.

This data is presented in an alternative format in Figure 5.6, which shows the ratio of the heat transfer of the modified surface to that of the flat plate reference case.

Presented in this way, it is clear whether heat transfer is improved or otherwise. For a cone with an aspect ratio of 2.0 heat transfer is significantly improved across the range of Reynolds numbers studied, whereas for an aspect ratio of 1.0 and no fillet, heat

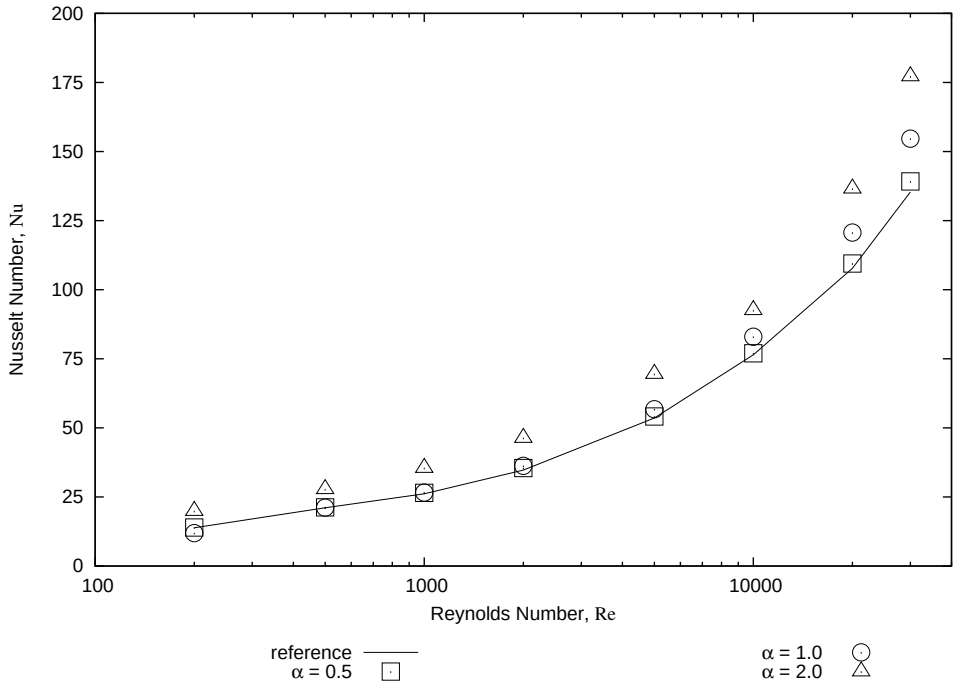

Figure 5.4: Surface heat transfer, without fillet

transfer enhancement is obvious at high Reynolds number. For all other cases, the effects of surface modification are minimal, with almost the same heat transfer recorded for surfaces with and without a cone. The following sections identify and discuss the observed trends in more detail as the aspect ratio and the Reynolds number were varied for cones with and without a fillet at the base.

5.4.1 Reynolds number

Figures 5.4 and 5.5 show that the effect of increasing the Reynolds number of the jet was to increase the heat transfer from the surface. This variation was consistent with expectations; a higher Reynolds number indicates increased mass flux, and hence more fluid is available to remove heat from the system. This increase in Nusselt number was observed for cases both with and without a base fillet.

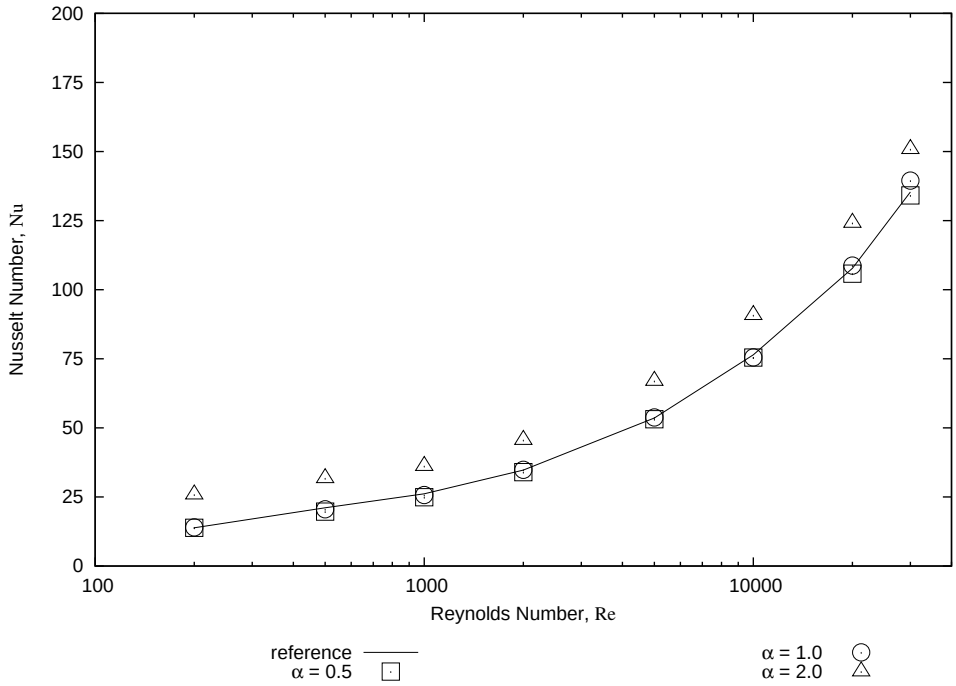

Figure 5.5: Surface heat transfer, with fillet

5.4.2 Cone Aspect Ratio

The aspect ratio of the cone, α, was observed to affect the surface averaged Nusselt number for the cone geometries investigated. The extent of this dependence was influenced by the jet Reynolds number, and whether or not the cone had a fillet at the base. At Reynolds numbers above 5000 and for all cases where there was no fillet, the calculated Nusselt number was found to increase as the aspect ratio of the cone increased. However, significant variation was observed in the magnitude of the increase in Nusselt number between cases. For the remainder of the Reynolds numbers investigated (5000 and below), at cone aspect ratios of 0.5 and 1.0 and for cases with no fillet, the calculated Nusselt number did not vary significantly from the flat plate reference case. In these cases both increases and decreases in Nusselt number were observed. For the cases with no fillet and with an aspect ratio of 2.0, increases in Nusselt number of around 30 to 40% were observed.

For the cases with a base fillet, for cones with aspect ratios of 0.5 and 1.0, no significant changes in Nusselt number were observed, with small increases or decreases

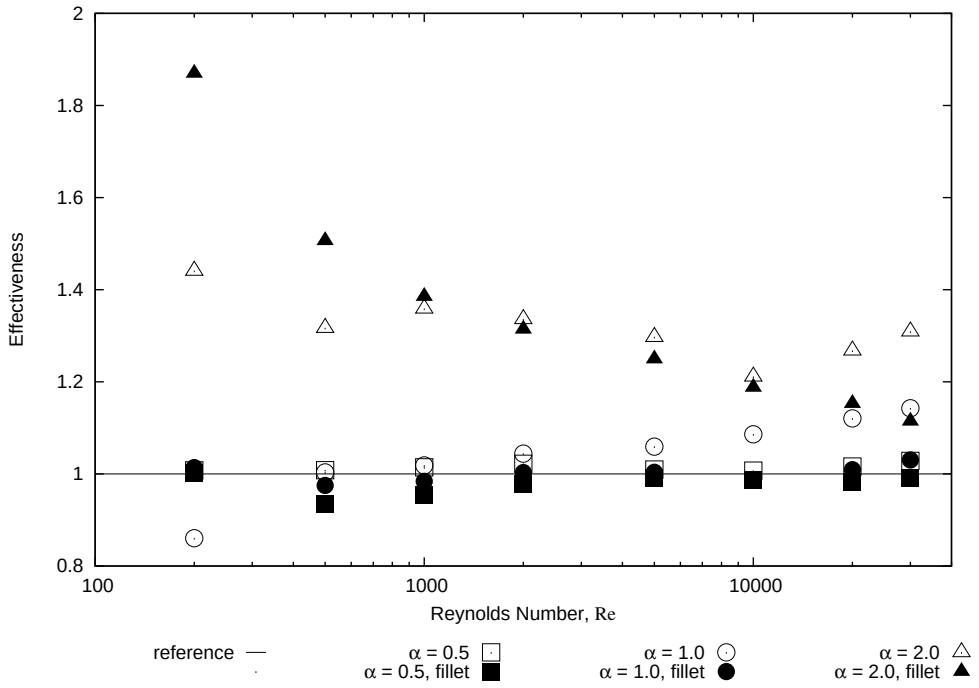

Figure 5.6: Ratio of heat transfer from modified surface to heat transfer from reference surface, for cases both with and without base fillets

observed across the complete range of Reynolds numbers. For cones with an aspect ratio of 2.0, increases in Nusselt number were observed at all Reynolds numbers, though the magnitude of the increase dropped off significantly as the Reynolds number increases. For Reynolds numbers above 2000 the observed increases were smaller than for the cases without a fillet.

5.4.3 Effect of Fillet

By comparing the calculated Nusselt number from the cases with and without a base fillet, it is possible to isolate the effects on heat transfer due to the fillet only. Figure 5.7 shows the ratio of the Nusselt number of a filleted cone to the same cone without the fillet. This figure clearly shows that in most cases the addition of a fillet has a detrimental effect on the heat transfer, with decreases between 1% and 15% observed. The exceptions to this were for Reynolds numbers of 1000 and below at an aspect ratio of 2.0, and at a Reynolds number of 200 at an aspect ratio of 1.0. In these 4 cases the

fillet increased the Nusselt number by between 2% and 30%.

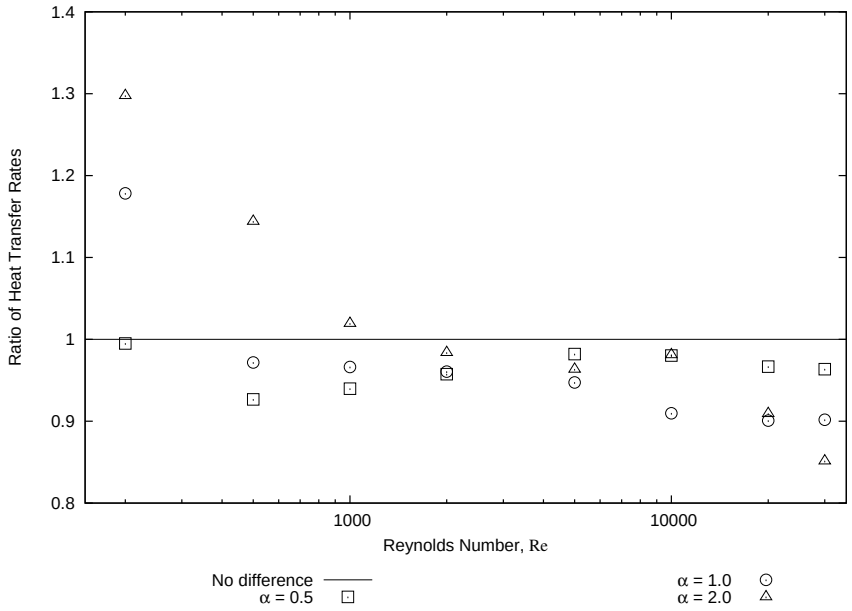

Figure 5.7: Ratio of Average Nusselt number for cones with and without base fillets

Figure 5.8 shows contours of stream function for a Reynolds number of 20,000. In this figure it can be seen that flow separation occurs when no base fillet is present for cone aspect ratios of 1.0 and 2.0. Addition of a fillet to the base of the cone eliminates the separation and the flow follows more closely the contours of the modified surface. Contrary to what may be expected, at this Reynolds number the addition of the fillet causes a reduction in the heat transfer from the surface. Figure 5.9 shows contours of turbulent kinetic energy near the base of the cone at a Reynolds number of 20,000. Examining this figure reveals that the introduction of the fillet causes a drop in the level of turbulence near the base. This naturally results in a reduction in the heat transfer in this region.

Figure 5.10 also shows contours of turbulent kinetic energy near the base of the cone, this time at a Reynolds number of 200. At this lower Reynolds number it is evident that there is minimal turbulence in the region of the fillet, and therefore no reduction in the heat transfer rate.

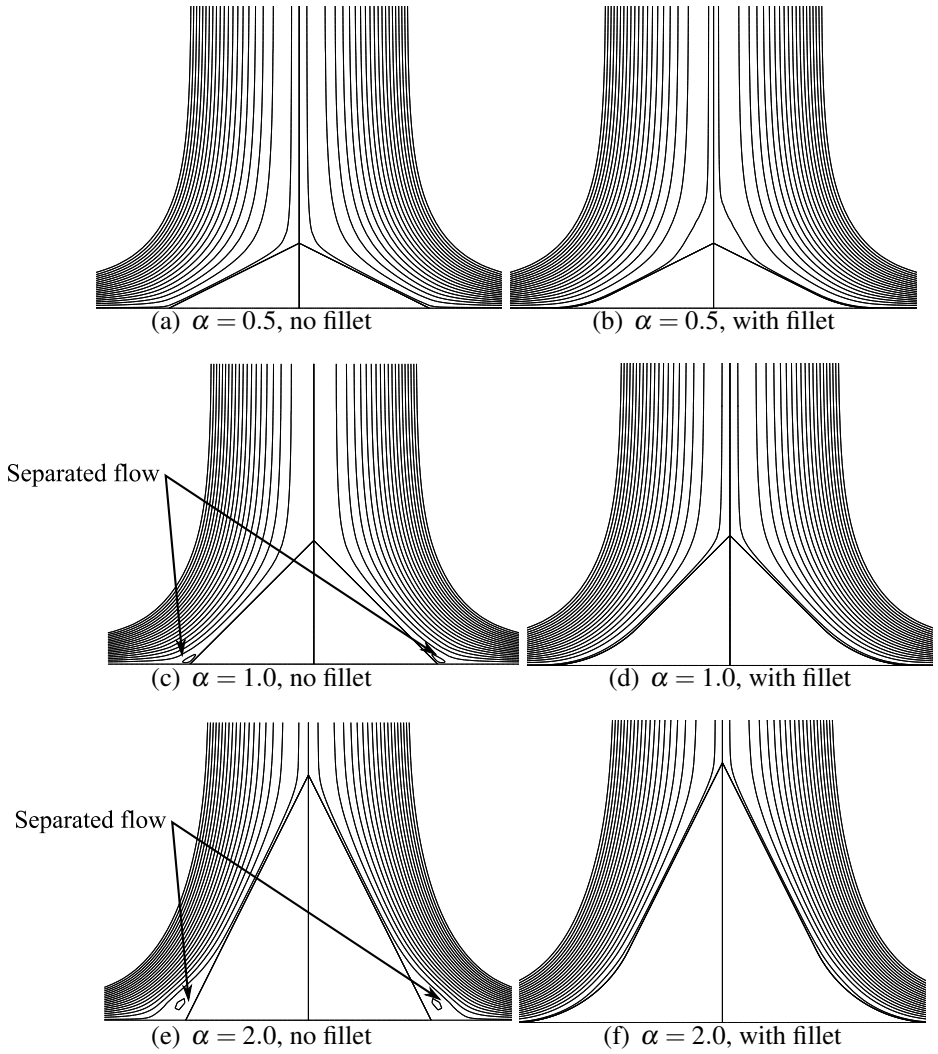

Figure 5.8: Flow contours near cone surface, showing flow separation in cases without a base fillet (Re=20,000)

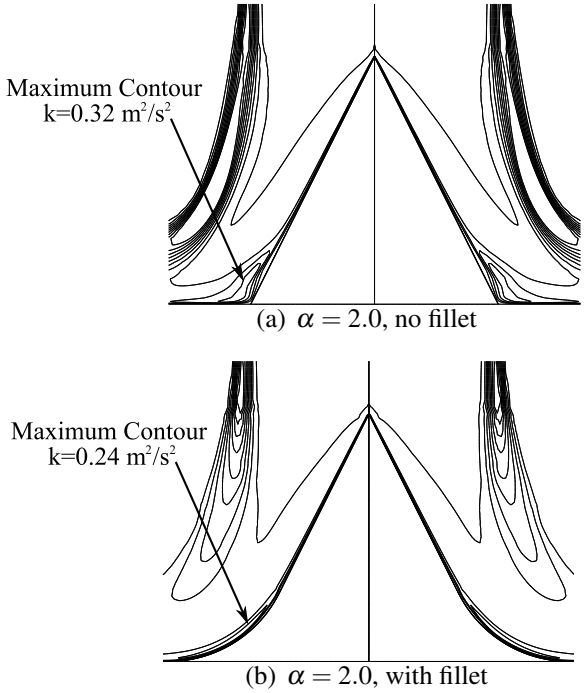

Figure 5.9: Contours of Turbulent Kinetic Energy, Re=20,000

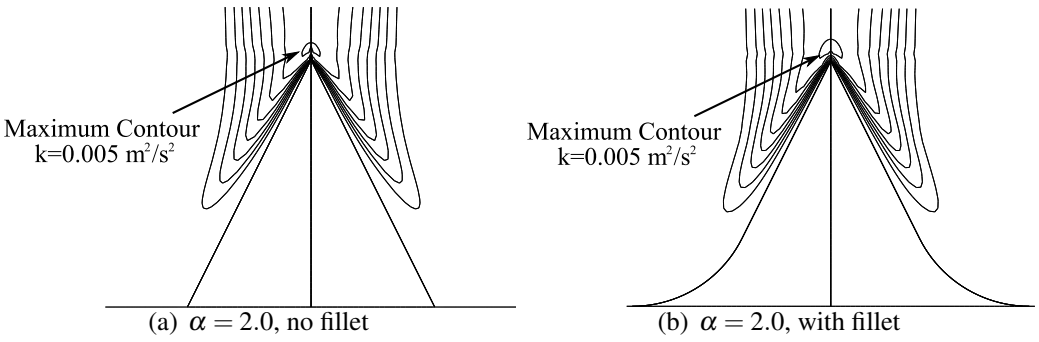

Figure 5.10: Contours of Turbulent Kinetic Energy, Re=200

5.5 Conclusions

In this chapter the potential for heat transfer enhancement by the addition of a protruding object directly beneath an impinging jet was investigated. Conical protrusions with high thermal conductivity located on the target surface and in-line with the jet axis were investigated. Large variations in the effects of these protrusions were evident from the results when compared with a flat-plate reference case. In the worst cases, heat transfer was reduced by up to 13%, while for favourable cases, heat transfer was significantly improved, with almost double the heat transfer observed in some cases. Examination of the flow in the affected region indicated that some flow separation occurred at the cone base for some configurations. At high Reynolds numbers, contrary to what may be expected, enhanced heat transfer was observed in the region and was due to the promotion of local turbulence. This was borne out for low Reynolds number cases where including a fillet at the base improved heat transfer, as turbulence levels near the base were low and had minimal affect on heat transfer. The high dependence of the heat transfer on the geometry of the cone suggests that further enhancement could be possible by careful selection of the surface profile based on the expected Reynolds number for an application. Due to the necessary fine-tuning of this method of heat transfer enhancement, and the possibility of reducing the heat transfer compared with an unaltered surface, the effects of jet-to-surface distance and cone diameter were not investigated further. Instead, the proposal discussed in the next chapter suggested higher potential for heat transfer improvement.

Chapter 6

Surface Cavities

Chapter 5 examined the potential for enhancing heat transfer from an impinging jet by modifying the target surface by adding conical protrusions directly beneath the jet. This chapter investigates an alternative scheme to increase heat transfer from an impinging jet, also by modifying the target surface. In this case the surface is modified by including a cylindrical cavity directly beneath the impinging jet. An extensive literature review found no similar modification schemes and the work presented in this chapter provides a significant contribution to the field.

6.1 Surface Modification Scheme

The theme developed throughout this thesis, is that the stagnation region of an impinging jet provides somewhat unique flow characteristics, and altering this flow may greatly increase the possible heat transfer. In the previous chapter, the surface modification aimed to increase the heat transfer by replacing fluid in the stagnation region with a highly conducting solid protrusion. The scheme presented in this chapter also alters the flow in the stagnation region, although in this case by inducing an additional change in direction of the fluid.

As discussed in previous chapters, the flow from a jet impinging orthogonally on a surface goes though a 90 degree change in direction, starting parallel to the jet axis and finishing as a radial flow away from the jet and along the target surface. This abrupt change in momentum is a contributing factor for the inherently high heat transfer rates which are possible in an impinging jet system. The cavity modification presented here extends from this idea, which suggests that additional sharp changes in direction of the flow should further increase the heat transfer potential of an impinging jet system. In an axisymmetric jet the simplest means to induce the desired change in direction is to

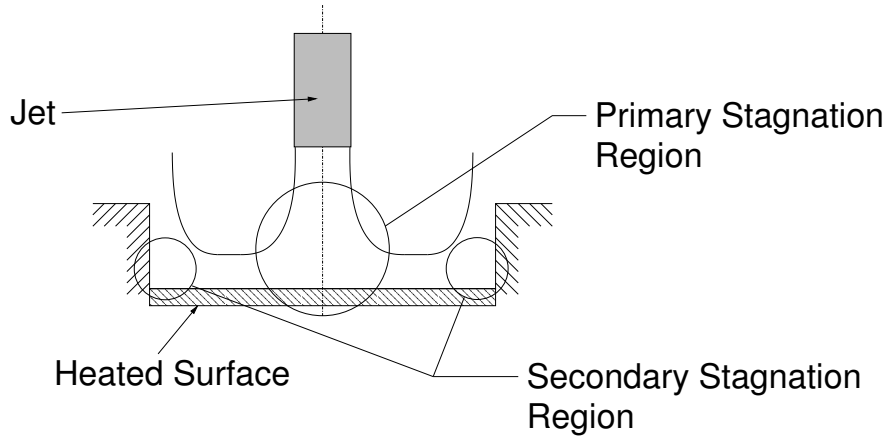

Figure 6.1: Cylindrical cavity introduced beneath an axisymmetric impinging jet

modify the surface by including a cylindrical cavity directly beneath the jet. This modification introduces a further 90 degree change in direction of the fluid, as illustrated in Figure 6.1.

6.2 Methodology

The previous chapter used the ratio of the heat transfer rates between the modified surface and unmodified surface to determine whether a protrusion added to the surface increased the heat transfer. Likewise, the surface cavity scheme also requires an appropriate method to determine if introducing surface cavities provides an increase in the heat transfer rate compared to a flat surface. The useful heat transfer from a cavity can be determined by calculating the average surface Nusselt number over the heat transfer area, denoted here as $\overline{\mathrm{Nu}}$, and defined as

$$\overline{\mathrm{Nu}} = \frac{4\dot{q}d}{\pi d_c^2 k_f \Delta T} \tag{6.1}$$

where $\dot{q}$ is the heat transfer rate from the cavity. In this work only the base of the cavity was used to calculate the average surface Nusselt number in order to isolate the effect on heat transfer due to the cavity alone. If the cavity walls had been included an

inherently higher value for heat transfer would have been observed due to the larger area available for heat transfer. To investigate the potential for heat transfer enhancement, the fluid flow and heat transfer for a number of different cavity geometries were predicted by numerical simulation and the average surface Nusselt number calculated and compared.

6.3 Simulation Parameters

In a similar manner to the previous chapter suitable parameters were identified for investigation prior to conducting the numerical simulations. The parameters deemed most likely to affect the heat transfer were identified as the jet to reference surface height, z, the cavity depth, l, the cavity diameter, d_c, and the jet velocity, V. Each of the geometric parameters were non-dimensionalized with respect to the diameter of the jet, with a Reynolds number used to indicate the jet velocity, based on the properties of air. Figure 6.2 identifies each of the parameters in relation to a diagram of the cavity geometry. The ranges for each of the parameters used for the simulations are shown in Table 6.1. Parameter combinations that were physically impossible were not simulated, namely those where the jet extended below the reference surface more than the depth of the cavity.

Parameter	Variable	Non-dimensionalized	Values
Jet-to-surface height	z/d	z^*	-2, -1, 0 , 1, 2
Cavity Depth	l/d	l^*	0, 1, 2, 3, 4
Cavity Diameter	d_c/d	d_c^*	2, 3, 4
Jet Velocity	$\rho V d/\mu$	Re	10000, 20000, 30000

Table 6.1: Parameter Ranges for Cavity Geometries

As for the studies in the previous chapters, simplification was possible due to rotational symmetry and axisymmetric models were used to reduce simulation complexity and solution time. The primary computational domain was two jet-diameters high and extended radially six jet-diameters from the jet axis, with the mesh extended as required to account for the fluid in the cavities. An additional portion of the jet nozzle

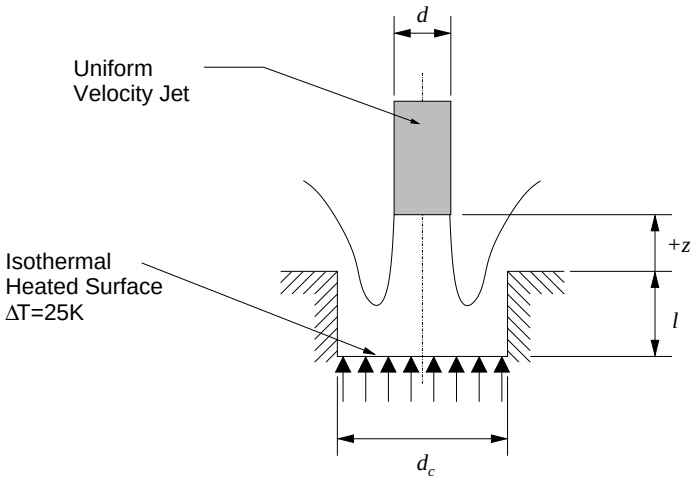

Figure 6.2: Simulation Parameters

was included to capture any flow variations near the exit. Fluid regions in the domain were considered to be air with properties taken as being independent of changes in temperature. The $\overline{v}^2$-f model was again used to account for the turbulence in the flow, based on the discussion presented in Chapter 4.

6.3.1 Boundary Conditions

The boundary conditions for the simulations were selected consistent with the aim of identifying any enhancement in heat transfer due to the cavities; adiabatic boundary conditions were applied to cavity walls and the reference surface, and constant pressure boundary conditions were applied to the top and sides of the domain with the reference pressure set to zero at the boundary. For the base of the cavity, an isothermal boundary was applied and the surface temperature was set to be 25^oC higher than the jet temperature. For the jet inlet the velocity was considered uniform across the diameter of the jet, while all wall boundaries had no-slip conditions applied.

6.3.2 Mesh

A regular rectangular grid was constructed throughout the domain and successively refined until the solution was independent of the grid size. In addition, local refinement

near the cavity walls was carried out until wall y^+ values were within the required limits, namely that $y^+ < 1$ for the $\overline{v}^2$-f turbulence model (as discussed in Chapter 3). Figure 6.3 shows a typical mesh used for simulation.

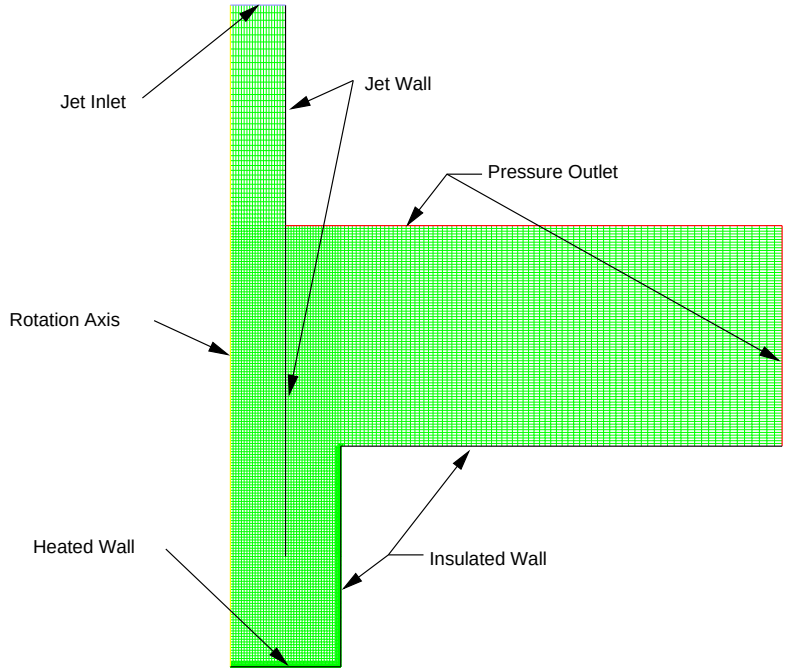

Figure 6.3: Typical grid independent mesh for a cavity geometry. (Depicted is z^*= -1, l^* = 2 d_c^* = 2)

6.4 Results and Discussion

Figures 6.4 to 6.12 show plots of the average surface Nusselt number over the cavity base for each of the investigated cavity geometries. A new variable, the dimensionless net cavity depth, L^*, is used for the abscissa. This is defined as the total distance between the nozzle exit and the base of the cavity, non-dimensionalized by the jet diameter, such that

$$L^* = z^* + l^* \tag{6.2}$$

The net cavity depth is introduced as it correlates better with the underlying characteristics of the flow than either the jet-to-surface distance or cavity depth alone. This

point is discussed in more depth in Section 6.4.1.

Additionally, preliminary analysis of the results suggested that it was appropriate to separate the results into two distinct groups for discussion, with the jet-to-surface distance, z^*, the determining factor. The first group included geometries where the jet nozzle discharged in-line with or below the level of the reference surface, $z^* \leq 0$, while the second group consisted of the remaining geometries, wherein the jet nozzle discharged above the reference surface level, $z^* > 0$.

The following sections identify and discuss the observed trends in the results as each of the net cavity depth, Reynolds number, and cavity diameter were varied.

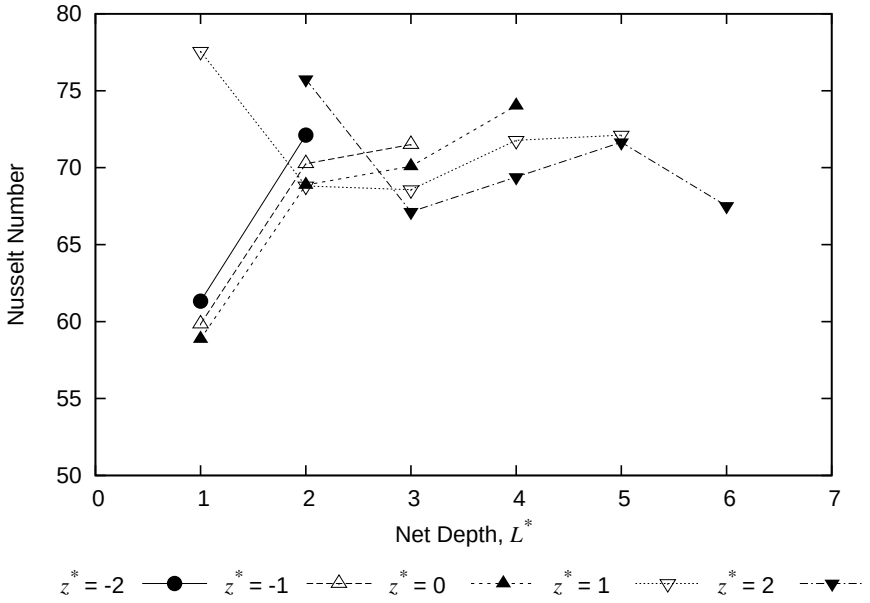

Figure 6.4: Average Surface Nusselt number, d_c^* = 2, Re = 10,000

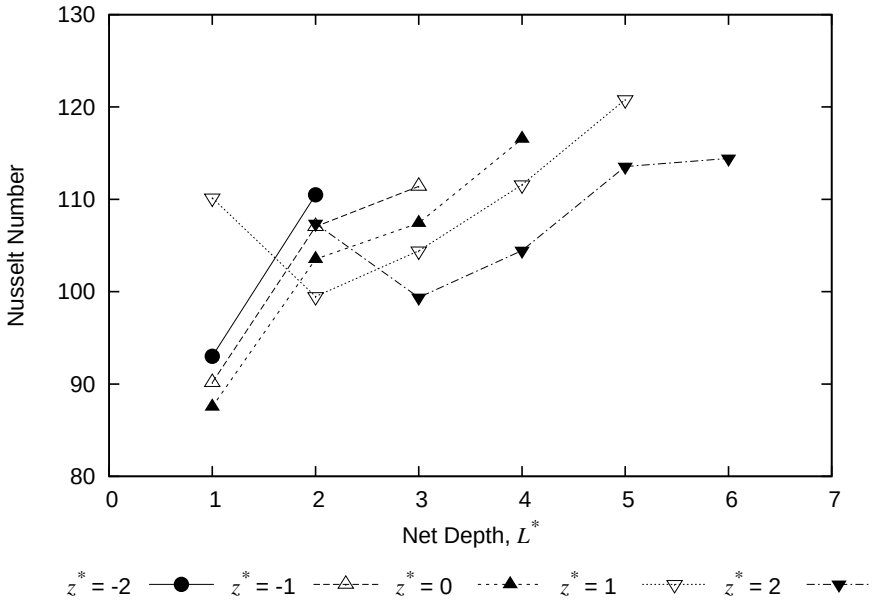

Figure 6.5: Average Surface Nusselt number, d_c^* = 2, Re = 20,000

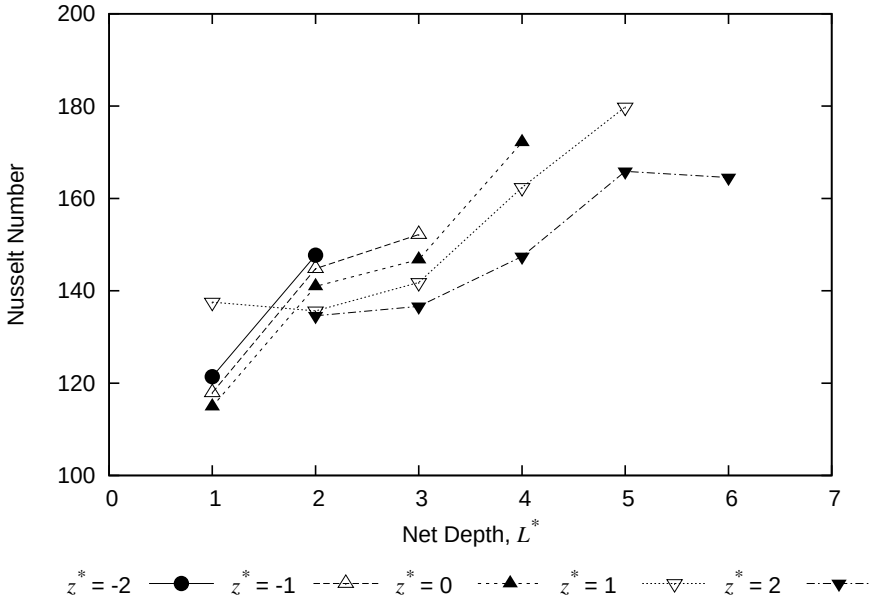

Figure 6.6: Average Surface Nusselt number, d_c^* = 2, Re = 30,000

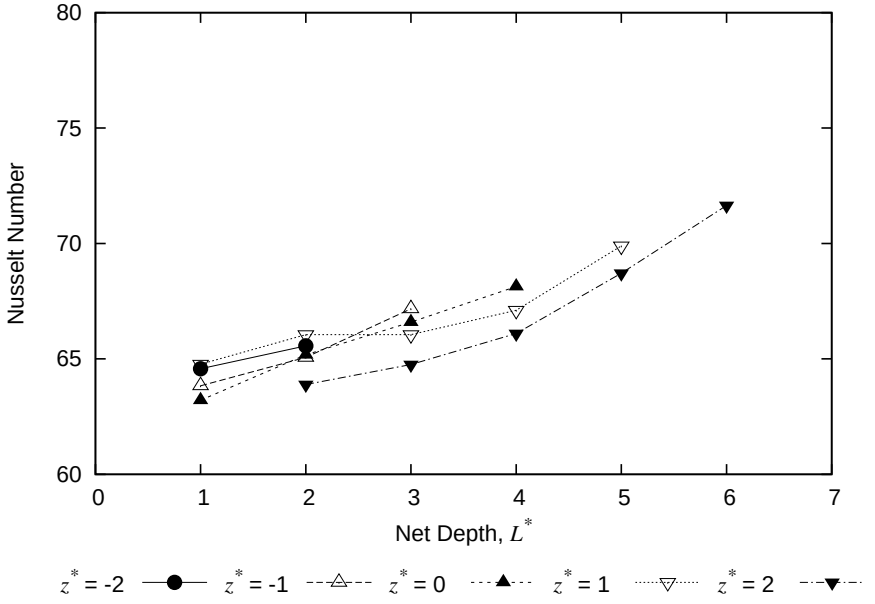

Figure 6.7: Average Surface Nusselt number, d_c^* = 3, Re = 10,000

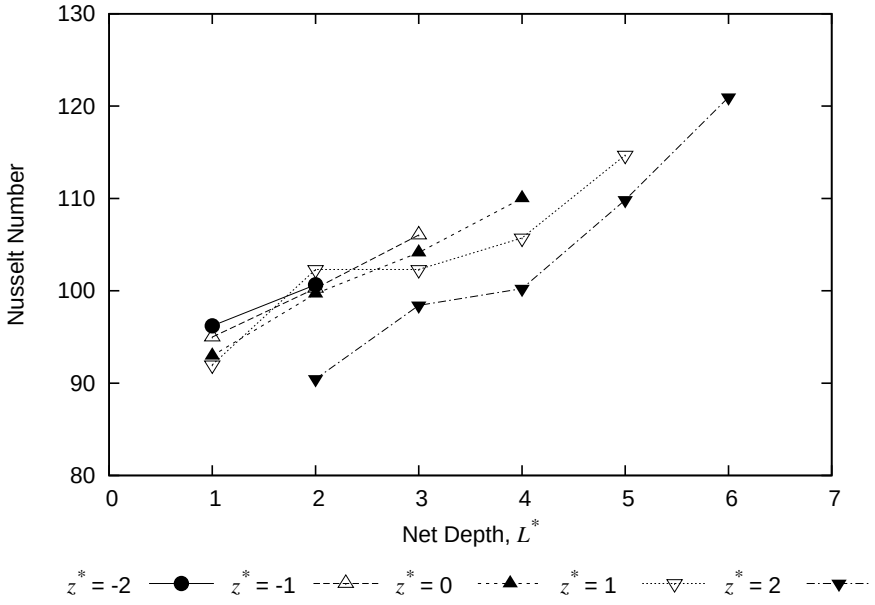

Figure 6.8: Average Surface Nusselt number, d_c^* = 3, Re = 20,000

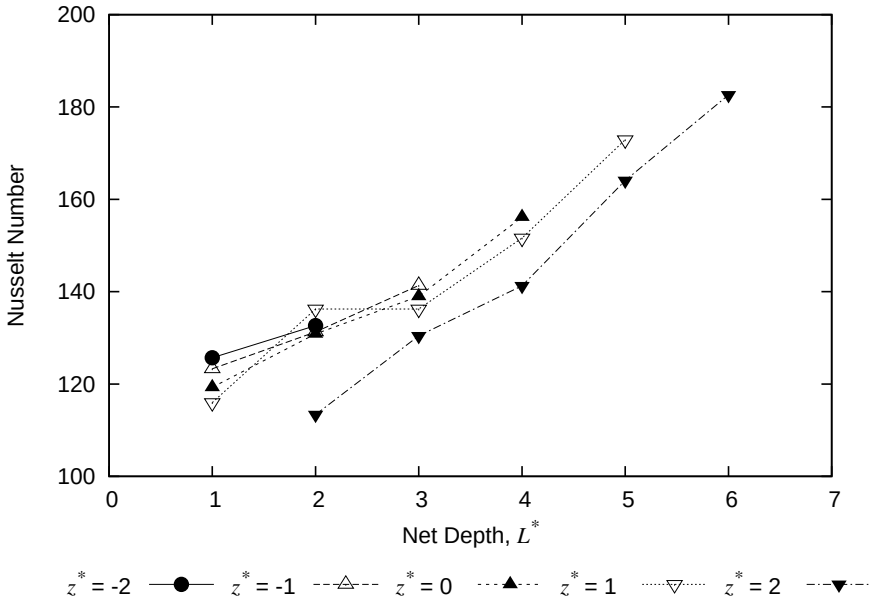

Figure 6.9: Average Surface Nusselt number, d_c^* = 3, Re = 30,000

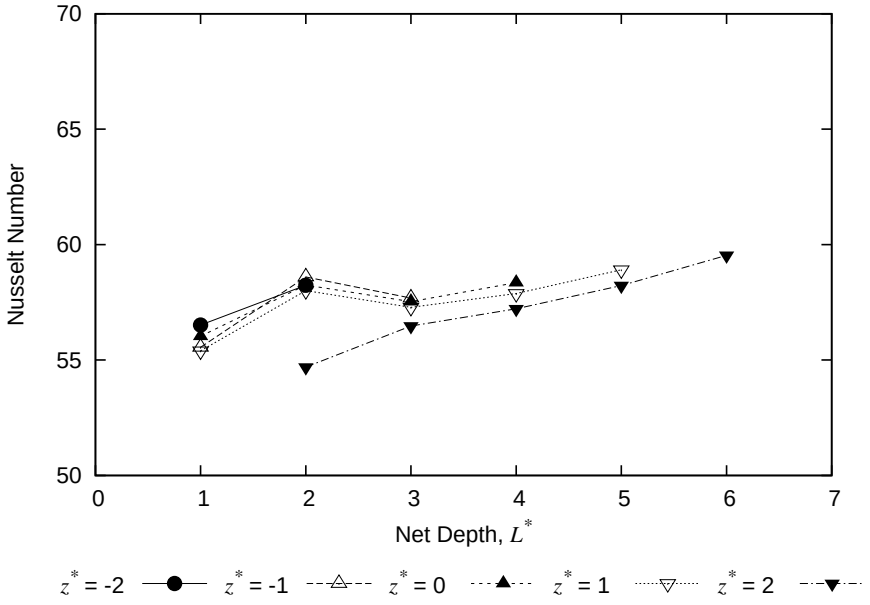

Figure 6.10: Average Surface Nusselt number, d_c^* = 4, Re = 10,000

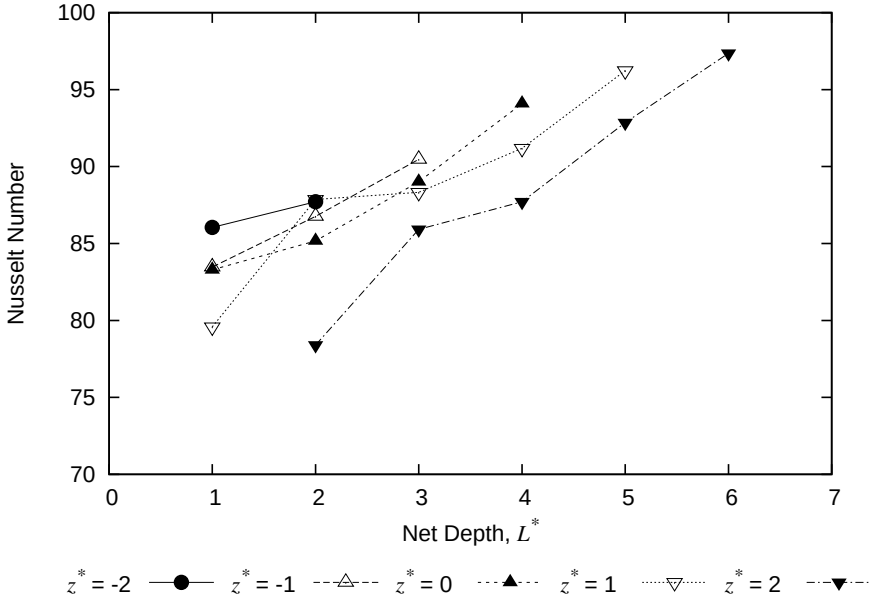

Figure 6.11: Average Surface Nusselt number, d_c^* = 4, Re = 20,000

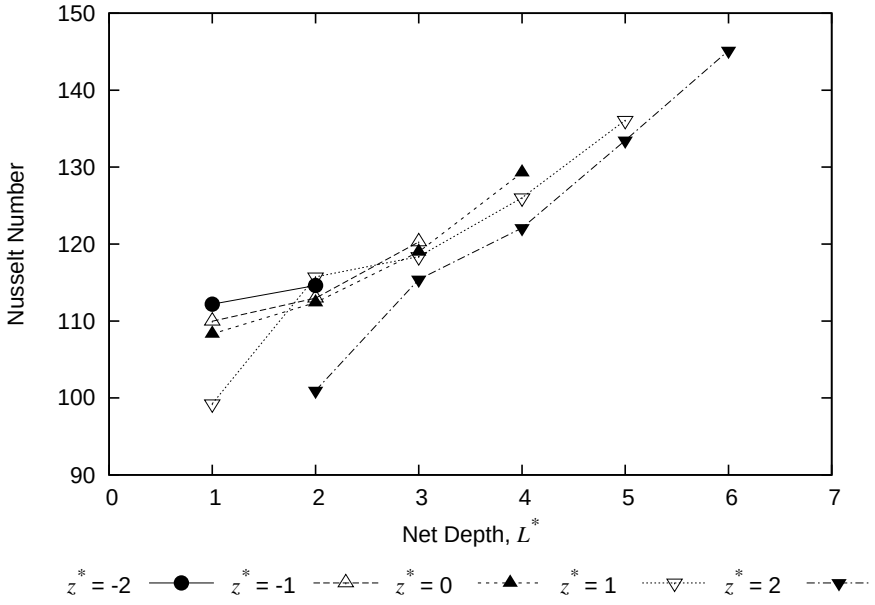

Figure 6.12: Average Surface Nusselt number, d_c^* = 4, Re = 30,000

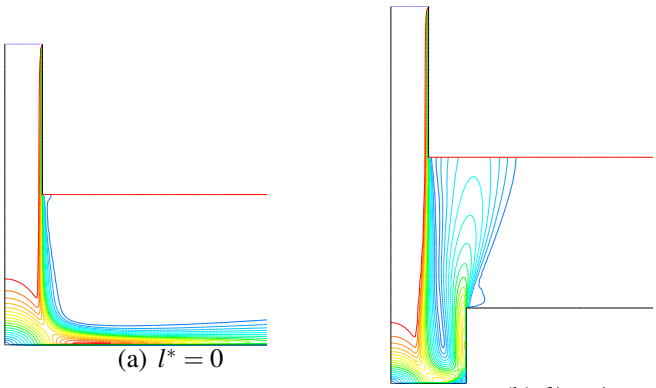

(a) $l^* = 0$

(b) $l^* = 1$

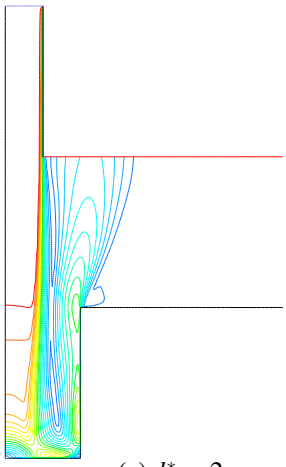

(c) $l^* = 2$

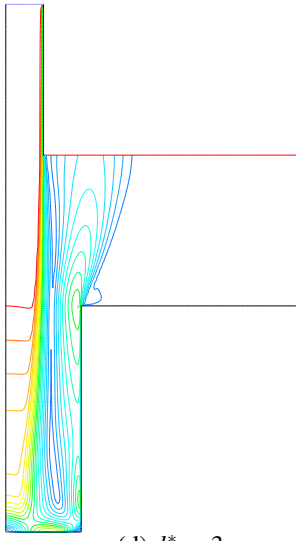

(d) $l^* = 3$

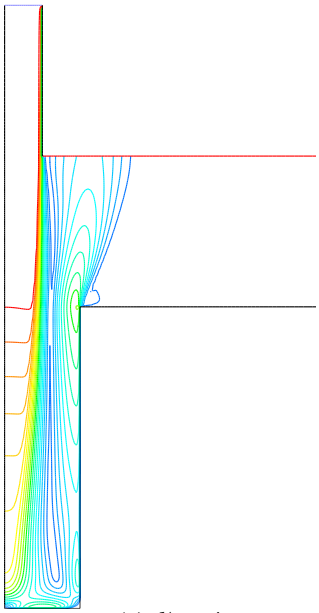

(e) $l^* = 4$

Figure 6.13: Velocity Contours, z^* = 2, d_c^* = 2, Re = 20,000

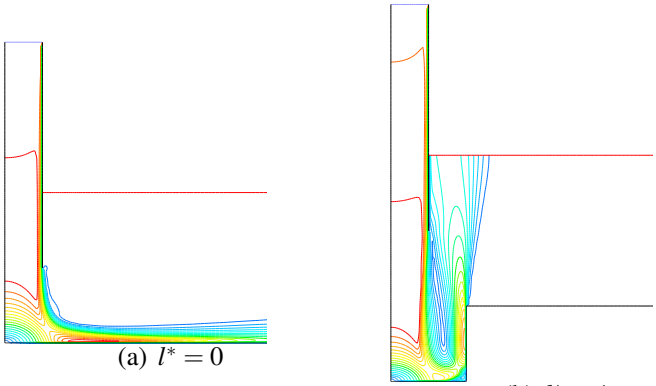

(a) $l^* = 0$

(b) $l^* = 1$

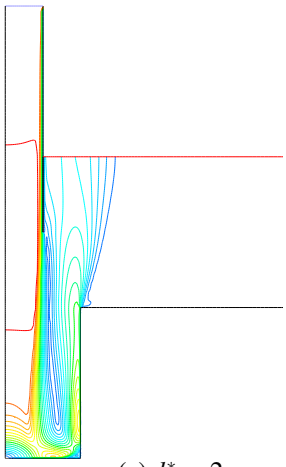

(c) $l^* = 2$

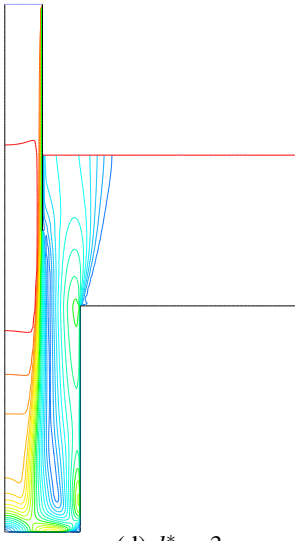

(d) $l^* = 3$

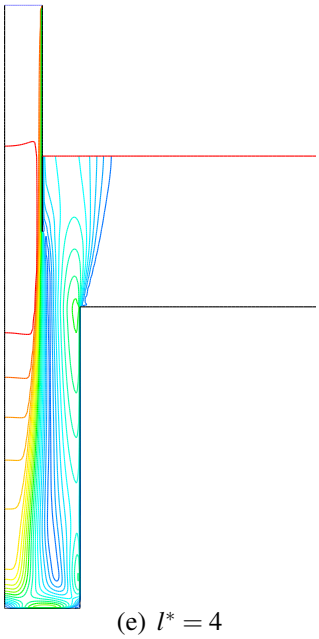

(e) $l^* = 4$

Figure 6.14: Velocity Contours, z^* = 1, d_c^* = 2, Re = 20,000

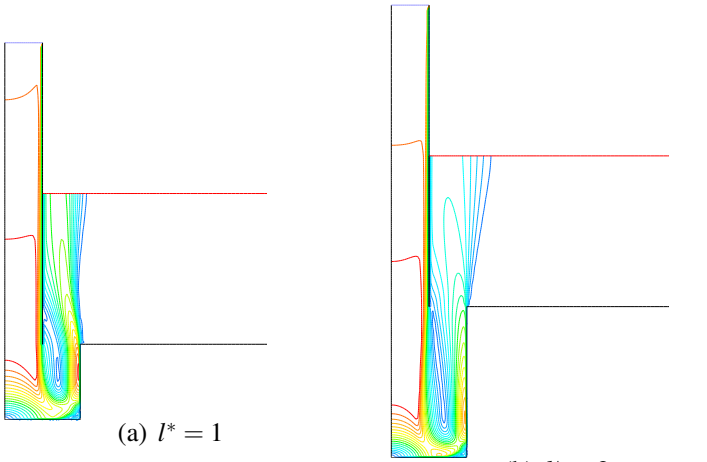

(a) $l^* = 1$ (b) $l^* = 2$

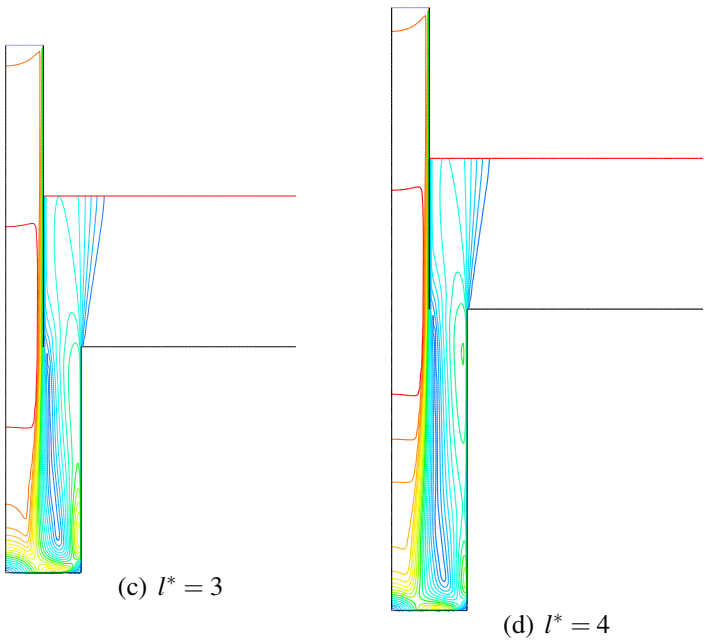

(c) $l^* = 3$ (d) $l^* = 4$

Figure 6.15: Velocity Contours, z^* = 0, d_c^* = 2, Re = 20,000

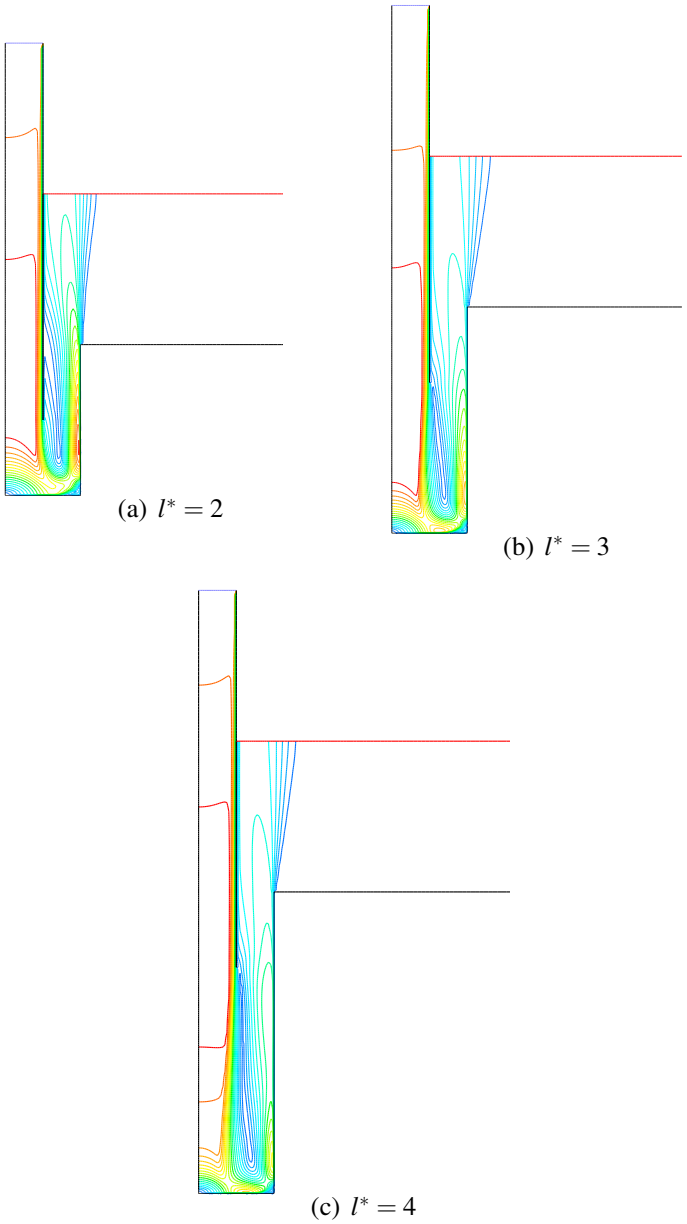

(a) $l^* = 2$

(b) $l^* = 3$

(c) $l^* = 4$

Figure 6.16: Velocity Contours, z^* = -1, d_c^* = 2, Re = 20,000

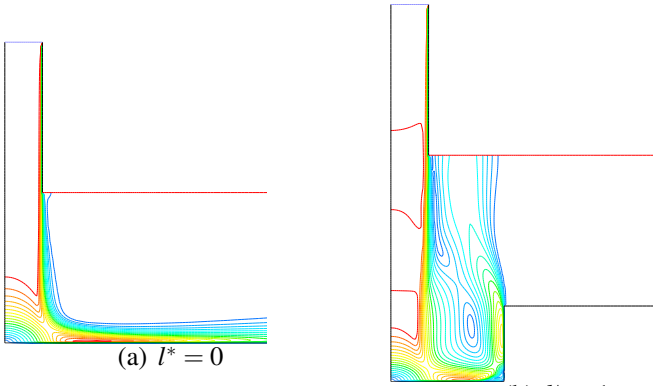

(a) $l^* = 0$

(b) $l^* = 1$

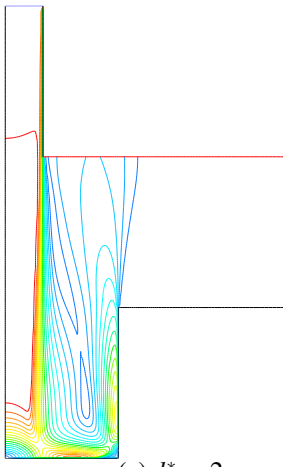

(c) $l^* = 2$

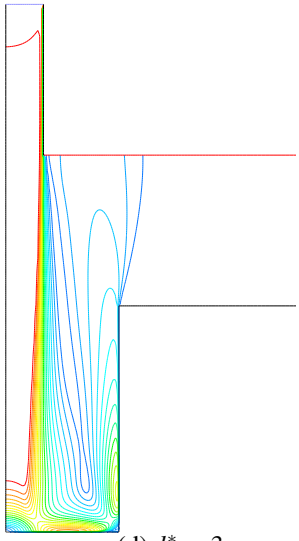

(d) $l^* = 3$

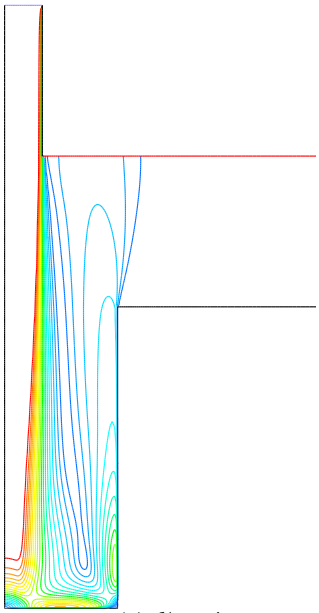

(e) $l^* = 4$

Figure 6.17: Velocity Contours, z^* = 2, d_c^* = 3, Re = 20,000

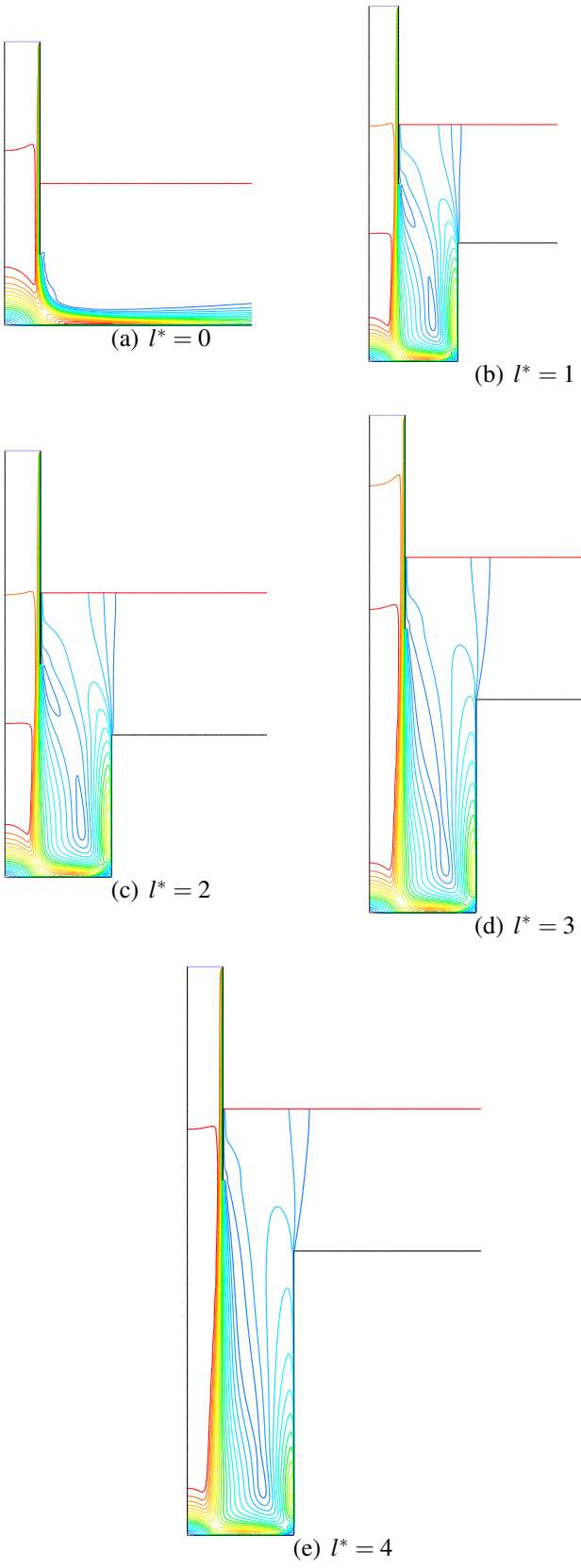

(a) $l^* = 0$

(b) $l^* = 1$

(c) $l^* = 2$

(d) $l^* = 3$

(e) $l^* = 4$

Figure 6.18: Velocity Contours, z^* = 1, d_c^* = 3, Re = 20,000

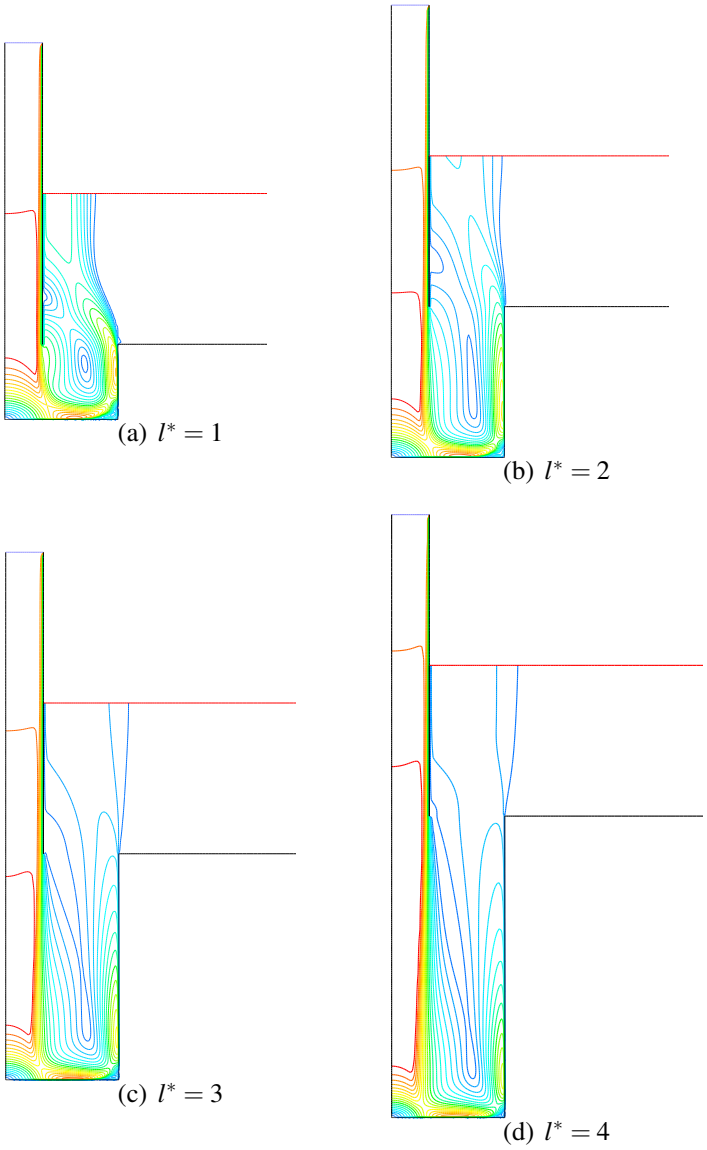

(a) $l^* = 1$ (b) $l^* = 2$

(c) $l^* = 3$ (d) $l^* = 4$

Figure 6.19: Velocity Contours, z^* = 0, d_c^* = 3, Re = 20,000

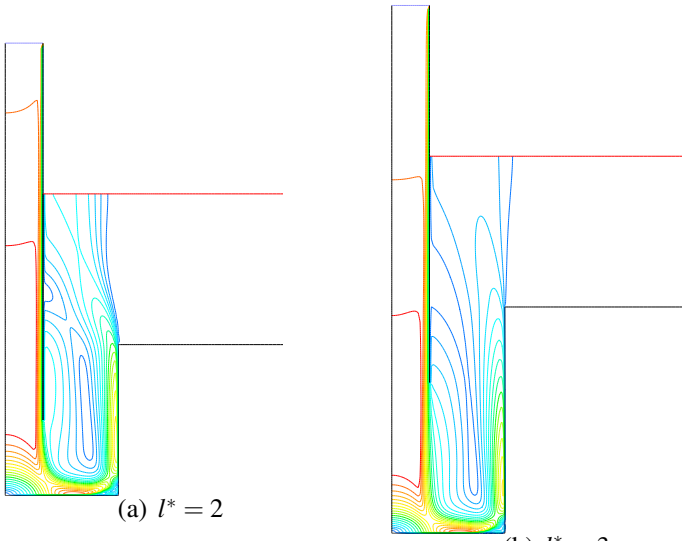

(a) $l^* = 2$ (b) $l^* = 3$

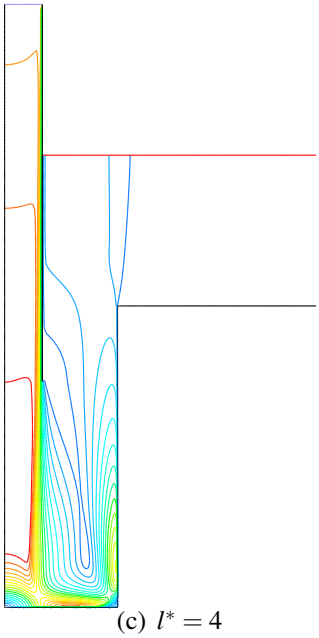

(c) $l^* = 4$

Figure 6.20: Velocity Contours, z^* = -1, d_c^* = 3, Re = 20,000

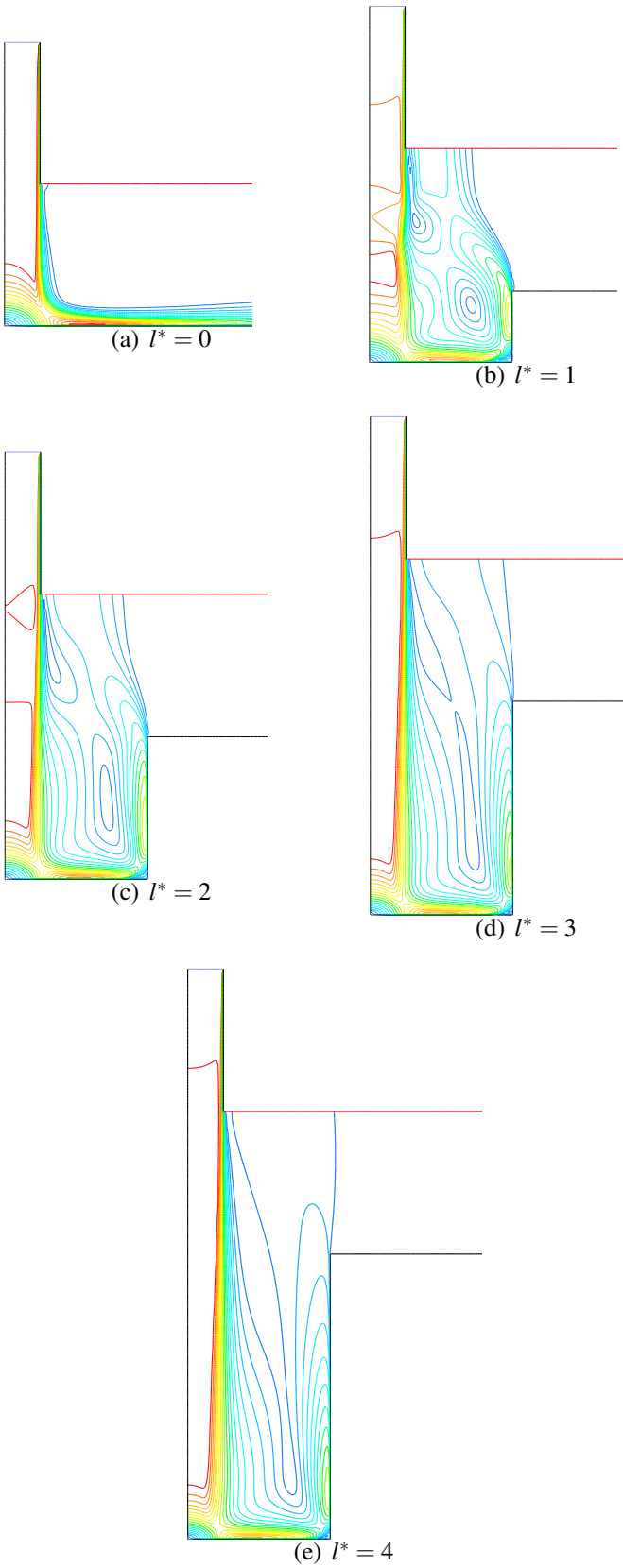

(a) $l^* = 0$

(b) $l^* = 1$

(c) $l^* = 2$

(d) $l^* = 3$

(e) $l^* = 4$

Figure 6.21: Velocity Contours, z^* = 2, d_c^* = 4, Re = 20,000

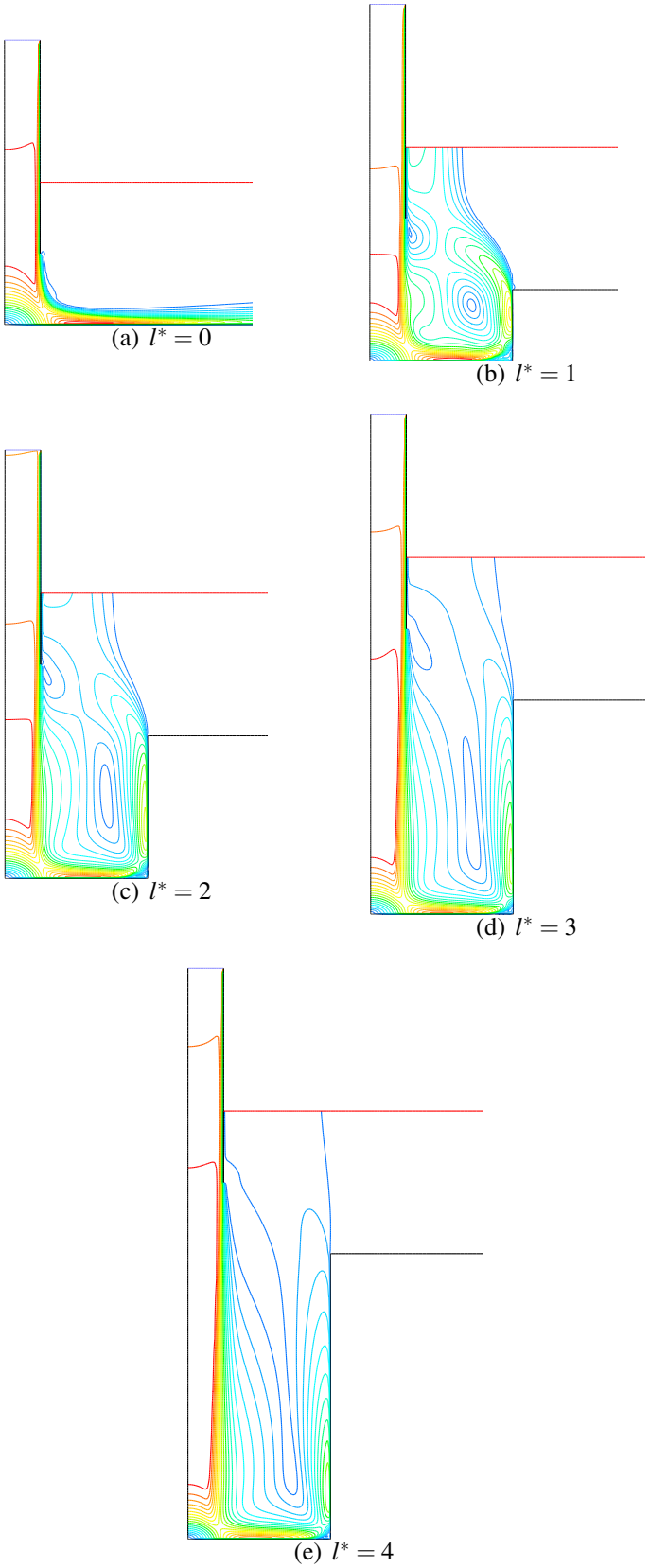

(a) $l^* = 0$

(b) $l^* = 1$

(c) $l^* = 2$

(d) $l^* = 3$

(e) $l^* = 4$

Figure 6.22: Velocity Contours, z^* = 1, d_c^* = 4, Re = 20,000

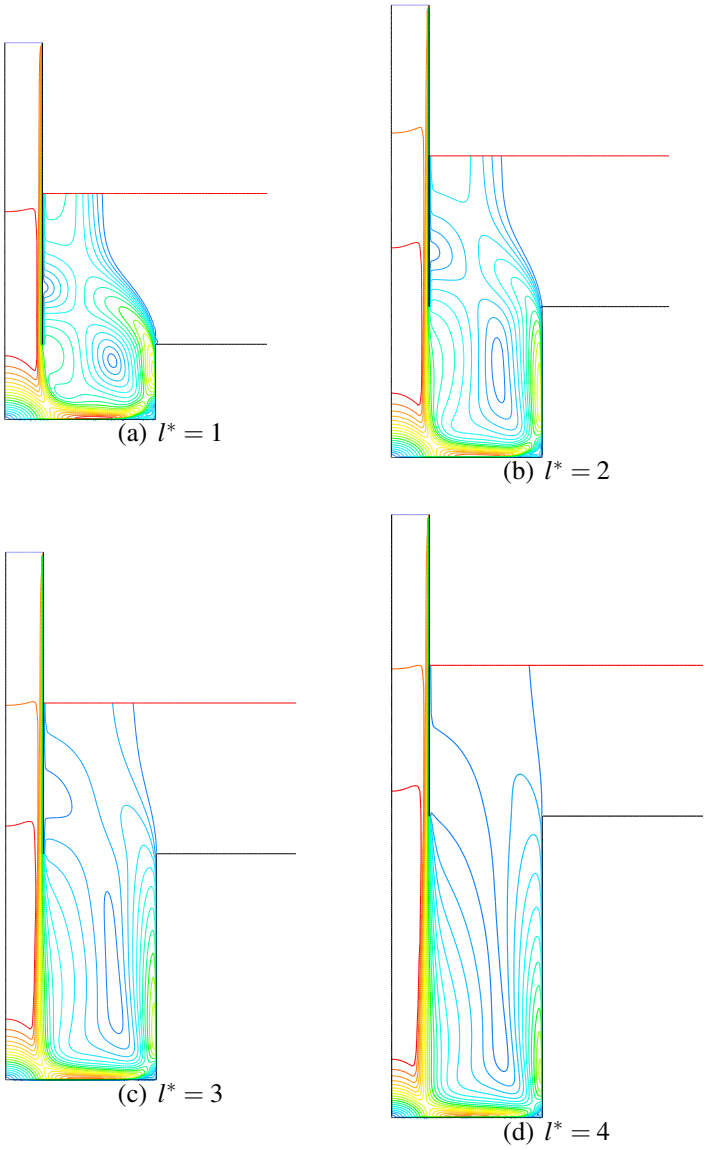

(a) $l^* = 1$ (b) $l^* = 2$

(c) $l^* = 3$ (d) $l^* = 4$

Figure 6.23: Velocity Contours, z^* = 0, d_c^* = 4, Re = 20,000

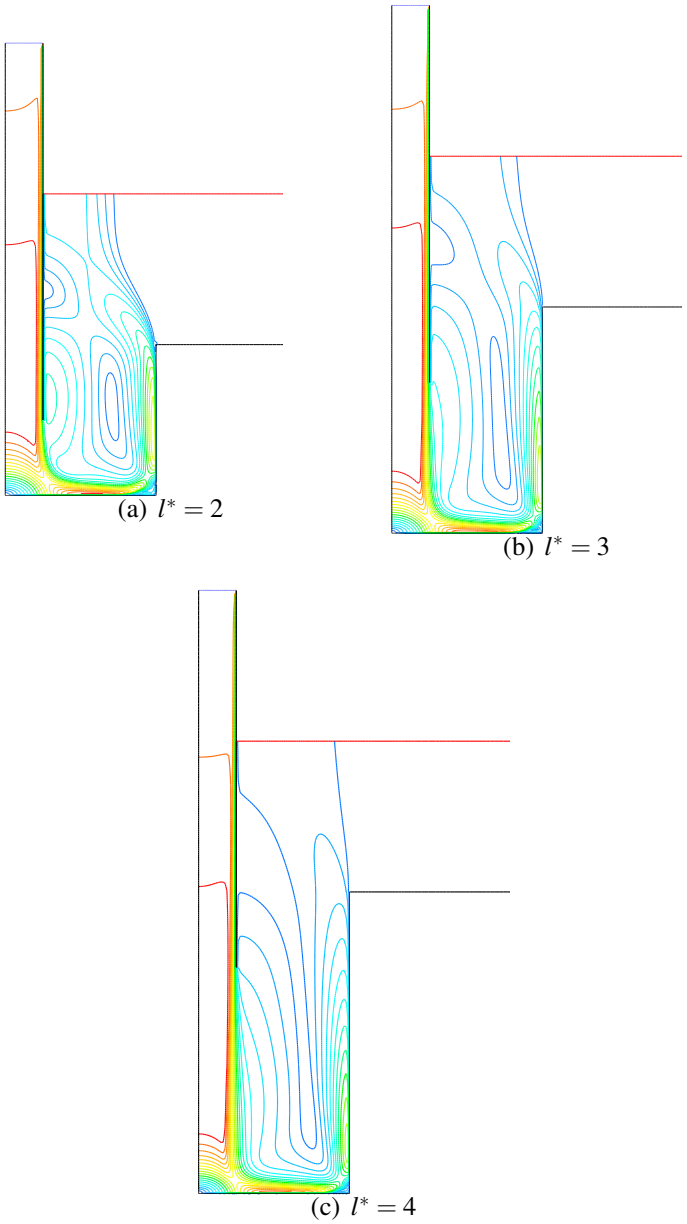

(a) $l^* = 2$ (b) $l^* = 3$ (c) $l^* = 4$

Figure 6.24: Velocity Contours, z^* = -1, d_c^* = 4, Re = 20,000

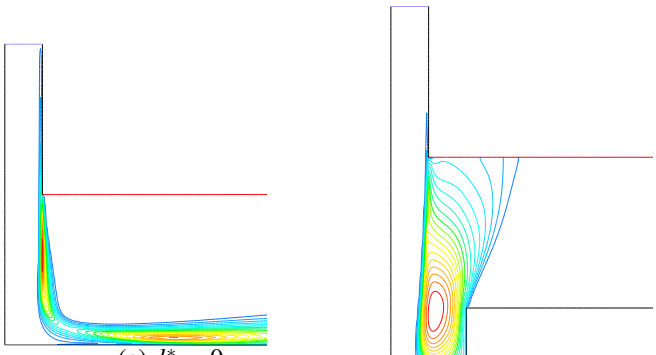

(a) $l^* = 0$

(b) $l^* = 1$

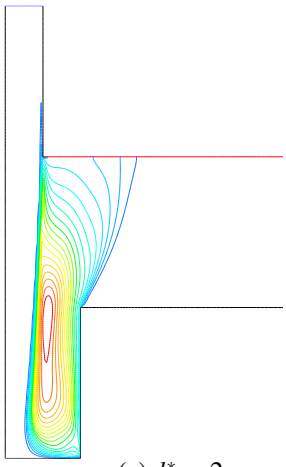

(c) $l^* = 2$

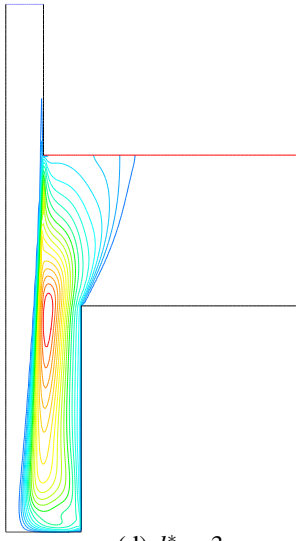

(d) $l^* = 3$

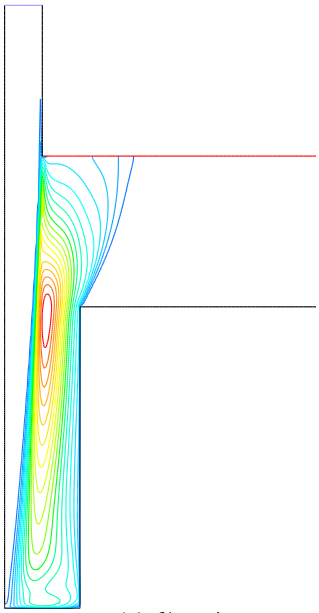

(e) $l^* = 4$

Figure 6.25: Contours of Turbulent Kinetic Energy, k, z^* = 2, d_c^* = 2, Re = 20,000

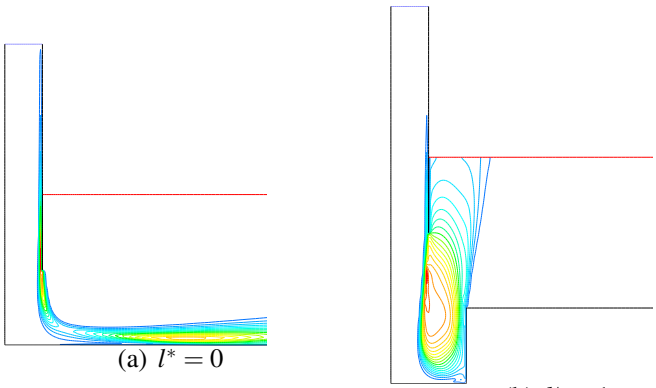

(a) $l^* = 0$

(b) $l^* = 1$

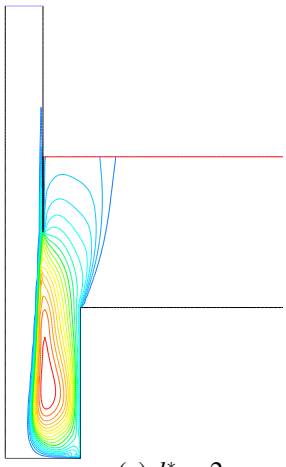

(c) $l^* = 2$

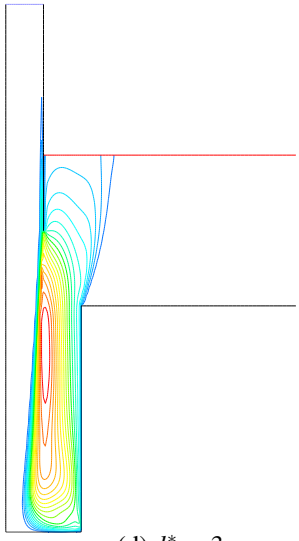

(d) $l^* = 3$

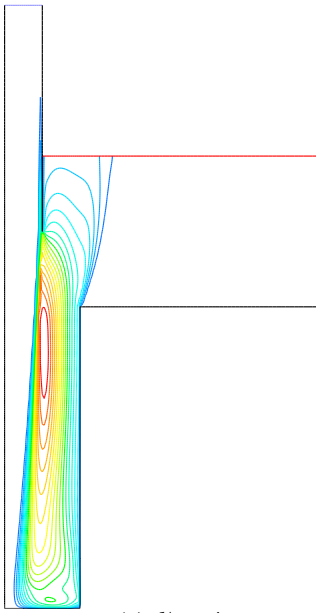

(e) $l^* = 4$

Figure 6.26: Contours of Turbulent Kinetic Energy, k, z^* = 1, d_c^* = 2, Re = 20,000

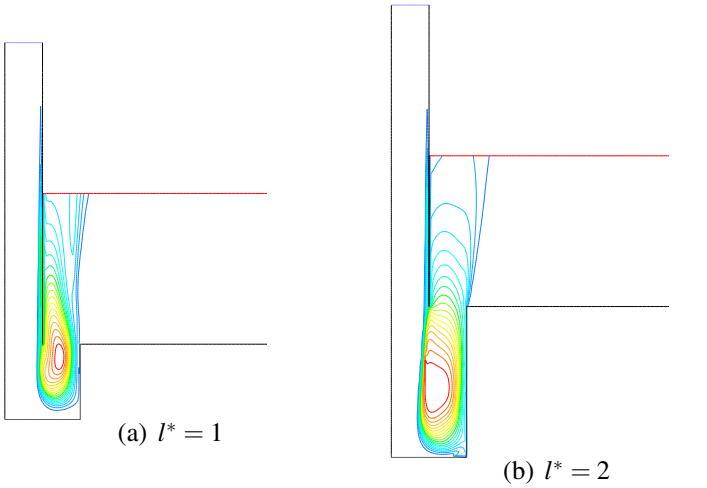

(a) $l^* = 1$

(b) $l^* = 2$

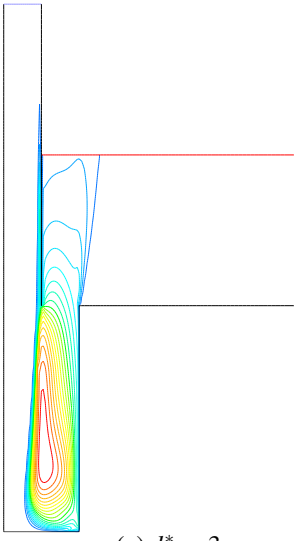

(c) $l^* = 3$

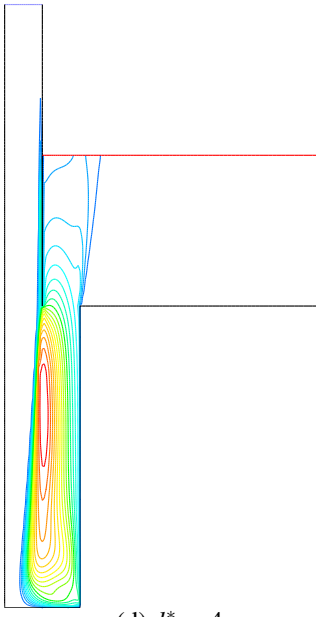

(d) $l^* = 4$

Figure 6.27: Contours of Turbulent Kinetic Energy, k, z^* = 0, d_c^* = 2, Re = 20,000

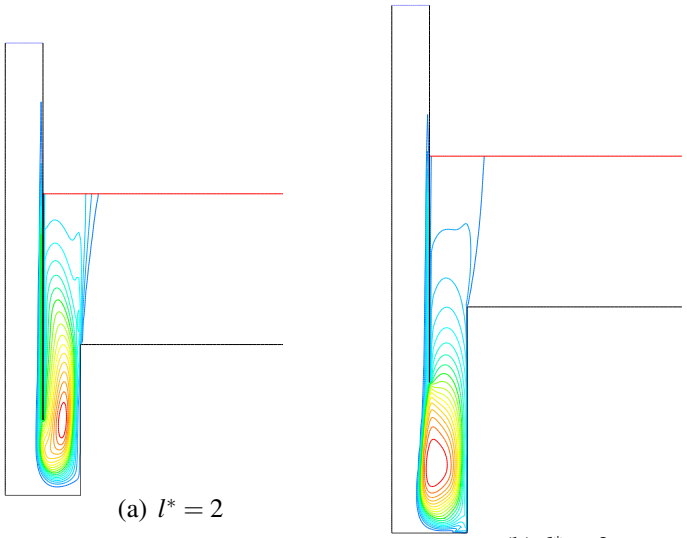

(a) $l^* = 2$ (b) $l^* = 3$

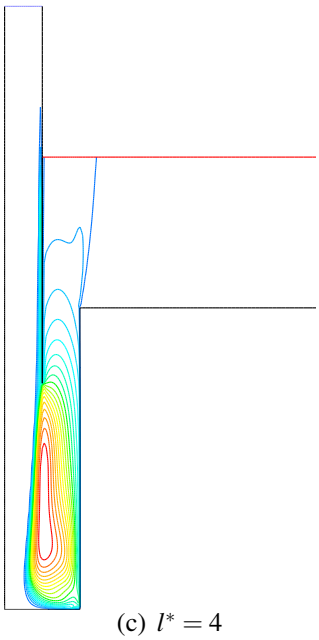

(c) $l^* = 4$

Figure 6.28: Contours of Turbulent Kinetic Energy, k, z^* = -1, d_c^* = 2, Re = 20,000

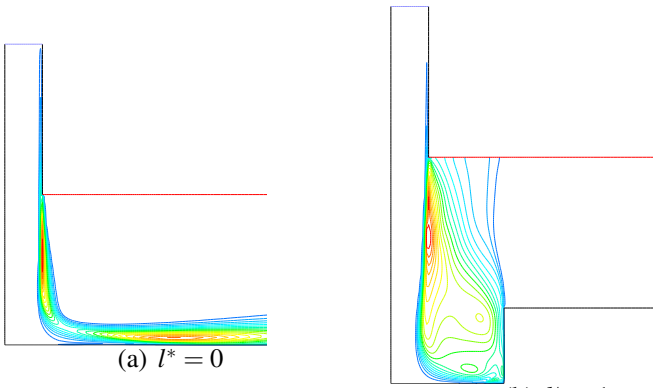

(a) $l^* = 0$ (b) $l^* = 1$

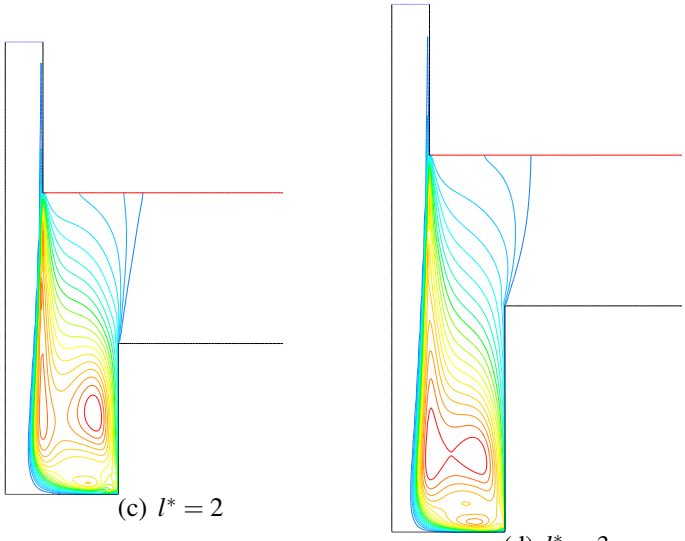

(c) $l^* = 2$ (d) $l^* = 3$

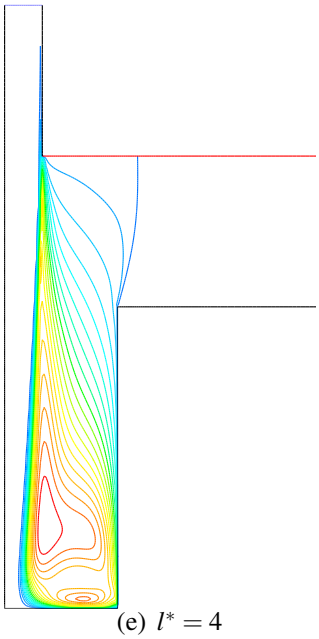

(e) $l^* = 4$

Figure 6.29: Contours of Turbulent Kinetic Energy, k, z^* = 2, d_c^* = 3, Re = 20,000

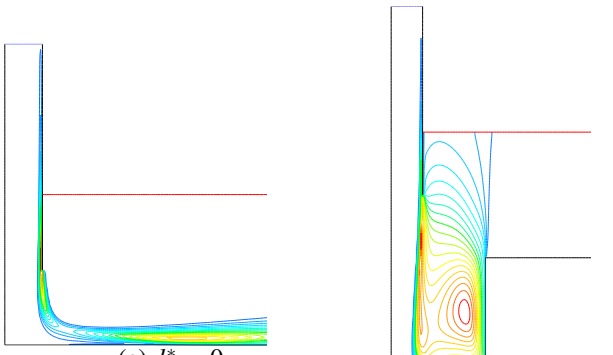

(a) $l^* = 0$

(b) $l^* = 1$

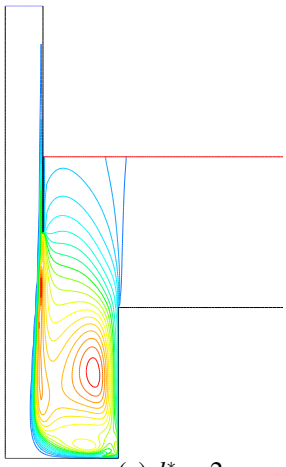

(c) $l^* = 2$

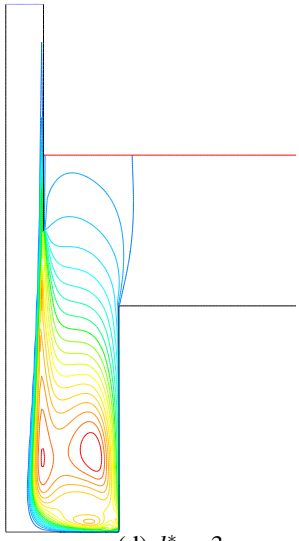

(d) $l^* = 3$

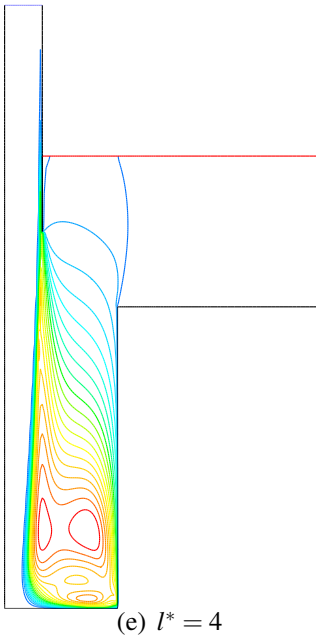

(e) $l^* = 4$

Figure 6.30: Contours of Turbulent Kinetic Energy, k, z^* = 1, d_c^* = 3, Re = 20,000

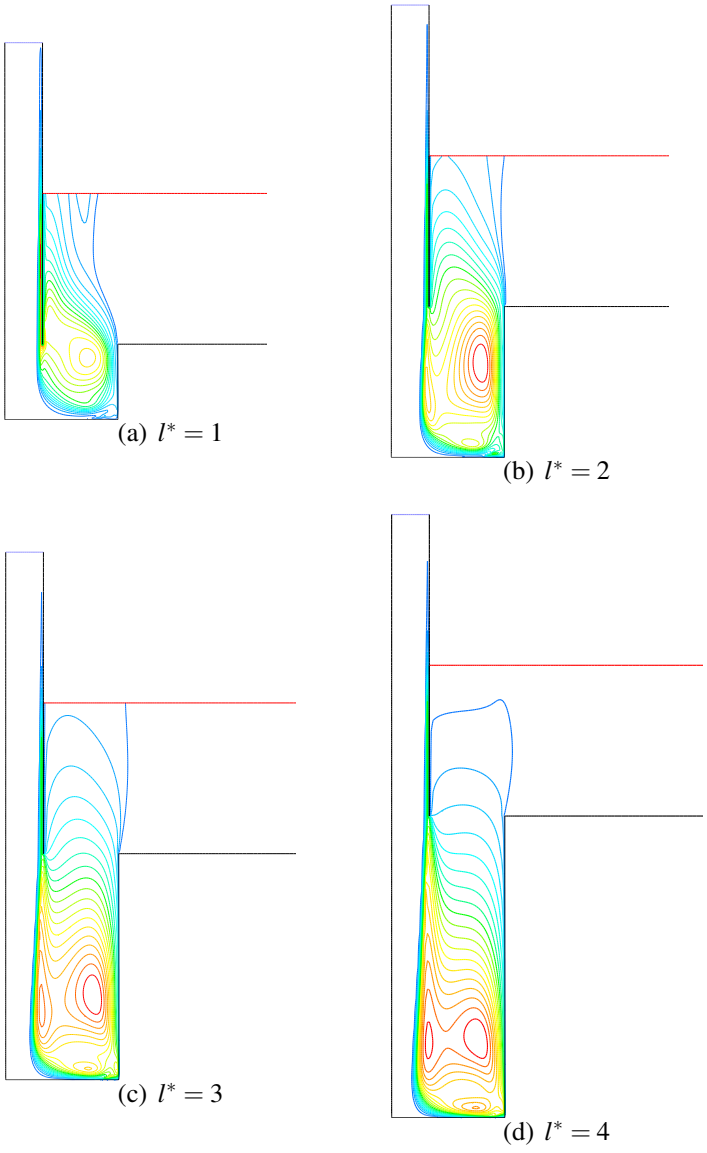

(a) $l^* = 1$ (b) $l^* = 2$

(c) $l^* = 3$ (d) $l^* = 4$

Figure 6.31: Contours of Turbulent Kinetic Energy, k, z^* = 0, d_c^* = 3, Re = 20,000

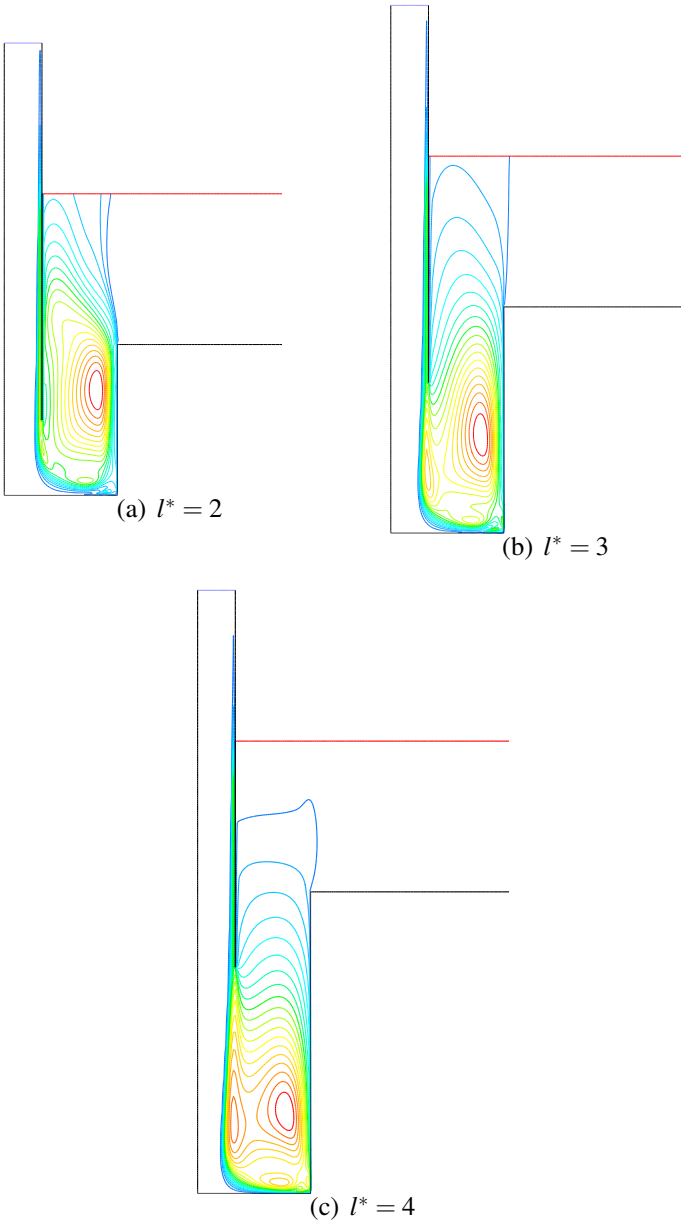

(a) $l^* = 2$

(b) $l^* = 3$

(c) $l^* = 4$

Figure 6.32: Contours of Turbulent Kinetic Energy, k, z^* = -1, d_c^* = 3, Re = 20,000

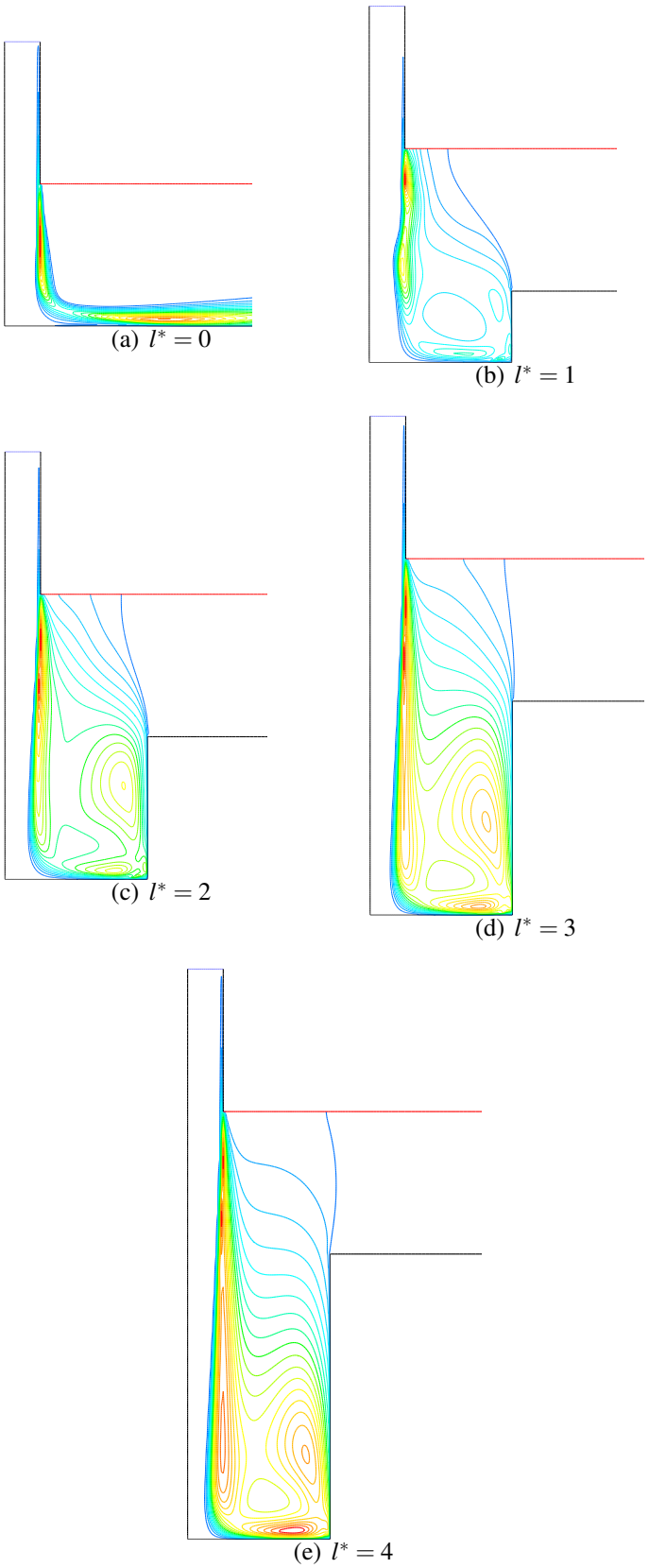

(a) $l^* = 0$

(b) $l^* = 1$

(c) $l^* = 2$

(d) $l^* = 3$

(e) $l^* = 4$

Figure 6.33: Contours of Turbulent Kinetic Energy, k, z^* = 2, d_c^* = 4, Re = 20,000

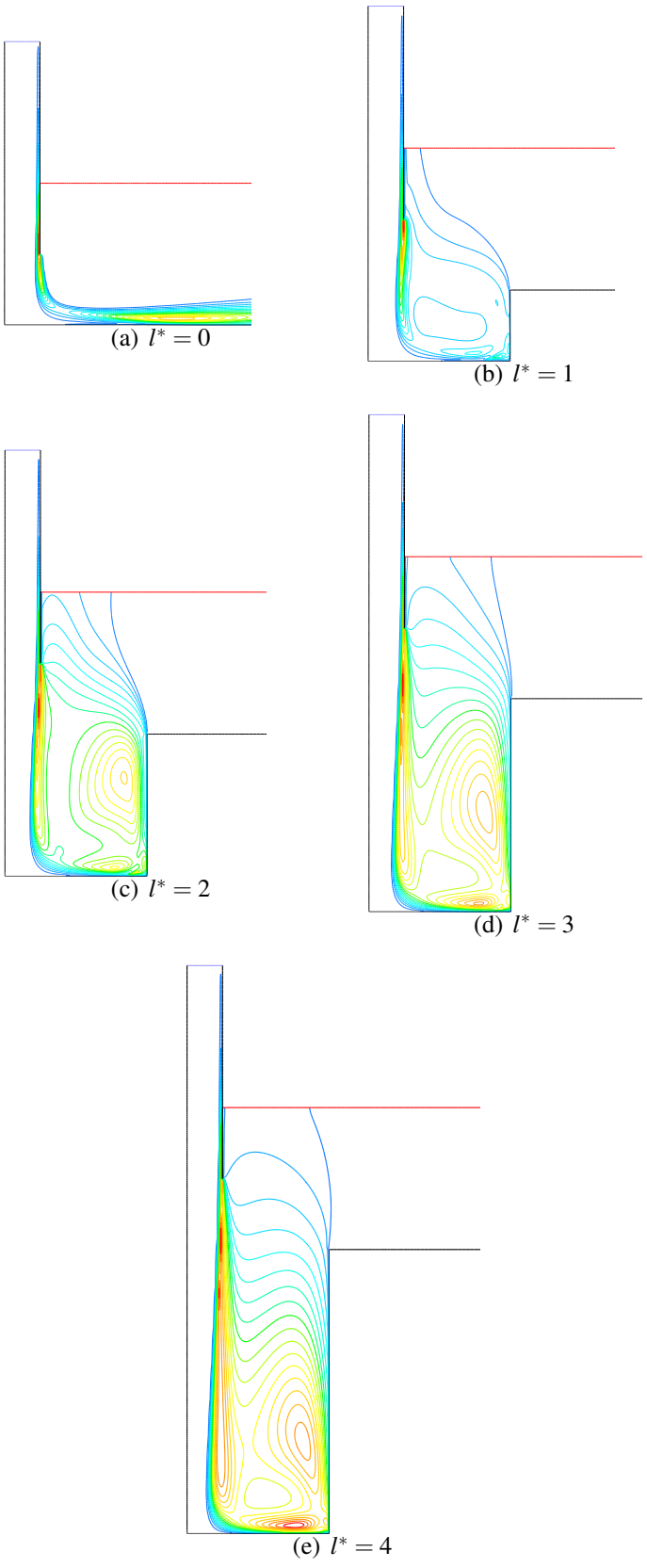

(a) $l^* = 0$

(b) $l^* = 1$

(c) $l^* = 2$

(d) $l^* = 3$

(e) $l^* = 4$

Figure 6.34: Contours of Turbulent Kinetic Energy, k, z^* = 1, d_c^* = 4, Re = 20,000

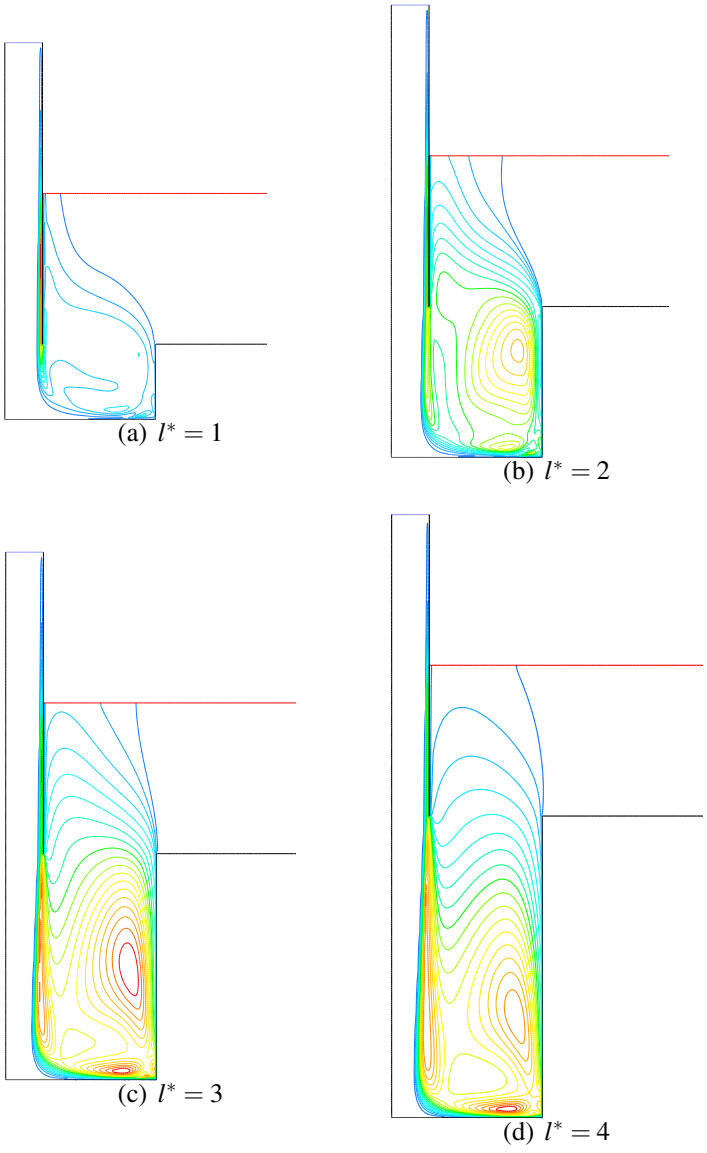

(a) $l^* = 1$ (b) $l^* = 2$

(c) $l^* = 3$ (d) $l^* = 4$

Figure 6.35: Contours of Turbulent Kinetic Energy, k, z^* = 0, d_c^* = 4, Re = 20,000

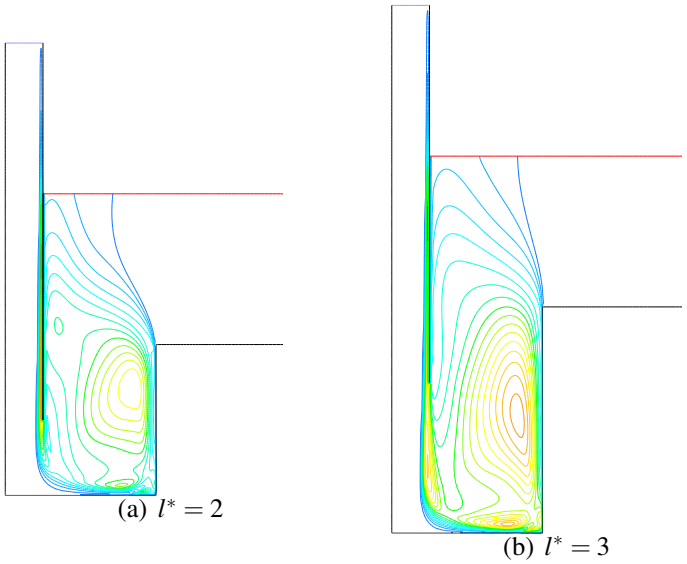

(a) $l^* = 2$ (b) $l^* = 3$

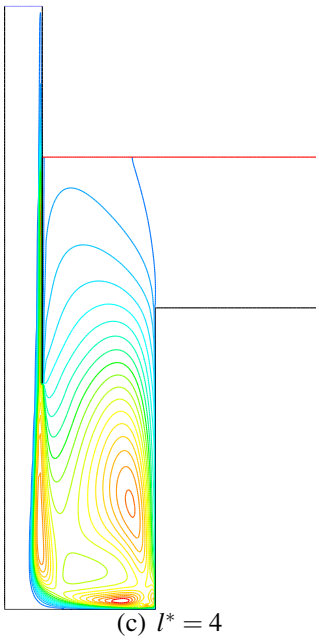

(c) $l^* = 4$

Figure 6.36: Contours of Turbulent Kinetic Energy, k, z^* = -1, d_c^* = 4, Re = 20,000

6.4.1 Net Cavity Depth

For the first group, where $z^* \leq 0$, the average surface Nusselt number was generally observed to increase as the net depth, L^*, increased. This trend was observed for almost all geometries in the group. The only exception occurred at a cavity diameter of $d_c^* = 4$ and at a Reynolds number of $\mathrm{Re} = 10,000$, where $\overline{\mathrm{Nu}}$ at $L^* = 2$ was higher than for $L^* = 3$.

For the second group, $\overline{\mathrm{Nu}}$ was dependent on both the cavity diameter and the Reynolds number. At small cavity diameters and low Reynolds numbers the first case when a cavity was present ($l^* = 1$) showed a reduction in the average Nusselt number, as evident in figures 6.4 and 6.5. However, as either of the Reynolds number or cavity diameter were increased the initial reduction in heat transfer became less acute or disappeared entirely, with figures 6.6, 6.7 and 6.10 showing only a minimal change in the Nusselt number. Furthermore, for the remaining combinations of Reynolds number and cavity diameter, the initial introduction of the cavity resulted in an increase in Nusselt number, as figures 6.8, 6.9, 6.11 and 6.12 indicate.

Ignoring these initial changes in Nusselt number due to the introduction of the cavity, the general trend was for the average Nusselt number, $\overline{\mathrm{Nu}}$, to increase as the net cavity depth increased.

Examination of the velocity and turbulent kinetic energy contour plots gives further insight into this observation. Figures 6.13 to 6.24 show contours of velocity magnitude for a sample of the cavity geometries studied, with z^* equal to 2, 1, 0 and -1, at a Reynolds number of 20,000.

At first, the analysis is simplified the by examining only a subset of the presented flow contours, limited to a single Reynolds number, cavity diameter and jet-to-surface distance. Figures 6.13 and 6.25 show the velocity magnitude and turbulent kinetic energy contour plots at a cavity diameter of $d_c^* = 2$, and a Reynolds number of 20,000. From these two figures it can be seen that as the net cavity depth, L^*, increased from 3 to 6, significant changes occurred in the velocity and turbulent kinetic energy distributions.

At $L^* = 3$, Figure 6.13(a) shows closely packed velocity contours near the base of the cavity, and none within the core of the jet. The lack of contours in the jet core indicates that there was minimal change to the momentum in this region for this case. The small change in momentum infers that minimal diffusion or mixing occurred between the flow into and out of the cavity, and consequently low heat transfer was observed. This is supported by the turbulent kinetic energy contours shown in Figure 6.25(a), where minimal change in the turbulent kinetic energy was apparent in the jet core until after the fluid had reached the base of the cavity.

As L^* increased, however, more momentum transfer occurred between the incoming core of the jet and the returning fluid, which in turn promoted mixing between the two streams and resulted in enhanced heat transfer compared with the case where $L^* = 3$. This is demonstrated in Figure 6.13(e), in which the core of the jet steadily lost momentum as the jet travelled towards the base of the cavity. The turbulent kinetic energy contours again support this observation, with Figure 6.25(e) showing increased levels of turbulence present in the flow near the heat transfer surface at the base of the cavity.

If the constraint on the jet-to-surface distance is removed, so that the jet-to-surface distance, z^*, is no longer limited to 2, similar observations can be made concerning the changes in heat transfer. The velocity and turbulent kinetic energy contour plots presented in figures 6.14 to 6.16 and figures 6.26 to 6.28 again lend support to the above explanation. As in the case where $z^* = 2$, for the cases where $z^* < 2$ an increase in the net cavity depth showed enhanced mixing between the jet core flow and the return flow streams, while turbulent kinetic energy production was also observed to be higher. The enhanced mixing and turbulence generation meant that increased heat transfer was observed from the base of the cavity as L^* was increased.

Reynolds number

Generally it is expected that an increase in the Reynolds number gives rise to a corresponding increase in heat transfer, since an increased Reynolds number is equivalent

to an increase in mass flux, with more fluid therefore available to transfer heat. This can be seen from figures 6.4 to 6.12 where for each geometry the corresponding heat transfer was observed to increase as the Reynolds number increased.

In addition to this trend secondary effects due to the Reynolds number were also observed. These affected the heat transfer in combination with the net cavity depth. For the second group of results, those in which the jet discharged above the reference surface, an increase in the Reynolds number resulted in the reduction or elimination of the drop in heat transfer that was observed due to the initial introduction of the cavity. Similarly, in the cases where the introduction of the cavity had no detrimental effect, an increase in the Reynolds number showed even further increases in heat transfer compared to lower Reynolds number cases.

Cavity Diameter

The cavity diameter generally had no direct effect on the average surface Nusselt number, rather changing the cavity diameter altered the effect of the changes due to the cavity depth or Reynolds number. This was observed predominantly at cavity diameters of 3 and 4 times the jet diameter, where the initial introduction of the cavity resulted in increased heat transfer, compared to the reduction observed at a cavity diameter of 2 times the jet diameter.

6.5 Conclusions

The surface cavity surface modification presented in this chapter is a novel method for increasing the heat transfer from an impinging jet system. The potential for heat transfer was examined for simple cylindrical cavities of varying depths and diameters, at a range of Reynolds numbers and for various jet-to-surface distances. The results indicate significant heat transfer enhancement is possible using this technique, with up to a 45% increase observed for some cases. The key parameter affecting the heat transfer from the cavity was found to be the ‘net cavity depth’, which roughly corresponds to

the distance between the exit of the jet nozzle and the base of the cavity. The cavity diameter was found to have a minimal direct impact on the heat transfer from the cavity, instead it was found to alter the changes in heat transfer due to the net cavity depth and Reynolds number.

Additionally, the results presented in this chapter did not take into account any heat transfer from the side-walls of the cavity. Allowing heat transfer from these surfaces in addition to the heat transfer from the base should allow even further gains in heat transfer to be realised.

Chapter 7

Impinging Jet Arrays

The previous two chapters of this thesis investigated two effective schemes to enhance the heat transfer rate from individual impinging jets. For situations where high heat fluxes are spread over a large area, however, a single impinging jet is often unsuitable. This is due to the highly localised nature of the heat transfer. For these cases arrays of impinging jets are employed, as an array provides a more even distribution of heat transfer. Chapter 2 discussed many previous studies on impinging jet arrays, while highlighting an absense of research into providing generalised correlations on the optimal geometry required to provide the maximum heat transfer from an array. This chapter presents a detailed study on the heat transfer characteristics of arrays of impinging jets. Additionally, correlations for determining the heat transfer from an array of jets of different geometries are presented.

7.1 Methodology

The work presented in this chapter considers 'large' arrays with jet diameters that were considerably smaller than the total size of the array. In this sense, a 'large' array is one where the number of jets around the perimeter of the array is small in comparison to the number of internal jets. Limiting the investigation to these types of arrays allowed a single 'representative jet' to be considered for each array geometry, resulting in significant savings in simulation time. A representative jet describes equally any individual jet in the internal region of the array, and enables conclusions drawn from the representative jet to be extended to the array as a whole. An additional advantage of studying a 'large' array is the smaller computational domain required when compared with smaller arrays. In a large array any internal jet is interchangeable with any other and the perimeter jets have only a small effect on the observed heat transfer. However

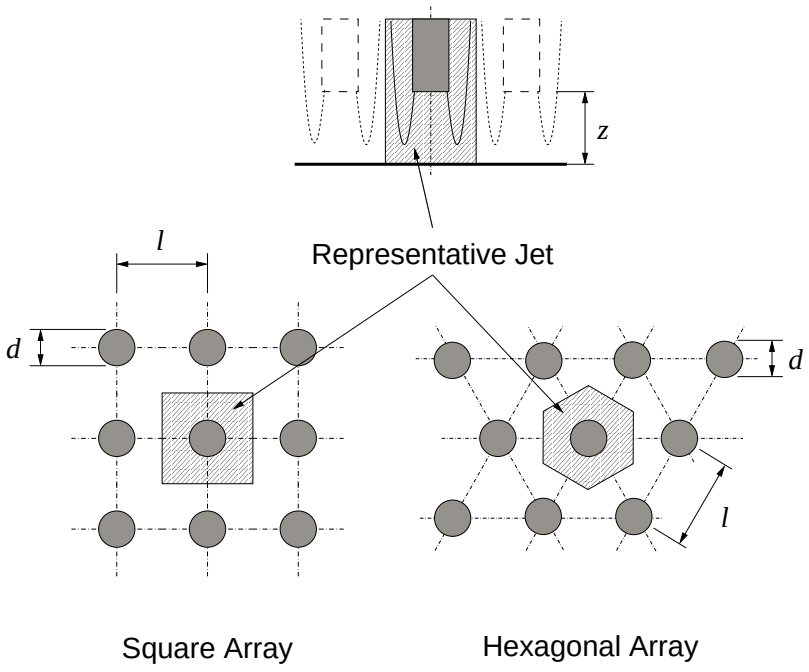

Figure 7.1: Representative jets for square and hexagonal jet arrays

for smaller arrays the perimeter jets affect the whole array enough to warrant these including these jets in the computational domain. Two possible configurations of the arrays were examined, arranged in either square or hexagonal configurations as shown in Figure 7.1.

To determine the relative performance the average Nusselt number for the heat transfer surface was calculated for each array, where

$$\overline{\mathrm{Nu}} = \frac{\dot{q}d}{4l^2 k_f \Delta T} \tag{7.1}$$

for a square array and

$$\overline{\mathrm{Nu}} = \frac{2\dot{q}d}{3\sqrt{3}l^2 k_f \Delta T} \tag{7.2}$$

for a hexagonal array.

The Nusselt numbers calculated for each array were further analysed to correlate the heat transfer from a given array of impinging jets against the jet-to-surface distance, Reynolds number and jet-to-jet spacing. Turbulence in the flow was accounted for

using the $\overline{v}^2$-f turbulence model in accordance with the conclusions of Chapter 4

7.2 Simulation Parameters

A parametric study was performed in order to investigate a range of possible impinging jet arrays. The parameters investigated for each arrangement were the distance between any two adjacent jets, l, the jet velocity, V, and the jet-to-surface distance, z. Each of the parameters investigated was non-dimenionalised with respect to the jet diameter and the ranges for each are presented in Table 7.1.

Parameter	Variable	Non-dimensionalised	Values
Jet-to-Jet Spacing	l/d	l^*	1.5, 2, 2.5, 3, 4, 5, 6, 7
Jet Velocity	$\rho V d/\mu$	Re	200, 500, 1000, 2000, 5000, 10000, 23000, 30000
Jet-to-surface height	z/d	z^*	2, 4, 6

Table 7.1: Parameter Ranges for jet array

7.2.1 Boundary Conditions

The heated surface was modelled as an isothermal boundary with the surface temperature set to 25 ^{o}C above the jet inlet temperature. The jet inlet boundary was modelled as velocity inlet with a uniform velocity profile with the magnitude of the velocity determined from the desired jet Reynolds number. The outlet portion of the top boundary was modelled as a constant pressure outlet with the reference pressure set to zero. The jet wall was modelled as an infinitely thin adiabatic wall with a no-slip velocity constraint on the adjacent flow. The vertical sides of the domain were modelled as symmetry conditions.

7.2.2 Mesh

The computational domain was further simplified for simulation by allowing for additional symmetries that were present in the single representative jet. A regular hexa-

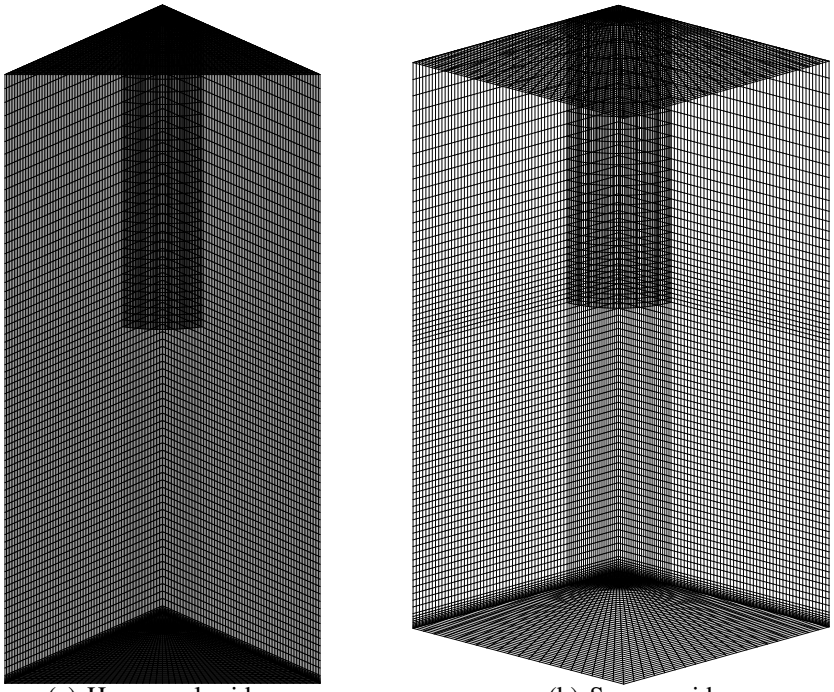

(a) Hexagonal grid (b) Square grid

Figure 7.2: Sample of meshes used for parametric studies

hedral grid was used to mesh the domain and grid independency checks and boundary layer refinement were conucted in accordance with Chapter 3. Figure 7.2 shows example grids for jet-to-jet spacings of 4 jet diameters at a jet-to-surface distance of two jet diameters.

7.3 Results and Discussion

This section presents results for each of the array geometries and the underlying trends are identified and discussed. Section 7.3.1 presents the heat transfer results in terms of the average Nusselt number for the two configurations of jet arrays studied, while sections 7.3.2, 7.3.3 and 7.3.4 discuss in detail the observed trends as each of the jet-to-jet spacing, Reynolds number and jet-to-surface distance were varied. Section 7.3.5 presents correlations to determine the heat transfer from a given infinite array of impinging jets. These correlations also aid the analysis by quantifying the influence on

heat transfer due to each of the investigated parameters.

7.3.1 Average Nusselt Number

Figures 7.3 to 7.5 show the average Nusselt number for square arrays as the jet-to-jet spacing was changed while figures 7.6 to 7.8, show similar information for hexagonal arrays. These figures present the heat transfer results for the complete range of Reynolds number studied.

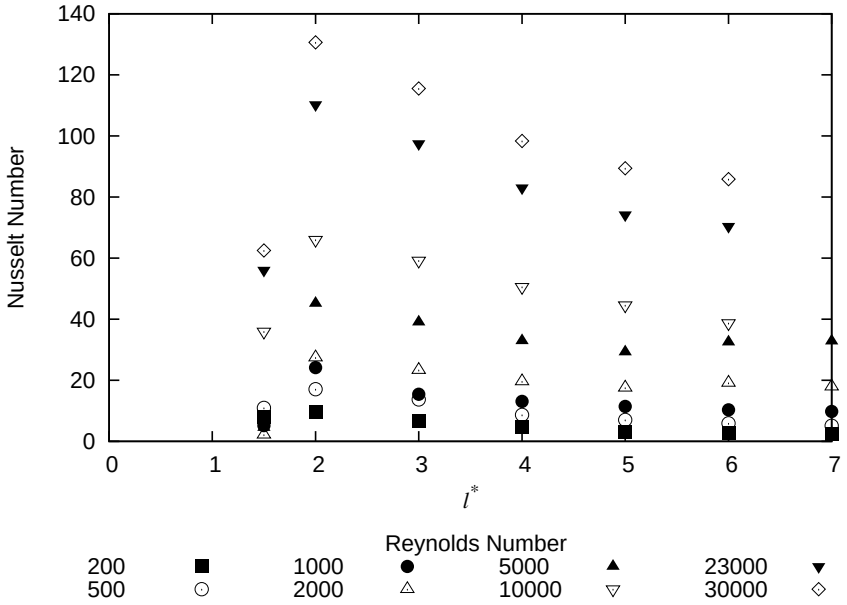

Figure 7.3: Average surface Nusselt number, square array, z^*=2

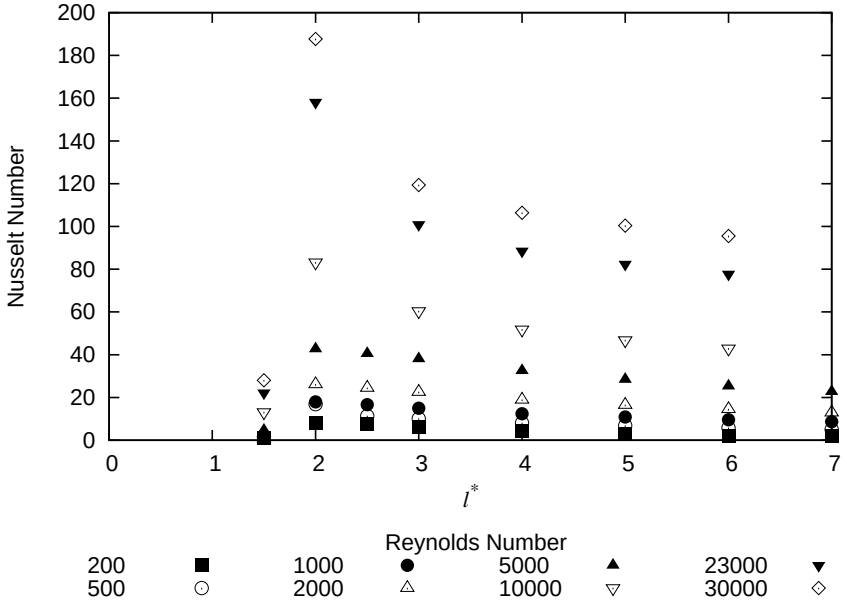

Figure 7.4: Average surface Nusselt number, square array, z^*=4

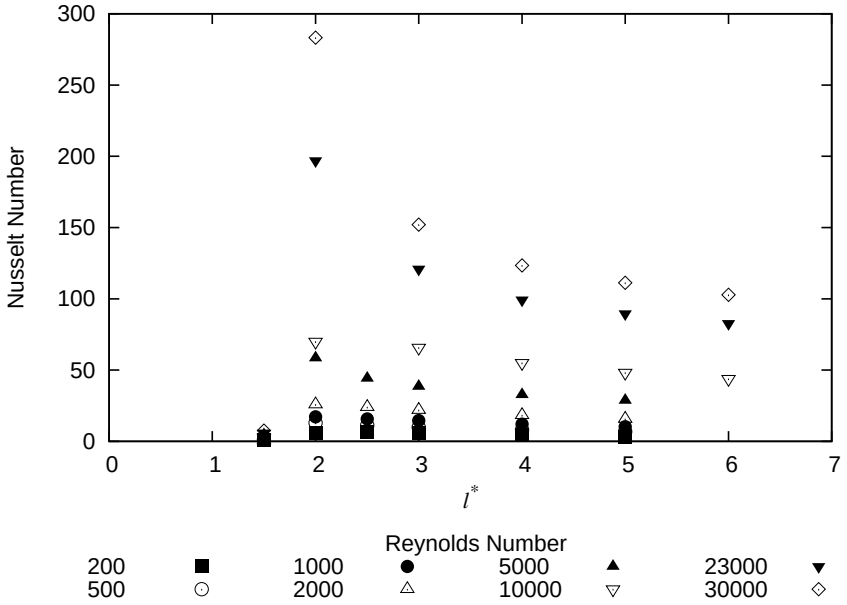

Figure 7.5: Average surface Nusselt number, square array, z^*=6

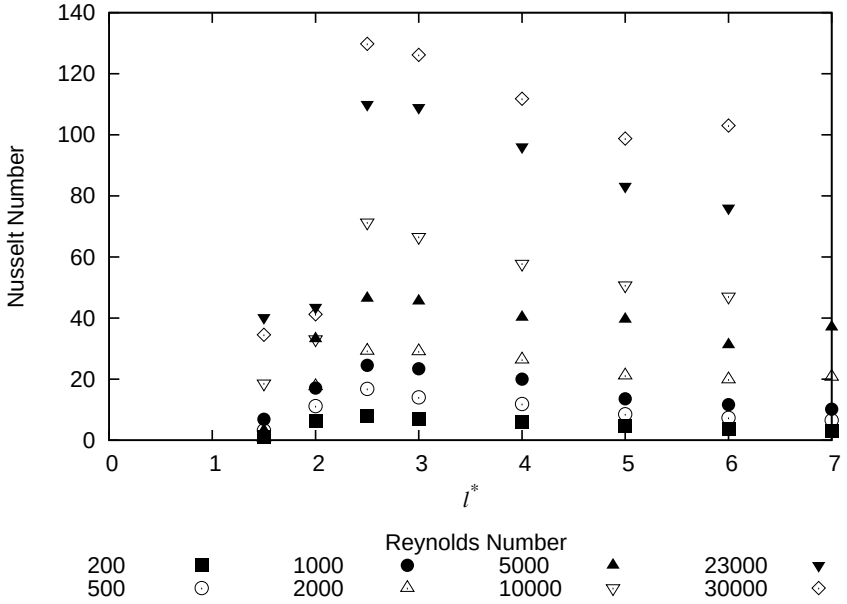

Figure 7.6: Average surface Nusselt number, hexagonal array, z^*=2

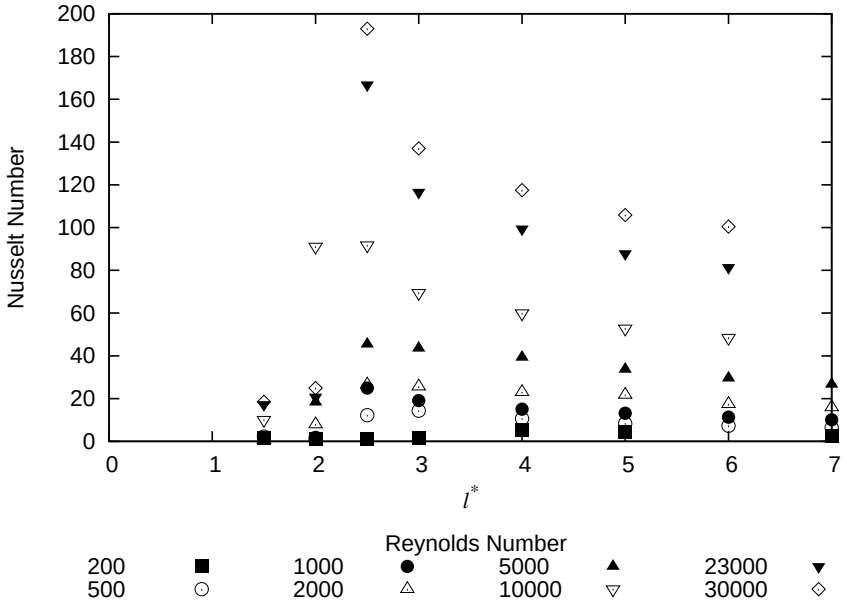

Figure 7.7: Average surface Nusselt number, hexagonal array, z^*=4

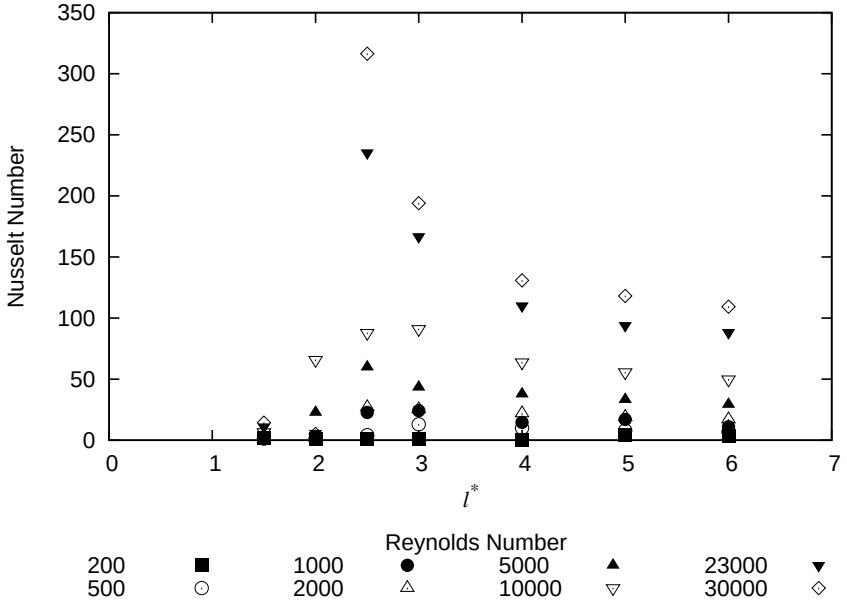

Figure 7.8: Average surface Nusselt number, hexagonal array, z^*=6

7.3.2 Jet-to-jet Spacing

From the results it is apparent that the average Nusselt number was highly dependent on the jet-to-jet spacing. Generally the heat transfer from the array increased as the jet-to-jet spacing decreased. However, it was also observed that a critical spacing existed, below which the heat transfer was significantly reduced. This reduction in heat transfer became more acute as the Reynolds number increased, though the actual spacing at which this occurred was observed to be independent of the Reynolds number. The critical spacing for each configuration was also found to be independent of the jet-to-surface distance, with similar values observed for each of the jet-to-surface distances simulated. The actual decrease in heat transfer below the critical spacing, however, was more acute at lower jet-to-surface distances.

Even though the value for the critical spacing was observed to be independent of the Reynolds number and jet-to-surface distance, the critical spacing was found to be affected by the arrangement of the jet array. For the square array the critical spacing was found to lie between 1.5 and 2 jet diameters, while for the hexagonal array the value was between 2 and 2.5 jet diameters.

To understand why a critical spacing exists it is necessary to examine the flow fields for each of the arrays. Figures 7.15, 7.16 and 7.17 show contours of velocity magnitude for the square array at a Reynolds number of 5000, a typical mid-range value, for l^* between 1.5 and 5 and for jet-to-surface distances of 2, 4 and 6. From these figures it can be seen that as the jet-to-jet spacing was decreased the area available for the fluid to exit the domain reduced. This reduction in area means that when the spacing became less than the critical value, the momentum of the jet was insufficient to reach the heated surface and the jet 'short-circuited' the domain with the end effect being to lower the observed heat transfer rate. Figures 7.18, 7.19 and 7.20 show similar contours of velocity magnitude for the hexagonal array. Again it is observed that below the critical spacing, the jet fails to reach the surface and the heat transfer is significantly reduced. For both the square and hexagonal arrays similar trends were observed at all the jet-to-surface distances studied.

7.3.3 Reynolds Number

The primary effect of increasing the Reynolds number of the jet was to increase the average heat transfer from the target surface. As with the previous investigations this was expected as a larger Reynolds number meant more fluid was available to remove heat from the surface.

A secondary observation that was made when the Reynolds number was changed was the effect that the Reynolds number had on the severity of the reduction in heat transfer when the jet-to-jet spacing was decreased below the critical value. At high Reynolds numbers, above approximately 5000, the reduction in heat transfer was significant, whereas at lower Reynolds numbers the heat transfer decreased less quickly from the peak value. Again a better understanding this phenomenon can be gained be examining the differences between the flow patterns for cases at high Reynolds number and those at lower Reynolds numbers.

For a typical high Reynolds number case, figures 7.22(a) and 7.22(b) show the contours of velocity magnitude for a Reynolds number of 30,000 at jet-to-jet spacings just above and just below the critical spacing for a square array. In the first figure it can be seen that the flow from the jet nozzle easily reached the heat transfer surface and as such the heat transfer was high. Contrasting this with the second figure, as discussed in the previous section the flow did not reach the heat transfer surface, instead the fluid 'short circuited' the domain and flowed almost directly out of the array. The reduction in the amount of fluid that reached the heat transfer surface can account for the severe drop in heat transfer that was calculated when the jet-to-jet spacing was below the critical value.

For a typical low Reynolds numbercase, figures 7.10(a) and 7.10(b) show the contours of velocity magnitude for a Reynolds number of 200, again at jet-to-jet spacings just above and just below the critical value for a square array. In the first figure the flow looks similar to that of the high Reynolds number case, where the fluid reached the heat transfer surface as desired, and therefore reasonable heat transfer was observed. For the second figure, where the jet-to-jet spacing was below the critical value, the flow at the

lower Reynolds number showed significant differences than for the higher Reynolds number case. In this figure the flow could still be seen to reach the heat transfer surface, though with less momentum than the case where the jet-to-jet spacing was above the critical value. The net effect of this was that the heat transfer was not reduced as much as for the high Reynolds number case.

When examining the hexagonal array configuration the same observations hold, albeit that the value for the critical jet-to-jet spacing is higher than for the square configuration. Figures 7.25(a) and 7.25(b) show contours of velocity magnitude for a Reynolds number of 30,000 at jet-to-jet spacings of 2 and 2.5, while figures 7.13(a) and 7.13(b) show similar information for a Reynolds number of 200.

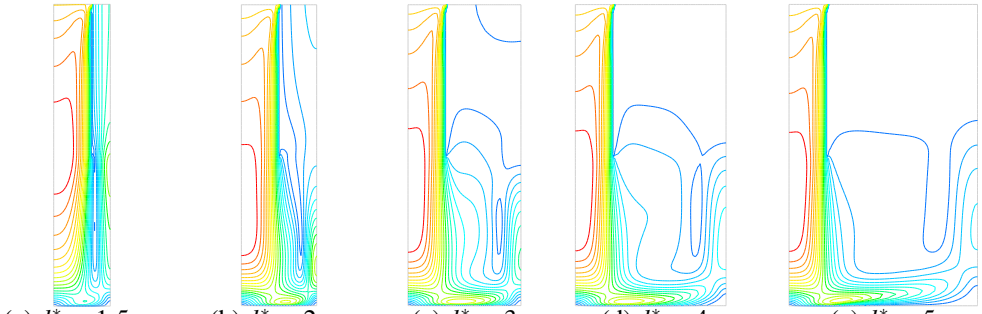

(a) $l^* = 1.5$ (b) $l^* = 2$ (c) $l^* = 3$ (d) $l^* = 4$ (e) $l^* = 5$

(f) $l^* = 6$

Figure 7.9: Velocity Contours, Square Array, z^* = 2, Re = 200

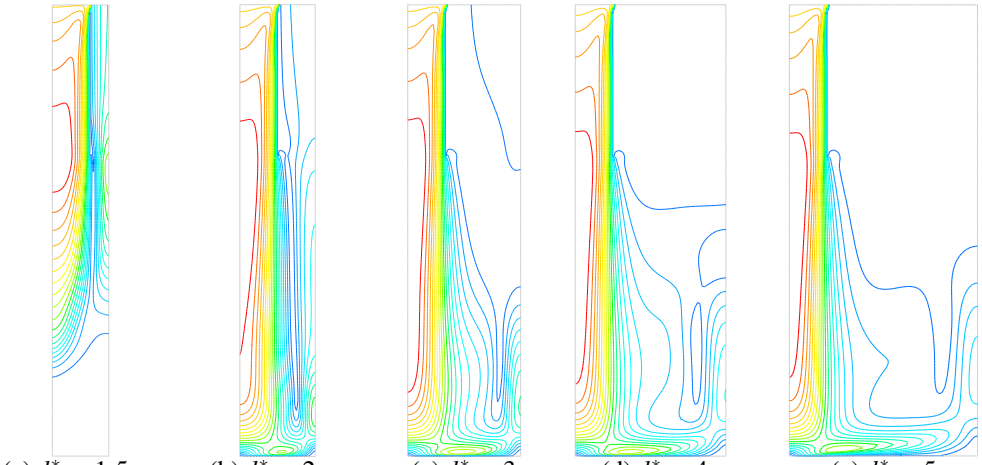

(a) $l^* = 1.5$ (b) $l^* = 2$ (c) $l^* = 3$ (d) $l^* = 4$ (e) $l^* = 5$

(f) $l^* = 6$

Figure 7.10: Velocity Contours, Square Array, z^* = 4, Re = 200

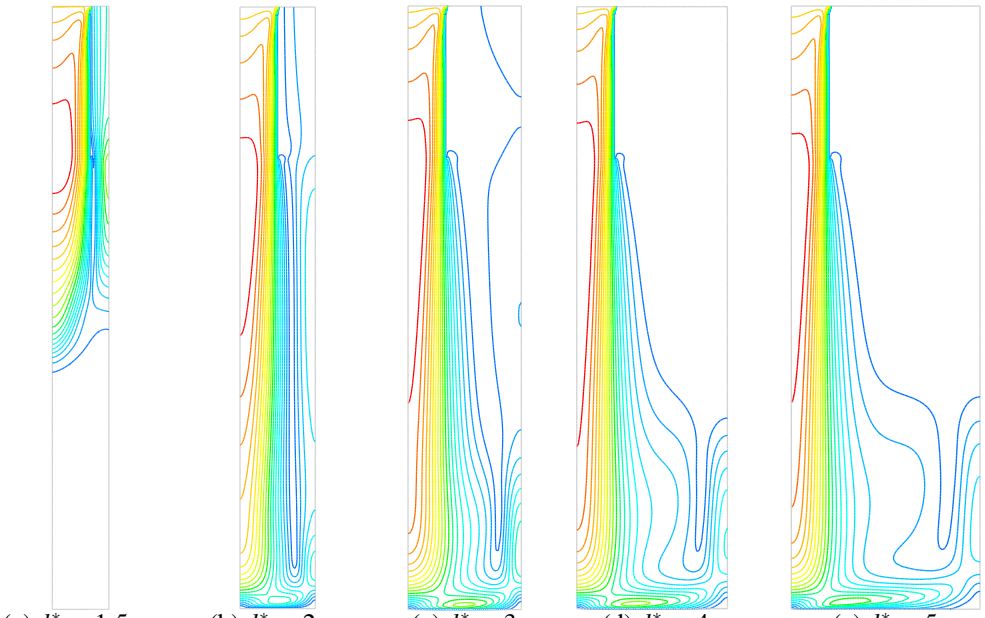

(a) $l^* = 1.5$ (b) $l^* = 2$ (c) $l^* = 3$ (d) $l^* = 4$ (e) $l^* = 5$

Figure 7.11: Velocity Contours, Square Array, z^* = 6, Re = 200

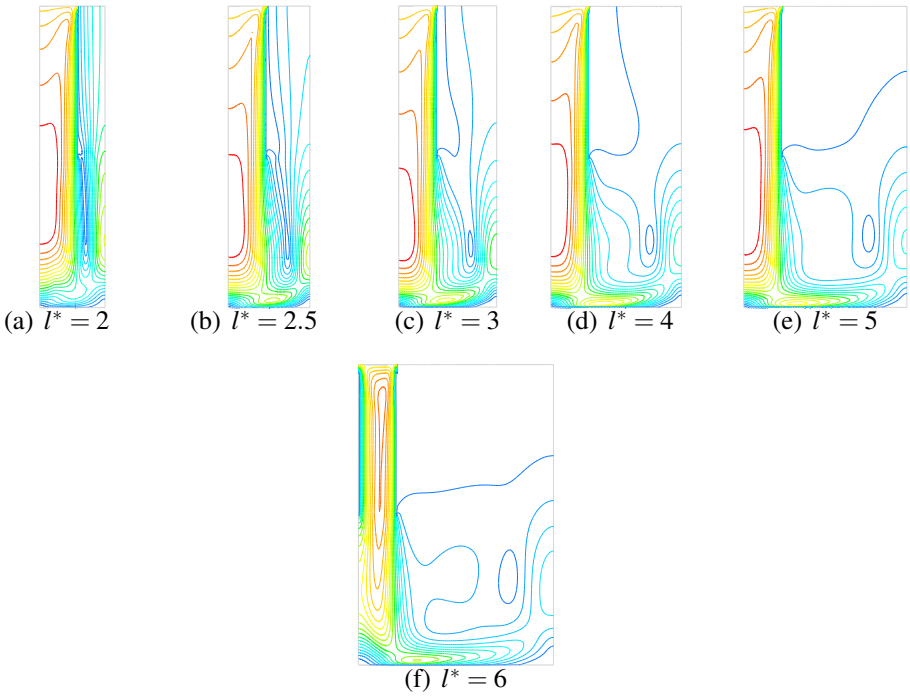

(a) $l^* = 2$ (b) $l^* = 2.5$ (c) $l^* = 3$ (d) $l^* = 4$ (e) $l^* = 5$

(f) $l^* = 6$

Figure 7.12: Velocity Contours, Hexagonal Array, z^* = 2, Re = 200

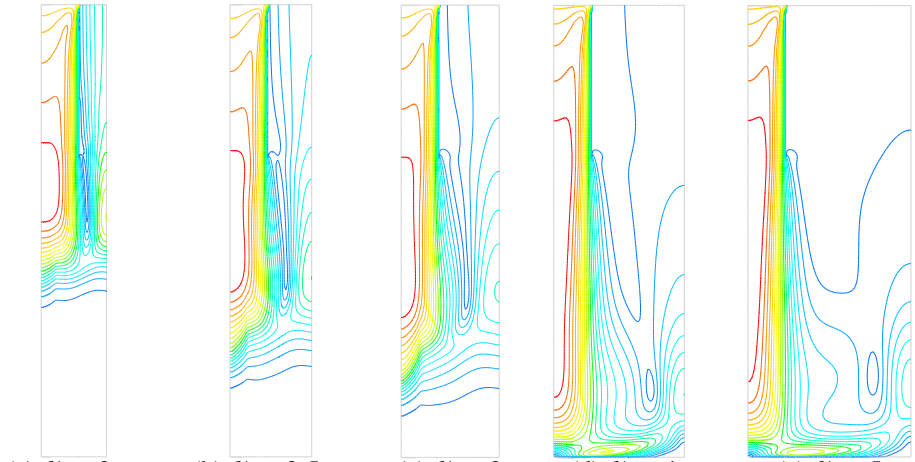

(a) $l^* = 2$ (b) $l^* = 2.5$ (c) $l^* = 3$ (d) $l^* = 4$ (e) $l^* = 5$

Figure 7.13: Velocity Contours, Hexagonal Array, z^* = 4, Re = 200

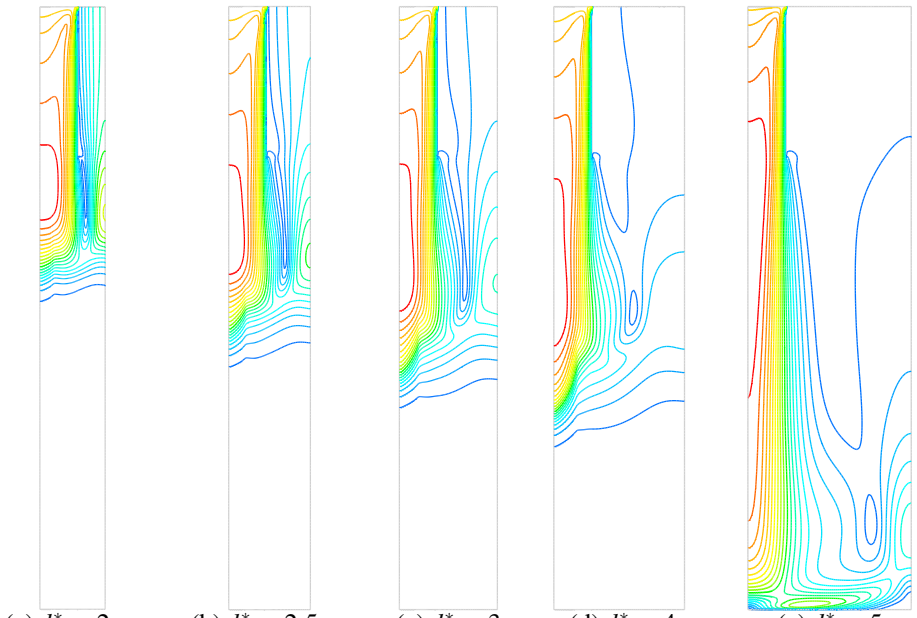

(a) $l^* = 2$ (b) $l^* = 2.5$ (c) $l^* = 3$ (d) $l^* = 4$ (e) $l^* = 5$

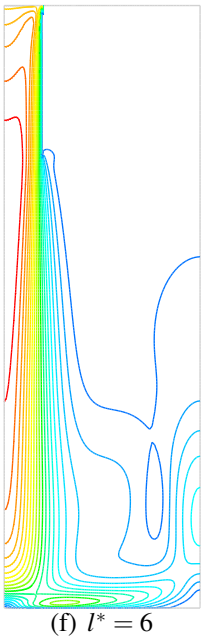

(f) $l^* = 6$

Figure 7.14: Velocity Contours, Hexagonal Array, z^* = 6, Re = 200

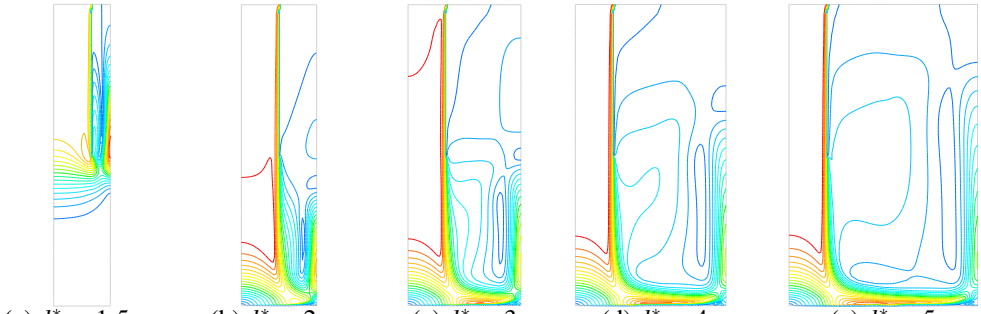

(a) $l^* = 1.5$ (b) $l^* = 2$ (c) $l^* = 3$ (d) $l^* = 4$ (e) $l^* = 5$

(f) $l^* = 6$

Figure 7.15: Velocity Contours, Square Array, z^* = 2, Re = 5,000

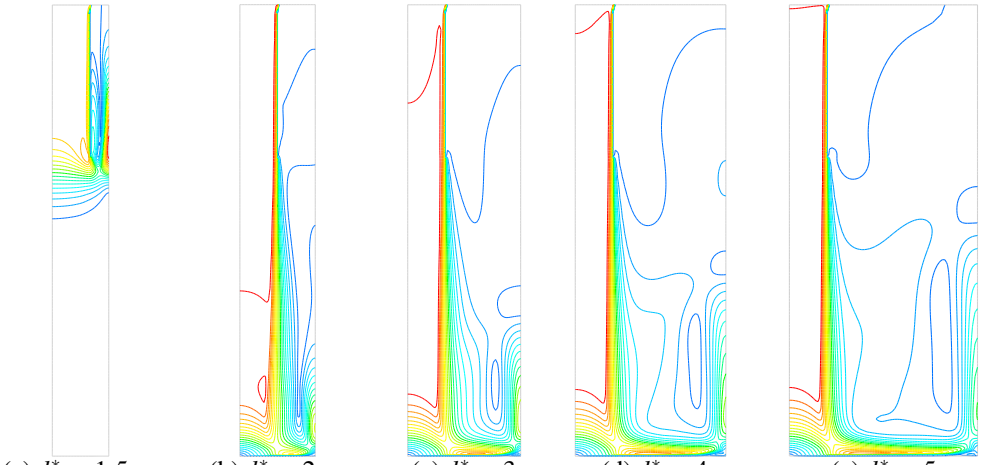

(a) $l^* = 1.5$ (b) $l^* = 2$ (c) $l^* = 3$ (d) $l^* = 4$ (e) $l^* = 5$

(f) $l^* = 6$

Figure 7.16: Velocity Contours, Square Array, z^* = 4, Re = 5,000

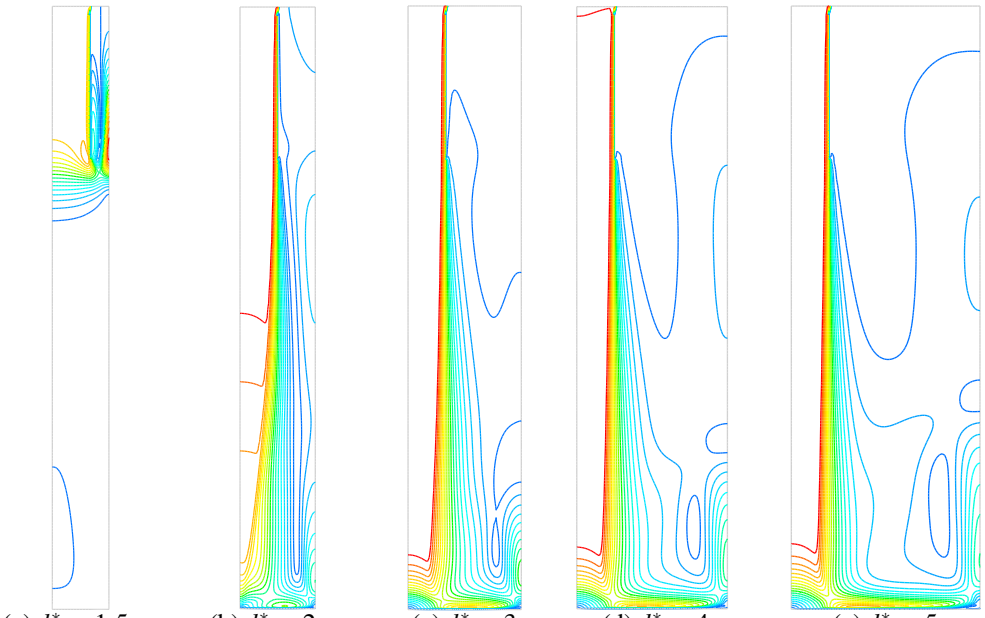

(a) $l^* = 1.5$ (b) $l^* = 2$ (c) $l^* = 3$ (d) $l^* = 4$ (e) $l^* = 5$

Figure 7.17: Velocity Contours, Square Array, z^* = 6, Re = 5,000

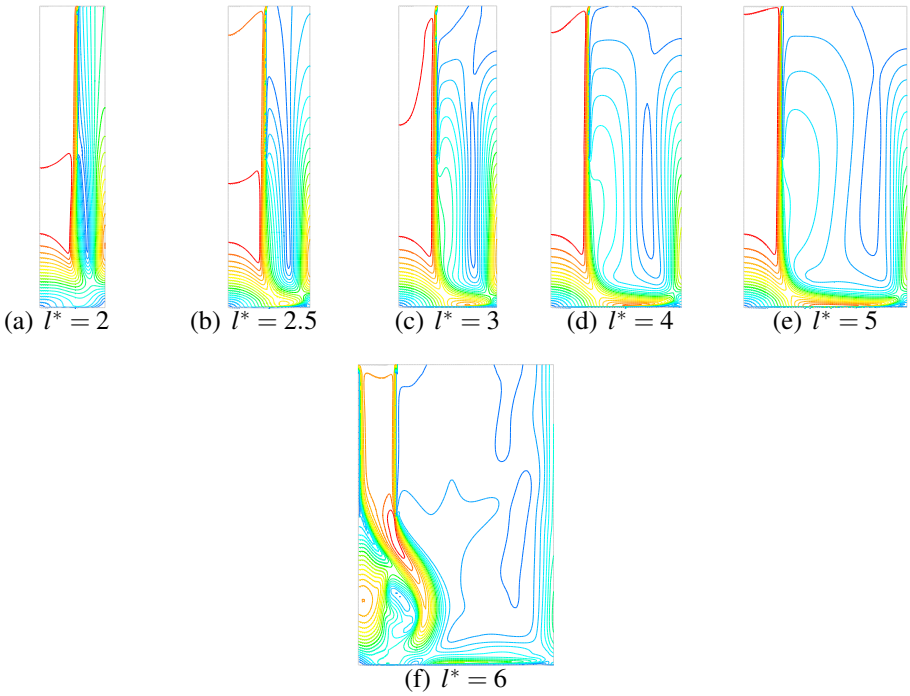

(a) $l^* = 2$ (b) $l^* = 2.5$ (c) $l^* = 3$ (d) $l^* = 4$ (e) $l^* = 5$

(f) $l^* = 6$

Figure 7.18: Velocity Contours, Hexagonal Array, z^* = 2, Re = 5,000

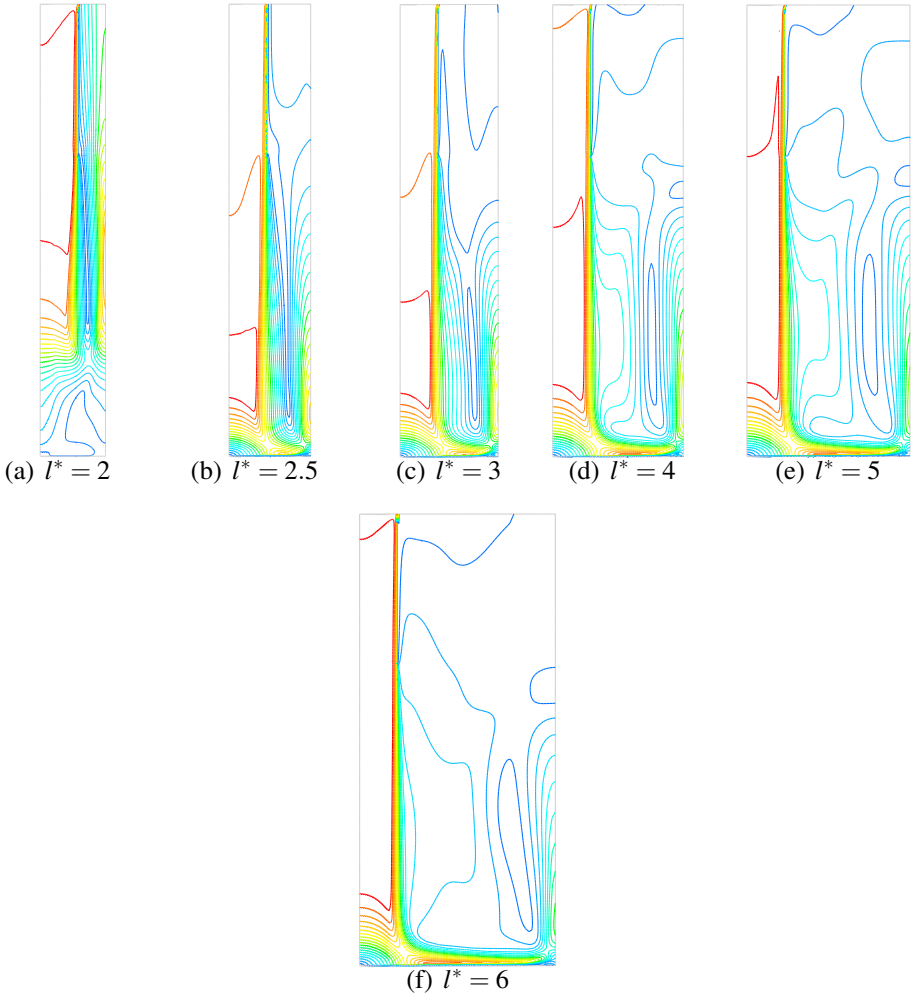

(a) $l^* = 2$ (b) $l^* = 2.5$ (c) $l^* = 3$ (d) $l^* = 4$ (e) $l^* = 5$

(f) $l^* = 6$

Figure 7.19: Velocity Contours, Hexagonal Array, z^* = 4, Re = 5,000

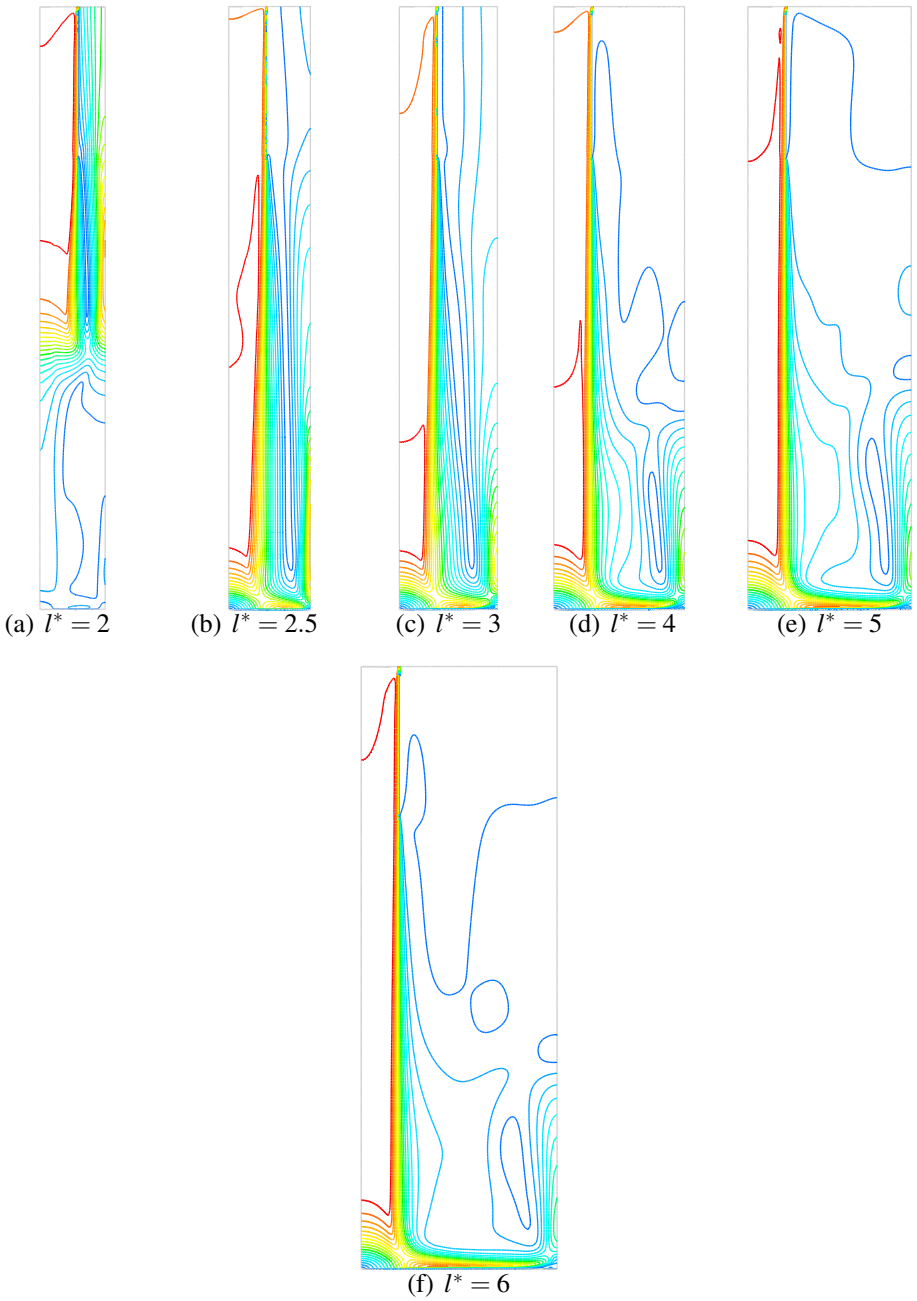

(a) $l^* = 2$ (b) $l^* = 2.5$ (c) $l^* = 3$ (d) $l^* = 4$ (e) $l^* = 5$

(f) $l^* = 6$

Figure 7.20: Velocity Contours, Hexagonal Array, z^* = 6, Re = 5,000

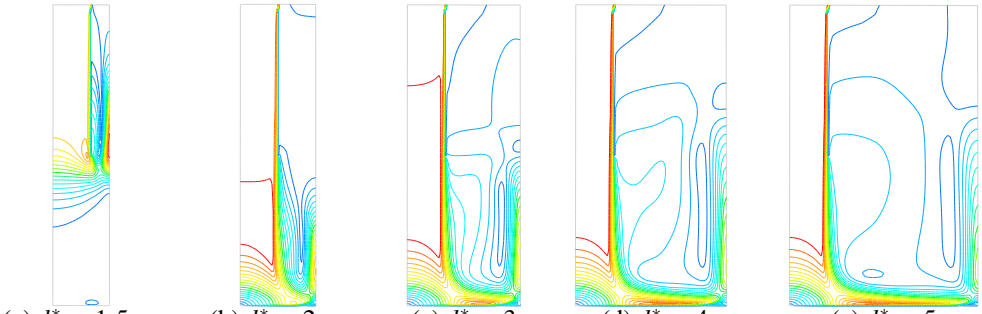

(a) $l^* = 1.5$ (b) $l^* = 2$ (c) $l^* = 3$ (d) $l^* = 4$ (e) $l^* = 5$

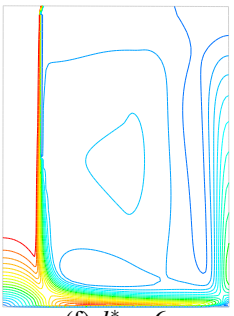

(f) $l^* = 6$

Figure 7.21: Velocity Contours, Square Array, z^* = 2, Re = 30,000

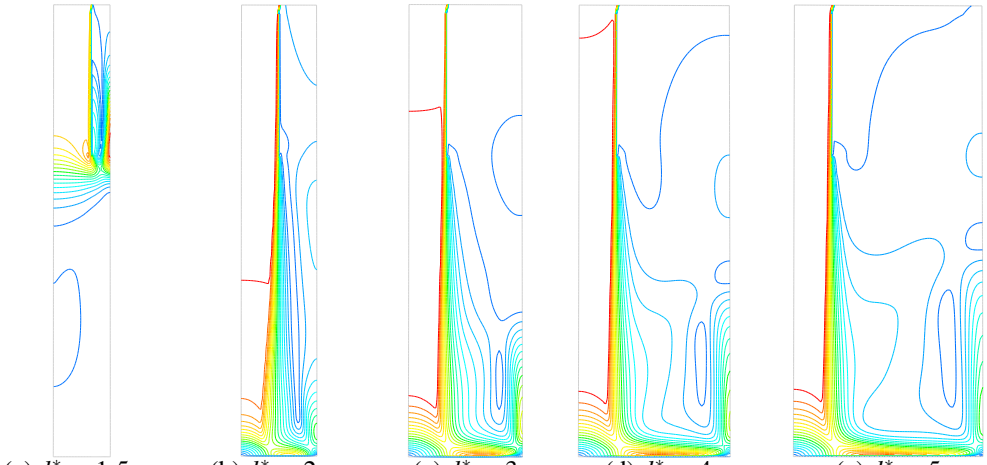

(a) $l^* = 1.5$ (b) $l^* = 2$ (c) $l^* = 3$ (d) $l^* = 4$ (e) $l^* = 5$

(f) $l^* = 6$

Figure 7.22: Velocity Contours, Square Array, z^* = 4, Re = 30,000

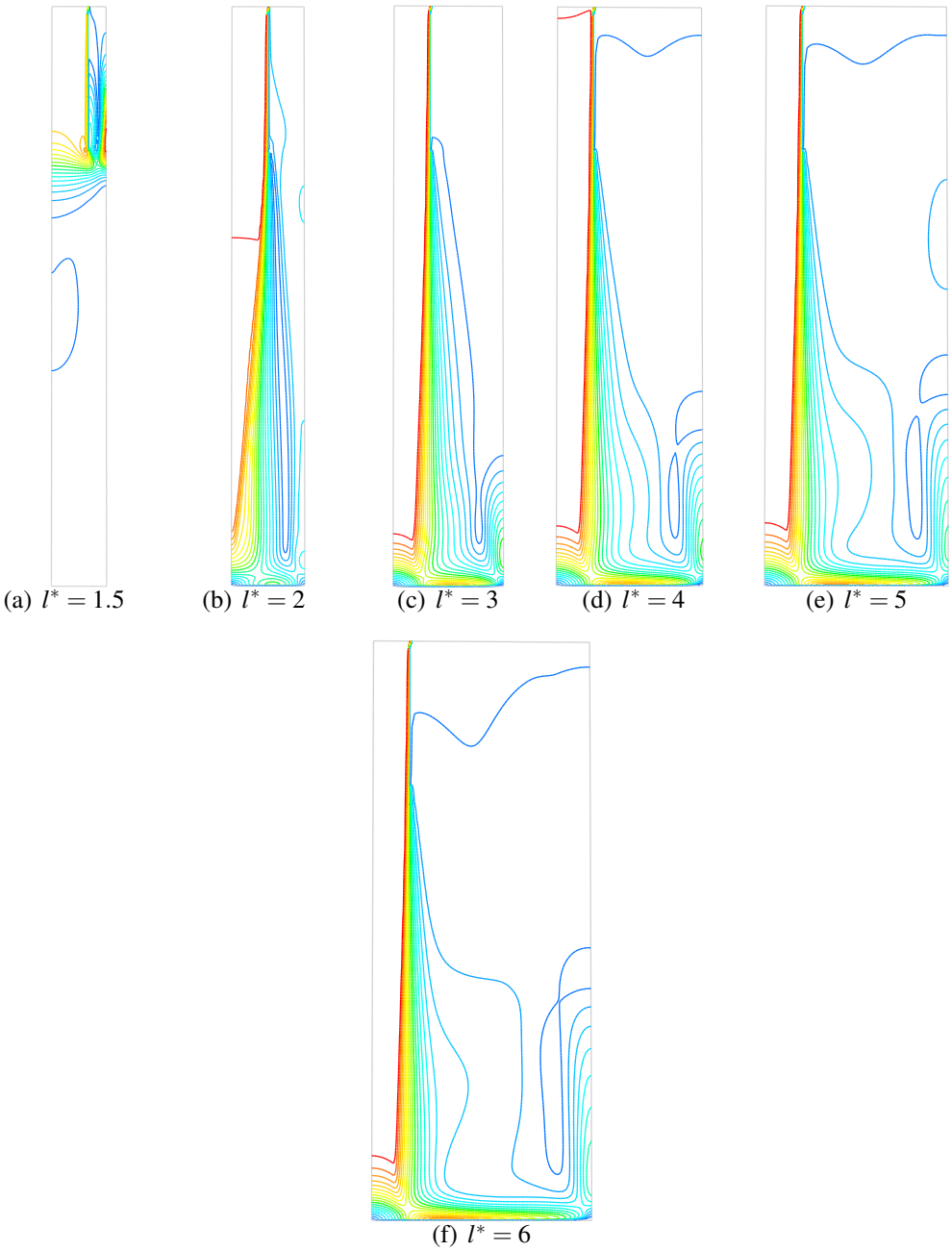

(a) $l^* = 1.5$ (b) $l^* = 2$ (c) $l^* = 3$ (d) $l^* = 4$ (e) $l^* = 5$

(f) $l^* = 6$

Figure 7.23: Velocity Contours, Square Array, z^* = 6, Re = 30,000

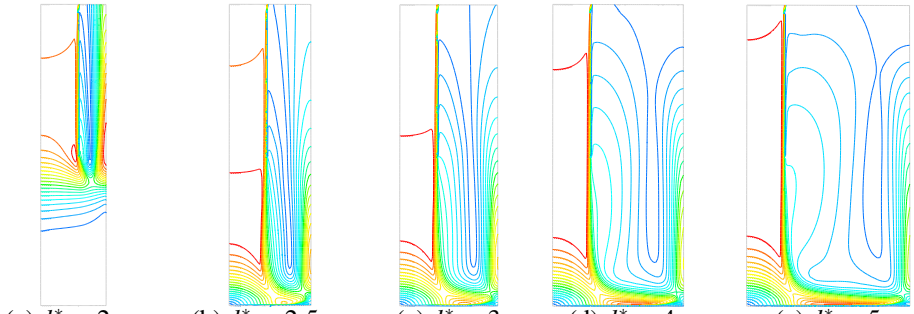

(a) $l^* = 2$ (b) $l^* = 2.5$ (c) $l^* = 3$ (d) $l^* = 4$ (e) $l^* = 5$

(f) $l^* = 6$

Figure 7.24: Velocity Contours, Hexagonal Array, z^* = 2, Re = 30,000

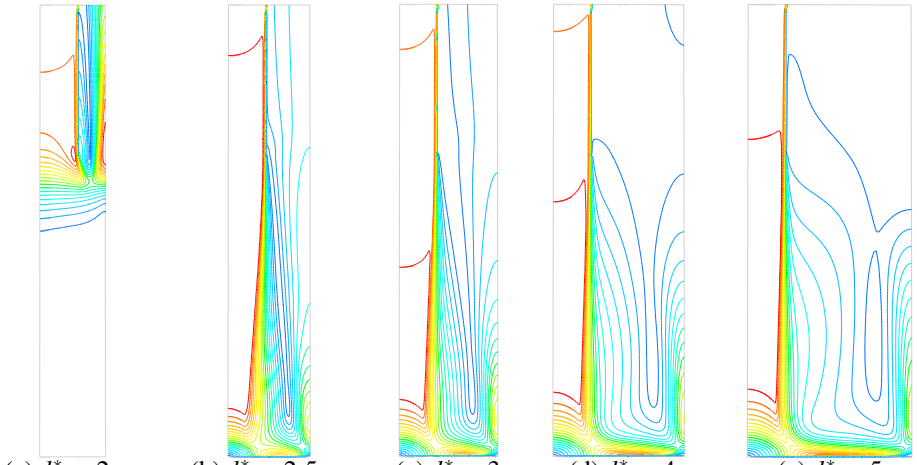

(a) $l^* = 2$ (b) $l^* = 2.5$ (c) $l^* = 3$ (d) $l^* = 4$ (e) $l^* = 5$

(f) $l^* = 6$

Figure 7.25: Velocity Contours, Hexagonal Array, z^* = 4, Re = 30,000

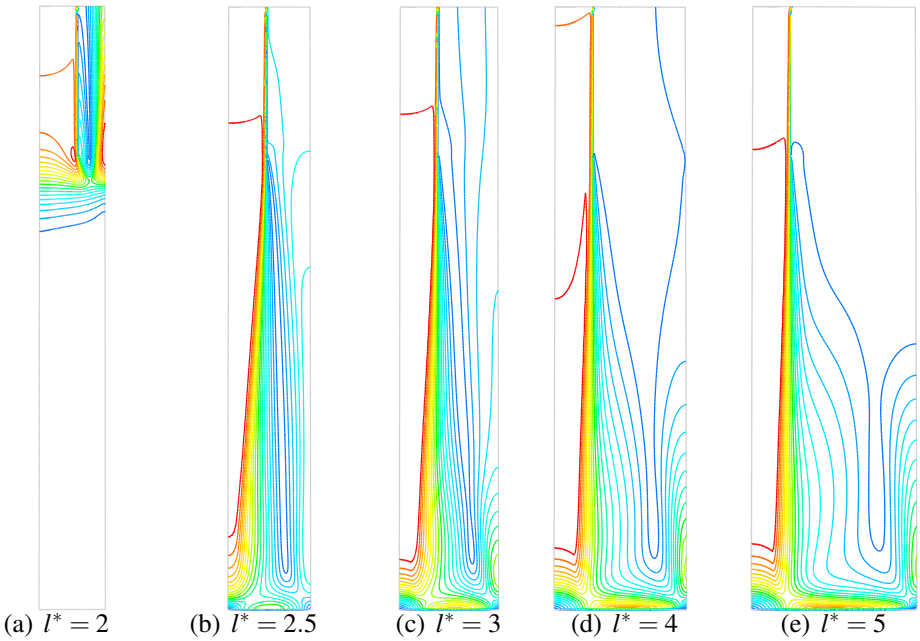

(a) $l^* = 2$ (b) $l^* = 2.5$ (c) $l^* = 3$ (d) $l^* = 4$ (e) $l^* = 5$

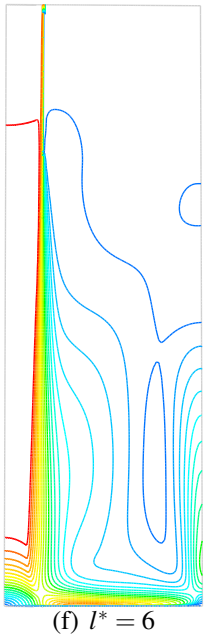

(f) $l^* = 6$

Figure 7.26: Velocity Contours, Hexagonal Array, z^* = 6, Re = 30,000

7.3.4 Jet-to-surface Distance

In most cases the jet-to-surface distance was observed to only maringally affect the average Nusselt number. However at the lowest jet-to-jet spacing above the critical value, the average Nusselt number was observed to increase significantly as the jet-to-surface distance was increased. This trend was observed for both the square and hexagonal array configurations where the jet-to-jet spacing was above the critical value and at all the Reynolds numbers investigated. The maximum heat transfer is observed at a jet-to-surface distance of 6. This value is consistent with existing work on the subject.

7.3.5 Nusselt Number Correlations

Correlations for the heat transfer, in terms of the average Nusselt number, were developed from the Nusselt number data presented in Section 7.3.1. The development of these correlations provides a number of benefits. Firstly, the correlations provide a quantitative measure of the influence of each of the correlated parameters on the heat transfer from the array. In addition the correlations provide a means to easily compare results obtained by other studies. Finally, these correlations serve as a useful design aid to predict the performance of systems that include a large array of impinging jets.

Existing Correlations

The most widely cited correlation for impinging jet heat transfer is that of Martin [2], which for an array of impinging jets is as follows

$$\frac{\overline{\mathrm{Nu}}}{\mathrm{Pr}^{0.42}} = K\left(A_r, \frac{H}{D}\right) G\left(A_r, \frac{H}{D}\right) F_2\left(\mathrm{Re}\right) \tag{7.3}$$

where

$$K = \left[1 + \left(\frac{H/D}{0.6/A_r^{1/2}}\right)^6\right]^{-0.05} \tag{7.4}$$

$$F_2 = 0.5\mathrm{Re}^{2/3} \tag{7.5}$$

and G is the heat transfer from a single round nozzle given by

$$G = 2A_r^{1/2}\frac{1-2.2A_r^{1/2}}{1+0.2(H/D-6)A_r^{1/2}} \tag{7.6}$$

The above correlation is valid for the following ranges of Reynolds number, H/D and A_r

$$\begin{bmatrix} 2000 \leq \mathrm{Re} \leq 100,000 \\ 2 \leq \frac{H}{D} \leq 12 \\ 0.004 \leq A_r \leq 0.04 \end{bmatrix}$$

Obot and Trabold [32] presented an alternative correlation to determine the average heat transfer from an array of impinging jets. The form of their correlation was

$$\overline{\mathrm{Nu}} = A_0\mathrm{Re}^m\overline{Z_n}^n A_f^x \tag{7.7}$$

where A_f is the open area fraction and A_0 a regression coefficient. The values for the correlation coefficient A_0 and the exponents m, n and x were determined for arrays where the spent fluid was ejected from the sides of the array only, and as such their results are not directly applicable for this work, though their correlation is used as the basis for the correlation presented in the next section.

Current Correlation

A correlation of the form of Equation 7.7 was initially chosen for the current work, and is presented again here, with the variables adapted to suit the current work.

$$\overline{\mathrm{Nu}} = C\mathrm{Re}^m z^{*n} l^{*p} \tag{7.8}$$

The heat transfer data for correlation was limited to jet arrays where the jet-to-jet spacing was above the critical value. This data was used to determine the values for

the coefficient C and the exponents m, n and p.

Prior to determining the coefficients for the complete correlation in Equation 7.8 separate correlations for each of the jet-to-surface distances studied were developed, of the form

$$\overline{\mathrm{Nu}} = C\mathrm{Re}^{m} l^{*p} \tag{7.9}$$

Least squares regression was used to determine the values for the exponents m and p subsequent to restricting the data set to arrays where the jet-to-jet spacing was above the critical value.

The resulting values for the parameters are shown in Table 7.2.

Configuration	z^*	C	m	p
Hexagonal	2	0.524	0.574	-0.415
Hexagonal	4	0.308	0.672	-0.654
Hexagonal	6	0.187	0.780	-0.942
Square	2	0.372	0.598	-0.428
Square	4	0.172	0.692	-0.464
Square	6	0.139	0.728	-0.472

Table 7.2: Correlation Parameters for Jet Arrays of varying jet-to-surface distance

The value for average surface Nusselt number obtained from the simulations are plotted against the value determined from the correlation in figures 7.27 to 7.32.

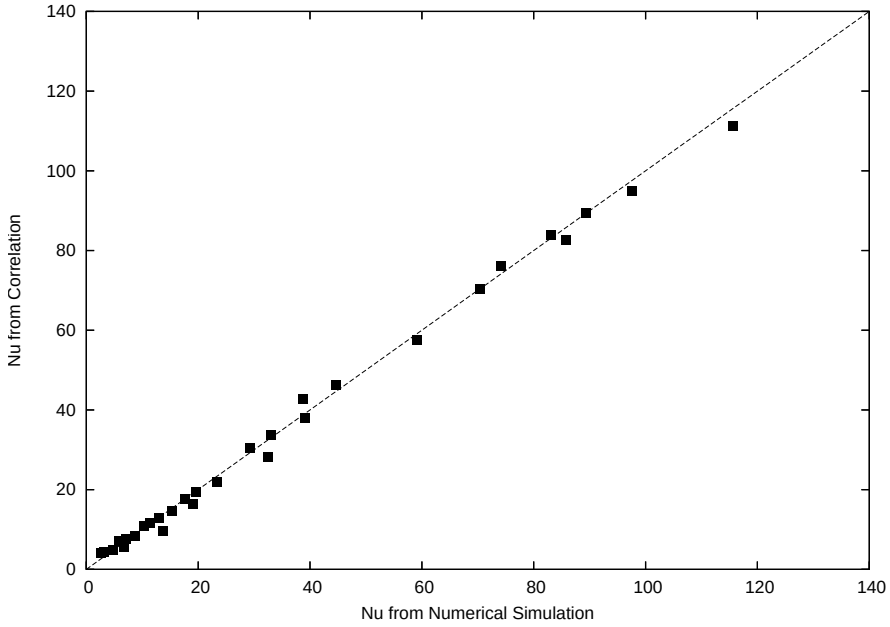

Figure 7.27: Correlated heat transfer, Square Array, z^*=2

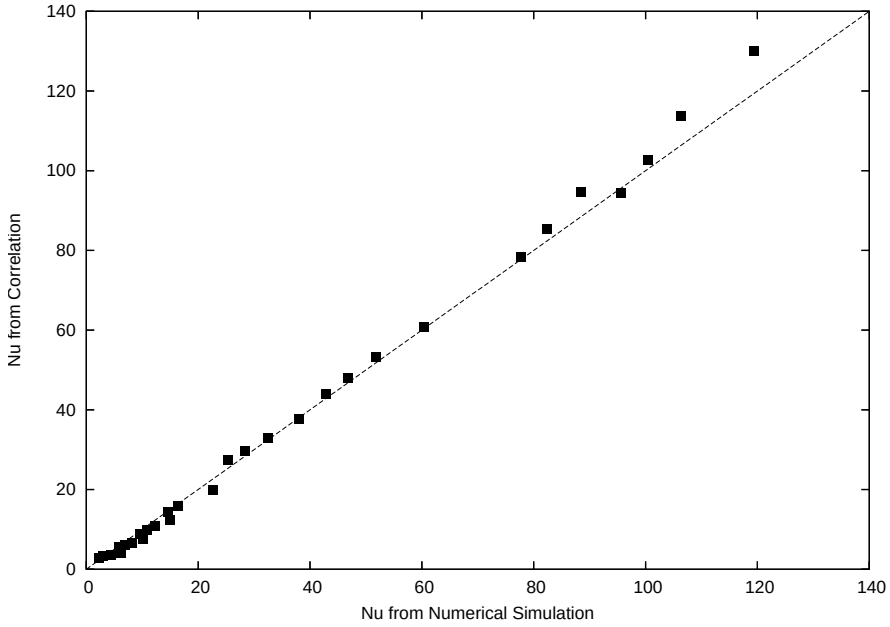

Figure 7.28: Correlated heat transfer, Square Array, z^*=4

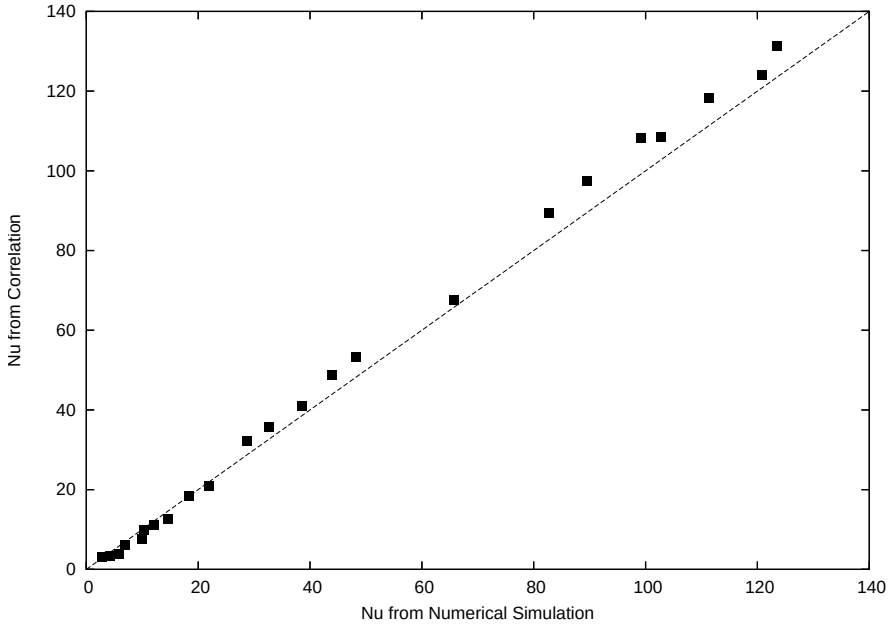

Figure 7.29: Correlated heat transfer, Square Array, z^*=6

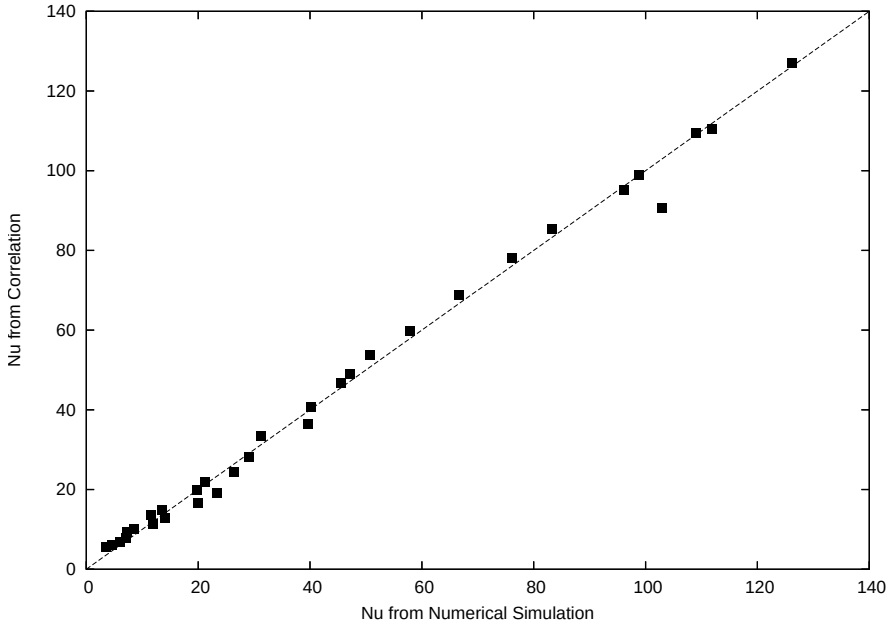

Figure 7.30: Correlated heat transfer, Hexagonal Array, z^*=2

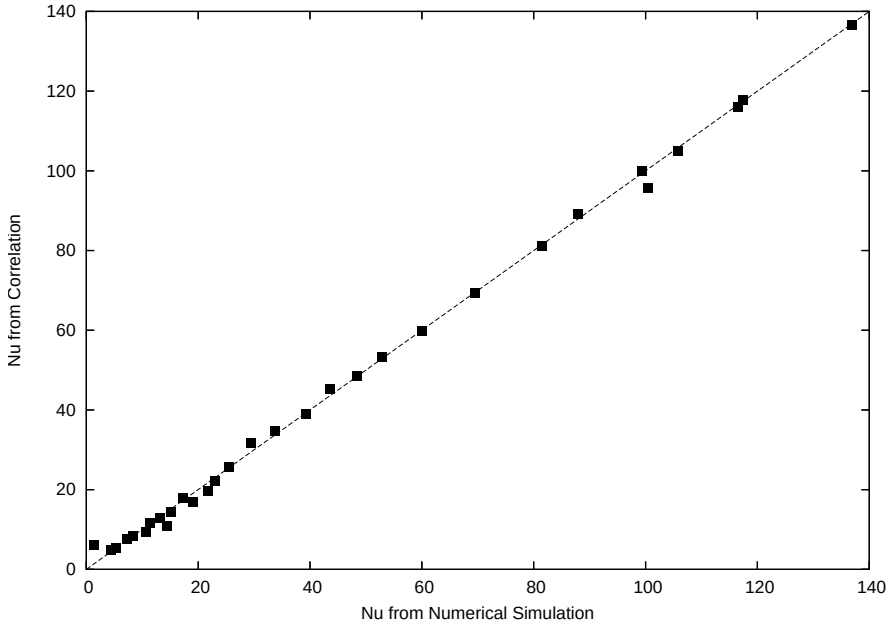

Figure 7.31: Correlated heat transfer, Hexagonal Array, z^*=4

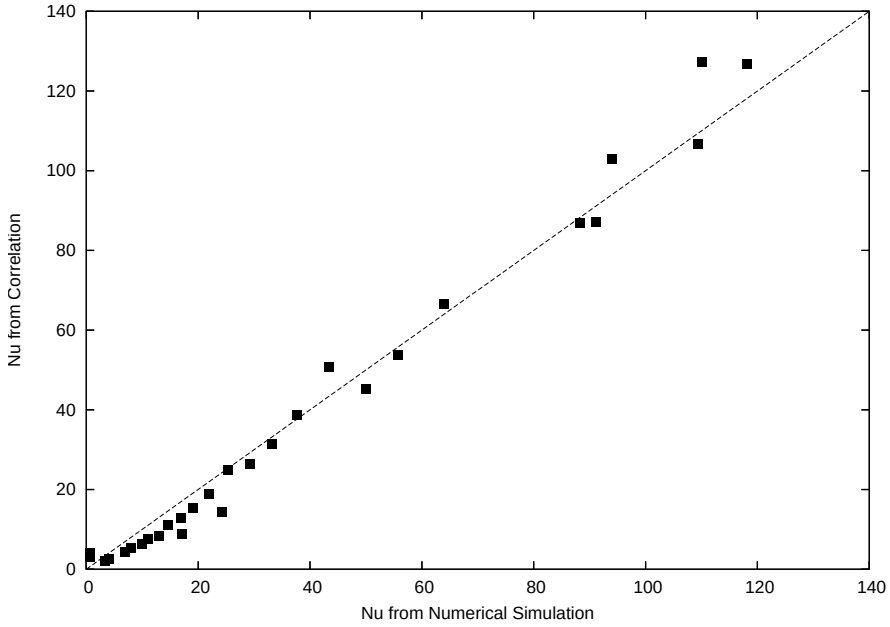

Figure 7.32: Correlated heat transfer, Hexagonal Array, z^*=6

The same procedure was followed to determine the exponents m, n, p and the constant C for the correlation in Equation 7.8. The values for these parameters are given in Table 7.3.

Configuration	C	m	n	p
Hexagonal	0.306	0.650	0.097	-0.590
Square	0.147	0.670	0.178	-0.374

Table 7.3: Correlation Parameters for Jet Arrays of varying jet-to-surface distance

Again the value for the average surface Nusselt number obtained from the simulations are plotted against the value predicted by the correlation, in figures 7.34 and 7.34.

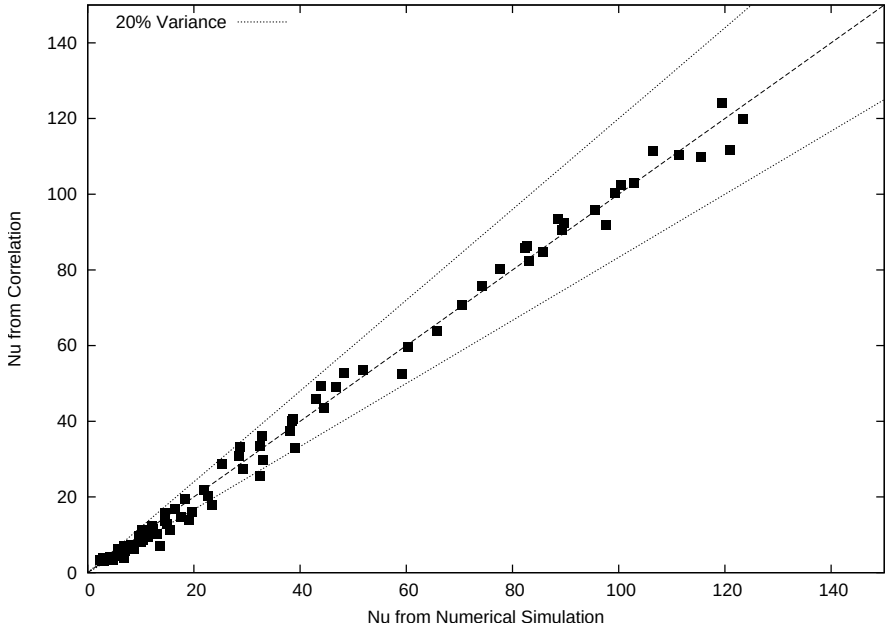

Figure 7.33: Correlated heat transfer, Square Array

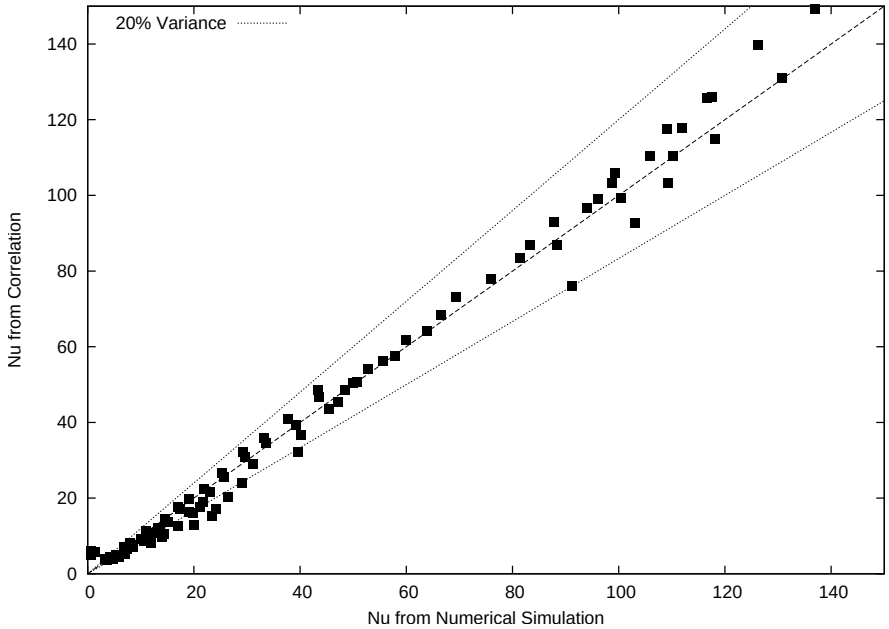

Figure 7.34: Correlated heat transfer, Hexagonal Array

As discussed in Section 7.3.2 the heat transfer from the jet array increased as the jet-to-jet spacing, l^*, decreased, so long as l^* remained above the well defined critical spacing. This observation is supported by the values of the related exponent p in Equation 7.8, which has the value -0.590 for a hexagonal array and the value -0.374 for a square array.

If the heat transfer is correlated to the area of the heat transfer surface instead of l^*, the exponents double since the area is proportional to l^{*2} as opposed to l^*. For a square array p becomes -0.748, while for a hexagonal array p becomes -1.180. This indicates that the heat transfer decreased at a faster rate than the heat transfer area increased. This further supports the conclusion that the optimum heat transfer would occur at the lowest jet-to-jet spacing, as was observed from this work.

Concentrating on the Reynolds number, the primary effect of increasing the Reynolds number of the jet was to increase the average heat transfer from the target surface. The value determined for the coefficient m in Equation 7.8 supports this observation, with the heat transfer increasing proportional to $\mathrm{Re}^{0.670}$ for a square array and to $\mathrm{Re}^{0.650}$ for a hexagonal array. These value are consistent with the results of Martin [2] in Equation 7.3 who found the heat transfer to increase proportionally to $\mathrm{Re}^{2/3}$.

The third major factor found to affect the heat transfer from an infinite array of impinging jets was the jet-to-surface distance, z^*. Increasing this distance increased the average Nusselt number in all of the cases investigated where the jet-to-jet spacing was above the critical value. The low positive value for the coefficient n in Equation 7.8 indicates that the influence was only minor over the range of values investigated, as indicated by values for n equal to 0.178 for a square array and 0.097 for a hexagonal array.

7.4 Conclusions

This chapter invetigated the heat transfer from ‘large’ arrays of impinging jets. While many similar investigations have been conducted, the study presented here examined

the heat transfer for a larger parameter space than is typically considered. In particular closely packed arrays were studied, with the result that a critical minimum spacing was identified, below which heat transfer was observed to significantly decrease. The maximum heat transfer occurred at the lowest jet-to-jet spacing that was above the critical value. This value was found to be independent of the Reynolds number, though the value did depend on the configuration of the array (square or hexagonal).

In addition to identifying the a critical spacing for these arrays, the heat transfer from each configuration was correlated against the Reynolds number, jet-to-surface height and the jet-spacing. The large parameter space of these correlations, and the identification of a critical jet-to-jet distance make an important contribution to the existing research on impinging jet arrays.

Chapter 8

Summary and Conclusions

This thesis presented investigations into three schemes for enhancing the heat transfer from impinging jet systems. Two schemes concentrated on single jet systems, and the final investigated arrays of impinging jets.

For the single jet systems the approaches focussed on modifying the flow in the stagnation region of an impinging jet. This region consists of nearly stagnant fluid and has the highest local heat transfer in an impinging jet system. The methods presented in chapters 5 and 6 resulted from considering each of these two points. In Chapter 5 it was proposed that the heat transfer could be improved by replacing the near stagnant fluid surrounding the impingement point with a solid of higher conductivity, while in Chapter 6 it was proposed that heat transfer could be enhanced by introducing an additional 'stagnation region'. This was achieved by forcing the jet to impinge into a cylindrical cavity directly beneath the nozzle.

For arrays of impinging jets much data exists already. The work presented in this thesis extends the already existing knowledge by detailed investigation of impinging jet arrays at low jet-to-jet spacings over a wide range of Reynolds numbers.

The following sections summarize in more detail the conclusions from each component of the work presented in this thesis.

8.1 Surface Protrusions

In Chapter 5 the potential for heat transfer enhancement by the addition of a protruding object beneath an impinging jet was investigated. Conical protrusions with high thermal conductivity were numerically simulated, where the cones were located on the target surface in-line with the jet axis. Heat transfer enhancement was observed for a number of cases, though in general large variations in the effects were evident from the

results. These effects ranged from a reduction in heat transfer, by up to 13%, in some cases, while for other cases, the heat transfer was significantly improved. The highest heat transfer improvement was in the order of an 80% increase compared with a flat plate. In addition to plain cones, cones with a fillet at the base were also investigated. At low Reynolds numbers the fillets aided heat transfer, while at high Reynolds numbers reductions in the heat transfer were observed, due to lower turbulence generation at the cone base. The extent of enhancement was found to be highly dependent on the geometry of the cone. This suggests that further enhancement could well be possible by fine-tuning the shape of the surface protrusion depending on the particular application. No previous work on surface protrusions of this type were found in the literature, and the results presented here contribute to the body of work on this subject.

8.2 Surface Cavities

In Chapter 6, the potential for heat transfer enhancement including a cylindrical cavity beneath the jet was investigated. Simple cylindrical cavities of varying depths and diameters, located directly beneath the jet were studied in order to gauge the effectiveness of the method. Results indicated that significant gains in heat transfer were possible, with the maximum observed gain showing a 45% increase in heat transfer compared with a flat surface. The key parameter affecting the heat transfer from the cavity was found to be the 'net cavity depth', which roughly corresponds to the distance between the exit of the jet nozzle and the base of the cavity. To allow a more transparent evaluation of the scheme, the presented results did not take into account heat transfer from the side-walls of the cavity. Allowing heat transfer from the sides of the cavity, in addition to the base would allow even better enhancement of heat transfer to be realised. As with the surface protrusion scheme, no previous work on surface cavities of this type could be found in the literature. As such the work presented in Chapter 6 makes a significant contribution to the field.

8.3 Impinging Jet Arrays

The work presented in Chapter 7 used a 'representative jet' analysis to determine the potential heat transfer from 'large' arrays of impinging jets. Two configurations of array were considered, either hexagonal or square, over a range of Reynolds numbers, and jet-to-surface heights. The range of jet-to-jet spacings investigated extended lower than the existing work on the subject. This allowed a critical jet-to-jet spacing to be identified, below which heat transfer was significantly reduced. In addition identifying this critical value, the heat transfer was correlated against the Reynolds number and jet-to-jet spacing for both configurations. These correlations allow the heat transfer to be determined for a large range of different impinging jet arrays and are an important addition to the existing work on impinging jet heat transfer.

8.4 Final comments

Impinging jets have been the subject of much investigation due to their high heat transfer rates. Even so, there is still potential for further enhancing the heat transfer characteristics of these systems. This thesis investigated a number of methods for improving the heat transfer characteristics of impinging jets. Chapters 5 and 6 concentrated on improving the absolute potential for heat transfer in a single impinging jet while Chapter 7 concentrated on arrays of jets, a well-known technique used to reduce the spatial variation of heat transfer from impinging jets.

The two local heat transfer enhancement schemes presented are novel techniques and hereto unreported. Both of these methods showed gains in heat transfer of up to 50% compared with standard impinging jets, and with further investigation no doubt additional gains could be realised. In particular, surface cavities could easily allow further increases in heat transfer to be obtained simply by allowing heat transfer from the cavity walls to occur.

Finally, any potential for improving the efficiency of devices or systems will result in real savings, in cost and energy. The work presented in this thesis will allow

some of these efficiencies to be realised and makes a valuable contribution to existing knowledge.

References

Every reasonable effort has been made to acknowledge the owners of copyright material. The author would be pleased to hear from any copyright owner who has been omitted or incorrectly acknowledged.

[1] K Jambunathan, E Lai, M A Moss, and B L Button. A review of heat transfer data for single circular jet impingement. *International Journal of Heat and Fluid Flow*, 13(2):106–115, 1992.

[2] H Martin. Heat and mass transfer between impinging gas jets and solid surfaces. In *Advances in heat transfer*, pages 1–60. Academic Press, 1977.

[3] J W B Baughn and S Shimizu. Heat transfer measurements from a surface with uniform heat flux and an impinging jet. *ASME Journal of Heat Transfer*, 111: 1096, 1989.

[4] James W Baughn, A E Hechanova, and Xiaojun Yan. An experimental study of entrainment effects on the heat transfer from a flat surface to a heated circular impinging jet. *Transactions of the ASME Journal of Heat Transfer*, 113:1023–1025, 1991.

[5] D Cooper, C Jackson, B E Launder, and G X Liao. Impinging jet studies for turbulence model assessment – I Flow-field experiments. *International Journal of Heat and Mass Transfer*, 36:2675 – 2684, 1993.

[6] T J Craft, L J W Graham, and B E Launder. Impinging jet studies for turbulence model assessment – II An examination of four turbulence models. *International Journal of Heat and Mass Transfer*, 36:2685 – 2697, 1993.

[7] D Lee, R Greif, S J Lee, and J H Lee. Heat transfer from a flat plate to a fully developed axisymmetric impinging jet. *Transactions of the ASME Journal of Heat Transfer*, 117:772–776, 1995.

[8] Koichi Nishino, Masanori Samada, Keiichi Kasuya, and Kahoru Torii. Turbulence statistics in the stagnation region of an axisymmetric impinging jet flow. *International Journal of Heat and Fluid Flow*, 17:193–201, 1996.

[9] S Ashforth-Frost, K Jambunathan, C F Whitney, and S J Ball. Heat transfer from a flat plate to a turbulent axisymmetric impinging jet. *Proceedings of the Institution of Mechanical Engineers*, 211:167–172, 1997.

[10] Jun Sakakibara, Koichi Hishida, and Masanobu Maeda. Vortex structure and heat transfer in the stagnation region of an impinging plane jet (simultaneous measurements of velocity and temperature fields by digital particle image velocimetry and laser-induced fluorescence). *International Journal of Heat and Mass Transfer*, 40:3163–3176, 1997.

[11] Chin-Yuan Li and Suresh V Garimella. Prandtl-number effects and generalized correlations for confined and submerged jet impingement. *International Journal of Heat and Mass Transfer*, 44:3471–3480, 2001.

[12] B E Launder and B I Sharma. Application of the energy-dissipation model of turbulence to the calculation of flow near a spinning disc. *Letters in Heat and Mass Transfer*, 1:131–137, 1974.

[13] P A Durbin. Separated flow computations with the k-ε-v^2 model. *AIAA Journal*, 33(4):659–664, 1995.

[14] P A Durbin. Near wall turbulence closure without damping functions. *Theoretical and Computational Fluid Dynamics*, 3:1–13, 1991.

[15] P A Durbin. On the k-ε stagnation point anomaly. *International Journal of Heat and Fluid Flow*, 17:89–90, 1996.

[16] M Dianat, M Fairweather, and W P Jones. Predictions of axisymmetric and two-dimensional impinging turbulent jets. *International Journal of Heat and Fluid Flow*, 17:530–538, 1996.

[17] M Behnia, S Parneix, and P A Durbin. Prediction of heat transfer in an axisymmetric turbulent jet impinging on a flat plate. *International Journal of Heat and Mass Transfer*, 41:1845–1855, 1998.

[18] Garron K Morris, Suresh V Garimella, and Janice A Fitzgerald. Improved predictions of the flow field in submerged and confined impinging jets using the reynolds stress model. In *1998 Intersociety Conference on Thermal Phenomena*, pages 362–370, 1998.

[19] M Behnia, S Parneix, Y Shabany, and P A Durbin. Numerical study of turbulent heat transfer in confined and unconfined impinging jets. *International Journal of Heat and Fluid Flow*, 20:1–9, 1999.

[20] Seon Tae Park and Hyung Jin Sung. Development of a near-wall turbulence model and application to jet impingement heat transfer. *International Journal of Heat and Fluid Flow*, 22:10–18, 2001.

[21] Bart Merci and Erik Dick. Heat transfer predictions with a cubic k–ε model for axisymmetric turbulent jets impinging onto a flat plate. *International Journal of Heat and Mass Transfer*, 46:469–480, 2003.

[22] Masood Mesbah, James W Baughn, and Christopher R Yap. The effect of curvature on the local heat transfer to an impinging jet on a hemispherically concave surface. In *The ninth international symposium on transport phenomena in thermal-fluids engineering*, pages 795–800, 1996.

[23] D H Lee, Y S Chung, and D S Kim. Turbulent flow and heat transfer measurements on a curved surface with a fully developed round impinging jet. *International Journal of Heat and Fluid Flow*, 18:160–169, 1997.

[24] Dae Hee Lee, Young Suk Chung, and Moo Geun Kim. Turbulent heat transfer from a convex hemispherical surface to a round impinging jet. *International Journal of Heat and Mass Transfer*, 42:1147–1156, 1999.

[25] Abdlmonem H Beitelmal, Michel A Saad, and Chandrakant D Patel. Effects of surface roughness on the average heat transfer of an impinging air jet. *International Communications in Heat and Mass Transfer*, 27:1–12, 2000.

[26] Srinath V Ekkad and David Kontrovitz. Jet impingement heat transfer on dimpled target surfaces. *International Journal of Heat and Fluid Flow*, 23:22–28, 2002.

[27] B S Yilbas, S Z Shuja, and M O Budair. Jet impingement onto a cavity. *International Journal of Numerical Methods for Heat and Fluid Flow*, 12(7):817–838, 2002.

[28] B S Yilbas, S Z Shuja, and M O Budair. Jet impingement onto a conical cavity with elevated wall temperature. *International Journal of Numerical Methods for Heat and Fluid Flow*, 14(8):1011–1028, 2004.

[29] R J Goldstein and J F Timmers. Visualization of heat transfer from arrays of impinging jets. *International Journal of Heat and Mass Transfer*, 25(12):1857–1868, 1982.

[30] L W Florschuetz, D E Metzger, and C C Su. Heat transfer characteristics for jet array impingement with initial crossflow. *Transactions of the ASME Journal of Heat Transfer*, 106:34–41, 1984.

[31] L W Florschuetz and C C Su. Effects of crossflow temperature on heat transfer within an array of impinging jets. *Transactions of the ASME Journal of Heat Transfer*, 109:74–82, 1987.

[32] N T Obot and T A Trabold. Impingement heat transfer within arrays of circular jets: Part 1 — Effects of minimum, intermediate, and complete crossflow for small and large spacings. *Transactions of the ASME Journal of Heat Transfer*, 109:872–879, 1987.

[33] Aaron M Huber and Raymond Viskanta. Effect of jet-jet spacing on convective

heat transfer to confined, impinging arrays of axisymmetric air jets. *International Journal of Heat and Mass Transfer*, 37(18):2859–2869, 1994.

[34] Jung-Yang San and Mao-De Lai. Optimum jet-to-jet spacing of heat transfer for staggered arrays of impinging air jets. *International Journal of Heat and Mass Transfer*, 44:3997–4007, 2001.

[35] P Brevet, C Dejeu, E Dorignac, M Jolly, and J J Vullierme. Heat transfer to a row of impinging jets in consideration of optimization. *International Journal of Heat and Mass Transfer*, 45:4191–4200, 2002.

[36] Dong-Ho Rhee, Pil-Hyun Yoon, and Hyung Hee Cho. Local heat/mass transfer and flow characteristics of array impinging jets with effusion holes ejecting spent air. *International Journal of Heat and Mass Transfer*, 46:1049–1061, 2003.

[37] L B Y Aldabbagh and I Sezai. Three-dimensional numerical simulation of an array of impinging laminar square jets with spent fluid removal. *International Journal of Thermal Sciences*, 43:241–247, 2004.

[38] W M Yan, S C Mei, H C Liu, C Y Soong, and W-J Yang. Measurement of detailed heat transfer on a surface under arrays of impinging elliptic jets by a transient liquid crystal technique. *International Journal of Heat and Mass Transfer*, 47: 5235–5245, 2004.

[39] L Thielen, H J J Jonker, and K Hanjalić. Symmetry breaking of flow and heat transfer in multiple impinging jets. *International Journal of Heat and Fluid Flow*, 24:444–453, 2003.

[40] Fluent Inc. *Fluent 6.1 User's Guide*, 2003.

[41] H K Versteeg and W Malalasekera. *An introduction to computational fluid dynamics: The finite volume method*. Longman Scientific and Technical, 1995.

[42] Hermann Schlichting. *Boundary Layer Theory*. McGraw-Hill, 1979.

[43] S V Patankar. *Numerical Heat Transfer and Fluid Flow*. McGraw-Hill, 1980.

[44] R I Issa. Solution of implicitly discretized fluid flow equations by operator splitting. *Journal of Computational Physics*, 62:40 – 65, 1986.

[45] Z Yang and Tsan-Hsing Shih. A k-ε model for turbulent and transitional boundary layers. In *Near Wall Turbulent Flows*, pages 165–176. Elsevier, 1993.

[46] M Behnia, S Parneix, and P A Durbin. Accurate modeling of impinging jet heat transfer. *Annual Research Briefs*, pages 149–164, 1997.

[47] David C Wilcox. *Turbulence Modelling for CFD*. DCW Industries Inc., 1998.

[48] M M Gibson and B E Launder. Ground effects on pressure fluctuations in the atmospheric boundary layer. *Journal of Fluid Mechanics*, 86:491–511, 1978.

[49] B E Launder. Second-moment closure: Present... and future? *International Journal of Heat and Fluid Flow*, 10(4):282–300, 1989.

[50] B E Launder, G J Reece, and W Rodi. Progress in the development of a reynolds-stress turbulence closure. *Journal of Fluid Mechanics*, 68(3):537–566, 1975.

Appendix A

List of Supporting Papers

A J C King and T T Chandratilleke, Heat transfer characteristics in impinging jet arrays,*Australian Journal of Mechanical Engineering*, 4(1):59-64, 2007

A J C King and T T Chandratilleke, Heat transfer enhancement in single impinging jets due to surface cavities, *5th International Conference on Heat Transfer, Fluid Mechanics and Thermodynamics*, 1-4 July, 2007, Sun City, South Africa

T T Chandratilleke, **A J C King** and R Narayanaswamy, Thermal performance and optimisation of an impinging fluid jet array at a heated surface, *13th International Heat Transfer Conference*, July, 2006, Sydney.

A J C King and T T Chandratilleke, Effects of surface modification on heat and fluid flow characteristics in fluid jets impinging on a heated surface, *8th Australasian Heat and Mass Transfer Conference*, July, 2005, Perth

A J C King, T T Chandratilleke, Heat transfer characteristics in impinging jet arrays, *8th Australasian Heat and Mass Transfer Conference*, July, 2005, Perth

A J C King, T T Chandratilleke, Heat transfer enhancement in impinging jets by surface modification, *6th Electronics Packaging Technology Conference*, pp. 270–273, December, 2004, Singapore

A J C King, T T Chandratilleke, Turbulence modelling of impinging jets for high heat flux cooling applications, *International Conference on Computational Methods*, pp. 177–182, December, 2004, Singapore.

Appendix B

Turbulence Model Transport Equations

B.1 k-ε model

The transport equation in the k-ε model for the turbulent kinetic energy is

$$\frac{\partial}{\partial t}(\rho k)+\frac{\partial}{\partial x_i}(\rho k u_i)=\frac{\partial}{\partial x_j}\left[\left(\mu+\frac{\mu_t}{\sigma_k}\right)\frac{\partial k}{\partial x_j}\right]+G_k-\rho\varepsilon \tag{B.1}$$

where G_k is the generation of TKE, and is given by

$$G_k=\mu_t S^2 \tag{B.2}$$

where S is the modulus of the mean strain rate tensor, defined as

$$S\equiv\sqrt{2S_{ij}S_{ij}} \tag{B.3}$$

The transport equation for the dissipation rate is

$$\frac{\partial}{\partial t}(\rho\varepsilon)+\frac{\partial}{\partial x_i}(\rho\varepsilon u_i)=\frac{\partial}{\partial x_j}\left[\left(\mu+\frac{\mu_t}{\sigma_k}\right)\frac{\partial\varepsilon}{\partial x_j}\right]+C_{1\varepsilon}G_k-C_{2\varepsilon}\rho\frac{\varepsilon^2}{k} \tag{B.4}$$

where $C_{1\varepsilon}$ and $C_{2\varepsilon}$ are constants.

The energy transport equation is

$$\frac{\partial}{\partial t}(\rho E)+\frac{\partial}{\partial x_i}[u_i(\rho E+p)]=\frac{\partial}{\partial x_j}\left(k_{\mathrm{T,eff}}\frac{\partial T}{\partial x_j}+u_i(\tau_{ij})_{\mathrm{eff}}\right) \tag{B.5}$$

where

$$(\tau_{ij})_{\mathrm{eff}}=\mu_{\mathrm{eff}}\left(\frac{\partial u_j}{\partial x_i}\frac{\partial u_i}{\partial x_j}\right)-\frac{2}{3}\mu_{\mathrm{eff}}\frac{\partial u_i}{\partial x_i}\delta_{ij} \tag{B.6}$$

and

$$k_{\mathrm{T,eff}} = k_{\mathrm{T}} + \frac{c_p \mu_t}{\mathrm{Pr}_t} \tag{B.7}$$

The turbulent viscosity, μ_t is given by

$$\mu_t = \rho C_\mu \frac{k^2}{\varepsilon} \tag{B.8}$$

where C_μ is a constant. σ_k, σ_ω are the turbulent Prandtl numbers for k and ε.

The model constants (derived empirically) are

$$C_{1\varepsilon} = 1.44, C_{2\varepsilon} = 1.92, C_\mu = 0.09, \sigma_k = 1.0, \sigma_\varepsilon = 1.3$$

B.2 k-ω model

The transport equations for the k-ω model are

$$\frac{\partial}{\partial t}(\rho k) + \frac{\partial}{\partial x_i}(\rho k u_i) = \frac{\partial}{\partial x_j}\left[\left(\mu + \frac{\mu_t}{\sigma_k}\right)\frac{\partial k}{\partial x_j}\right] + G_k - Y_k \tag{B.9}$$

turbulent kinetic energy and

$$\frac{\partial}{\partial t}(\rho \omega) + \frac{\partial}{\partial x_i}(\rho \omega u_i) = \frac{\partial}{\partial x_j}\left[\left(\mu + \frac{\mu_t}{\sigma_\omega}\right)\frac{\partial \omega}{\partial x_j}\right] + G_\omega - Y_\omega \tag{B.10}$$

for the specific dissipation rate. G_k and G_ω account for the production of k and ω, respectively while Y_k and Y_ω account for their dissipation

The turbulent viscosity is given by

$$\mu_t = \alpha^* \frac{\rho k}{\omega} \tag{B.11}$$

where

$$\alpha^* = \left(\frac{\alpha_0^* + \mathrm{Re}_t/R_k}{1 + \mathrm{Re}_t/R_k}\right) \tag{B.12}$$

and accounts for damping of the turbulent viscosity at low Reynolds numbers. The

constants in the above equation are

$$\mathrm{Re}_t = \frac{\rho k}{\mu \omega}, R_k = 6, \alpha_0^* = \frac{\beta_i}{3}, \beta_i = 0.072$$

The rate of production of turbulent kinetic energy is given by

$$G_k = \mu_t S^2 \tag{B.13}$$

where S is the mean strain rate tensor as before.

The rate of production of ω is given by

$$G_\omega = \alpha \frac{w}{k} G_k \tag{B.14}$$

where

$$\alpha = \frac{0.52}{\alpha^*} \left(\frac{\alpha_0 + \mathrm{Re}_t / R_\omega}{1 + \mathrm{Re}_t / R_\omega} \right) \tag{B.15}$$

and $R_\omega = 2.95$.

B.3 $\overline{v}^2$-f model

The transport equation for the turbulent kinetic energy in the $\overline{v}^2$-f model is given by

$$\frac{\partial}{\partial t}(\rho k) + \frac{\partial}{\partial x_i}(\rho k u_i) = \frac{\partial}{\partial x_j}\left[\left(\mu + \frac{\mu_t}{\sigma_k} \right) \frac{\partial k}{\partial x_j} \right] + G_k - \rho \varepsilon \tag{B.16}$$

The transport equation for the dissipation rate is

$$\frac{\partial}{\partial t}(\rho \varepsilon) + \frac{\partial}{\partial x_i}(\rho \varepsilon u_i) = \frac{\partial}{\partial x_j}\left[\left(\mu + \frac{\mu_t}{\sigma_k} \right) \frac{\partial \varepsilon}{\partial x_j} \right] + C_{1\varepsilon} G_k - C_{2\varepsilon} \rho \frac{\varepsilon^2}{k} \tag{B.17}$$

The $\overline{v}^2$-f model uses $\overline{v}^2$, as the turbulent length scale to determine the turbulent

viscosity. $\bar{v}^2$ needs an additional transport equation, given as

$$\frac{\partial}{\partial t}(\rho\bar{v}^2)+\frac{\partial}{\partial x_i}(\rho\bar{v}^2u_i)=\frac{\partial}{\partial x_j}\left[\left(\mu+\frac{\mu_t}{\sigma_k}\right)\frac{\partial\bar{v}^2}{\partial x_j}\right]+\rho k f_{22}-\rho\bar{v}^2\frac{\varepsilon}{k} \tag{B.18}$$

An elliptic relaxation function is used to determine the source of $\bar{v}^2$, $\rho k f_{22}$ and is given as

$$\frac{\partial}{\partial x_j}\left(\frac{\partial f_{22}}{\partial x_j}\right)-f_{22}=(1-C_1)\frac{2/3-\bar{v}^2/k}{T}-C_2\frac{\mu_t S^2}{k} \tag{B.19}$$

The required length and time scales are

$$l^2=\max\left[\frac{k^3}{\varepsilon^2},C_\eta^2\left(\frac{\nu^3}{\varepsilon}\right)^{\frac{1}{2}}\right] \tag{B.20}$$

$$L=C_L l \tag{B.21}$$

$$T=\max\left[\frac{k}{\varepsilon},6\left(\frac{\nu}{\varepsilon}\right)^{\frac{1}{2}}\right] \tag{B.22}$$

Finally the turbulent viscosity is given by

$$\mu_t=\rho C_\mu\bar{v}^2T \tag{B.23}$$

The model constants are as follows

$$C_{\varepsilon 1}=1.3+\frac{0.25}{1+(d/l)^8}$$

$$C_\mu=0.19, C_{\varepsilon 2}=1.9, C_1=1.4, C_2=0.3$$

$$C_L=0.3, C_\eta=70.0, \sigma_k=1.0, \sigma_\varepsilon=1.3$$

B.4 RSM model

The Reynolds Stress turbulence model solves transport equations for each of the Reynolds stresses, $\rho\overline{u_i'u_j'}$ The Reynolds stress transport equations may be written as follows

$$\frac{\partial}{\partial t}(\rho\overline{u_i'u_j'}) + \frac{\partial}{\partial x_k}(\rho u_k\overline{u_i'u_j'}) =$$

$$-\frac{\partial}{\partial x_k}\left[\rho\overline{u_i'u_j'u_k'} + \overline{p\left(\delta_{kj}u_i' + \delta_{ik}u_j'\right)}\right] + \frac{\partial}{\partial x_k}\left[\mu\frac{\partial}{\partial x_k}\overline{u_i'u_j'}\right]$$

$$-\rho\left(\overline{u_i'u_k'}\frac{\partial u_j}{\partial x_k} + \overline{u_j'u_k'}\frac{\partial u_i}{\partial x_k}\right)$$

$$+\overline{p\left(\frac{\partial u_i'}{\partial x_j} + \frac{\partial u_j'}{\partial x_i}\right)} - 2\mu\overline{\left(\frac{\partial u_i'}{\partial x_k} + \frac{\partial u_j'}{\partial x_k}\right)} \tag{B.24}$$

The turbulent kinetic energy is calculated from the Reynolds stresses from

$$k = \frac{1}{2}\overline{u_i'u_i'} \tag{B.25}$$

Additionally a transport equation for the dissipation rate must also be solved, this is the same as for the k-ε model and is written as

$$\frac{\partial}{\partial t}(\rho\varepsilon) + \frac{\partial}{\partial x_i}(\rho\varepsilon u_i) = \frac{\partial}{\partial x_j}\left[\left(\mu + \frac{\mu_t}{\sigma_k}\right)\frac{\partial\varepsilon}{\partial x_j}\right] + C_{1\varepsilon}G_k - C_{2\varepsilon}\rho\frac{\varepsilon^2}{k} \tag{B.26}$$

finally, the turbulent viscosity is calculated from

$$\mu_t = \rho C_\mu\frac{k^2}{\mu} \tag{B.27}$$